Silicon-based components: 2D photonic crystal components and semiconductor nanocrystals

AMÉLIE TÊTU

Interdisciplinary Nanoscience Center (iNANO) and
Department of Physics and Astronomy
University of Aarhus, Denmark

PhD thesis
November 2007

A mes parents...

This thesis has been submitted to the Faculty of Science at the University of Aarhus in order to fulfill the requirements for obtaining a PhD degree in physics. The work has been carried out under the supervision of Professor Brian Bech Nielsen and Professor Martin Kristensen at the Interdisciplinary Nanoscience Center (iNANO) and the Department of Physics and Astronomy.

List of Publications

Peer reviewed international scientific journal publications:

[1] *Broadband topology-optimized photonic crystal components for both TE and TM polarizations*
A. Têtu, M. Kristensen, L. H. Frandsen, A. Harpøth, P. I. Borel, J. S. Jensen, and O. Sigmund, Opt. Express, **13**, 8606-8611 (2005).

[2] *Photonic-crystal waveguide biosensor*,
N. Skivesen, **A. Têtu**, M. Kristensen, J. Kjems, L. H. Frandsen, and P. I. Borel
Opt. Express, **15**, 3169-3176 (2007).

[3] *Optimization of Photonic Crystal 60° Waveguide Bends for Broadband and Slow-Light Transmission*,
A.V. Lavrinenko, **A. Têtu**, L. H. Frandsen, J. Fage-Pedersen, and P. I. Borel,
Appl. Phys. B, **87**, 52-56 (2007).

[4] *Topology optimisation of slow light coupling to photonic crystal waveguides*,
L. Yang, A.V. Lavrinenko, L. H. Frandsen, P. I. Borel, **A. Têtu**, and J. Fage-Pedersen,
Electron. Lett., **43**, 923-924 (2007).

[5] *InSb nanocrystals embedded in SiO_2: Strain and melting-point hysteresis*,
A. Têtu, J. Chevallier, and B. B. Nielsen,
Mater. Sci. Eng., B, *In press*.

Peer reviewed international scientific conference publications:

[1] *Low-Loss Photonic Crystal Y-Splitter for TM Polarization*,
A. Têtu, M. Kristensen, L. H. Frandsen, A. Harpøth, P. I. Borel, J. S. Jensen, and O. Sigmund,
Poster presentation, BGPP'05, Sydney, Australia (2005).

[2] *Enhancement of coupling to the slow light regime in photonic crystal waveguides using topology optimization*,
A. Têtu, L. Yang, A.V. Lavrinenko, L. H. Frandsen, and P. I. Borel,
Proceedings of CLEO USA 2006.

[3] *Optimization of photonic crystal 60° waveguide bends in the slow light regime for broadband transmission*,
A.V. Lavrinenko, **A. Têtu**, L. H. Frandsen, and P. I. Borel,
Proceedings of CLEO USA 2006.

[4] *Planar photonic crystal waveguide biosensor*,
N. Skivesen, **A. Têtu**, M. Kristensen, J. Kjems, L. H. Frandsen, and P. I. Borel,
European Conference on Integrated Optics (ECIO), Copenhagen, (2007).

[5] *Protein detection with a planar photonic-crystal sensor*,
N. Skivesen, **A. Têtu**, M. Kristensen, J. Kjems, L. H. Frandsen, and P. I. Borel,
CLEO-EU, München, (2007).

[6] *InSb nanocrystals embedded in SiO_2: Strain and melting-point hysteresis*,
A. Têtu, J. Chevallier, and B. B. Nielsen,
E-MRS, Strasbourg, (2007).

Non-reviewed scientific conference publications:

[1] *Broadband planar PBG components*,
M. Kristensen, and **A. Têtu**,
The annual meeting of the Danish Optical Society (DOPS), Risø (2005).

[2] *Silicon photonics: Electro-optic property and use of slow light*,
J. Fage-Pedersen, L. H. Frandsen, A.V. Lavrinenko, P. I. Borel, L. Yang, **A. Têtu**, and M. Kristensen,
DOPS-NYT, Nr.2, 2007, 22. årgang.

In preparation:

[1] *Experimental and theoretical study of the superheating and undercooling of InSb nanocrystals embedded in SiO_2,*
A. Têtu, J. Chevallier, and B. B. Nielsen.

List of Abbreviations

ASE Advanced silicon etch

BF Bright field

BBXRD Bragg-Brentano X-ray diffraction

BSE Back scattering electrons

EBL Electron beam lithography

EMA Effective mass approximation

DC Direct current

DUT Device under test

FDTD Finite-difference time-domain

HRTEM High resolution transmission electron microscopy

ICP Inductively coupled plasma etching

RF Radio frequency

LED Light emitting diode

MBG MIT Photonic Bands

OSA Optical spectrum analyser

PIXE Proton induced X-ray emission

PML Perfectly matched layer

PBG Photonic band gap

PhC Photonic crystal

PWE Plane-wave expansion

PVD Physical vapor deposition

RBS Rutherford back-scattering spectrometry

RIE Reactive ion etching

RF Radio frequency

RTA Rapid thermal annealing

SE Secondary electrons

SEM Scanning electron microscopy

SOI Silicon-on-insulator

TBM Tight binding method

TE Transverse electric

TEM Transmission electron microscopy

TM Transverse magnetic

TL Tunable laser

List of Figures

Acknowledgments

This thesis summarises the work I have been doing for the last three years. I would like to take the time to thank the people who helped and supported me during this process.

First of all I would like to thank my supervisors Brian Bech Nielsen and Martin Kristensen for their guidance during this project. Martin Kristensen helped me start this project and Brian Bech Nielsen shared his passion for and extensive knowledge of physics. I appreciated our many fruitful discussions[1]. Jacques Chevallier shared his expertise on electron microscopy and magnetron sputtering and also prepared most of the samples presented in this thesis. Pia Bomholt prepared a countless number of TEM samples, and John L. Hansen helped me with RBS.

Part of the work presented in this thesis was carried out at the Technical University of Denmark at the COM•DTU department, and I am most grateful for the hospitality I received. I would like to thank especially Lars H. Frandsen for having been a "master smurf" in the cleanroom and showing me everything he knew. I appreciated the discussions around a big cup of tea with Andrei V. Lavrinenko, who started the optimisation and simulation of the 60° bends for the slow light regime. Lirong Yang worked on the optimisation of the in-coupling for the slow light regime. Ole Sigmund and Jakob S. Jensen from MEK•DTU gave me the possibility of using their software package and helped using it. A special thank you goes to Peter I. Borel for his friendship, support, and advises.

Finally, I would like to thank Nykola Jones, Christian Uhrenfeldt, Jacques Chevallier, and Merete Raarup for proof reading completely or partially this thesis, and my family, friends, and chéri, for their support during the last three years.

[1] Until the very end!

Contents

CHAPTER 1

General introduction

Silicon is indubitably the most important material in the microelectronics industry. Its excellent electronic properties, studied for more than half a century, the abundance on earth, low cost, and its stable oxide, make it a natural choice for realising integrated electronic circuits. The performance of electronic devices and their cost have been greatly improved by downscaling the component on a chip to a minimum feature size, making it possible to have more than 10^8 transistors on a single chip. However, the scaling down of features introduces signal propagation delay between the different parts of a chip due to the tighter packing of the interconnections. It is believed that the propagation time delay will reach the actual computation delay, making it the limiting factor of the performance of a chip. This problem is commonly referred to as the *interconnect bottleneck*, and using photons instead of electrons for the communication on a chip could be a solution. For this reason, a lot of effort has been made in the field of silicon photonics to achieve the monolithic integration of optical components on CMOS-compatible silicon chips. This brings great challenges to overcome, since silicon is a poor optically active material due to its indirect band gap.

Recent breakthroughs in the study of the optical properties of silicon have paved the way for the production of fully compatible silicon devices. One of the most significant advances was the observation of

light emission from porous silicon [1] and silicon nanocrystals [2], which boosted the field of silicon photonics, as previously light emission was generally restricted to III-V-based compounds, which are expensive and often incompatible with silicon. More recently, the Raman effect was exploited to achieve lasing in silicon [3], and modulation of light in silicon [4] and low loss silicon passive components [5] have been demonstrated. All these interesting results show silicon from another perspective and make it a very attractive material for electro-optic integrated circuits.

One area of silicon photonics that has attracted attention lately is that of photonic crystal components. Negative refraction as well as slow group velocity have been demonstrated with 2D photonic crystals components. These components have already been realized on a silicon-on-insulator platform using CMOS-processing techniques based on deep ultraviolet lithography [6]. Passive components based on 2D photonic crystals have experienced major developments in the last few years. The interest has been focused on specific characteristics such as their high dispersion properties and the confinement of light in small volume high quality factor cavities, which could lead to active components [7,8].

Another rapidly growing field is that of light emitting nanocrystals. By scaling down a semiconductor crystal to a few nanometers, one can change the electronic properties of the semiconductors. The engineering of the bandgap can transform indirect bandgap material into potential light-emitters [2]. It has also been shown that silicon nanocrystals can be obtained in a SiO_2 matrix, which is fully compatible with silicon-based platforms [9].

The results presented in this thesis are related to the two subjects discussed above. The first part deals with 2D photonic crystal components. The fundamental science relating to this subject will be outlined, and details of the fabrication and characterisation techniques for these components will be introduced. The unique dispersion properties of 2D photonic crystals will be discussed. An optimisation method, which is called topology optimisation, used to maximize the performance of 2D photonic crystal components, for a given polarisation of light and a given range of wavelengths, will also be presented. This method has been applied to optimise the optical transmission properties of several structures for transverse electric polarised light. The propagation of transverse magnetic polarised light through those structures has also been investigated experimentally and theoretically, and will be presented. Topology opti-

misation was also used to optimise structures for the slow light regime, such as in-coupling structures and 60° bends.

InSb semiconductor nanocrystals is the focus of the second part of this thesis. In this part, the basic theory of the quantum confinement effect is described in order to understand the interesting features of nanocrystals, and also the potential applications of InSb nanocrystals. This will be followed by details of the fabrication and characterization of these structures. The results for the formation of InSb nanocrystals embedded in a SiO_2 matrix will be presented. This includes a study of their optical properties and their melting and solidification behaviour.

The final ambition of this project was to bring both subjects together to enhance the photoluminescence of a silicon-based light emitting device. The possibility of prohibiting light propagation for certain directions with a photonic crystal can help in reaching this goal [10]. By careful engineering of photonic band gap components to the resonance wavelength of the nanocrystals, the performance of these structures should be increased significantly. Unfortunately, the end of this project came before the merging of these two fields. It is hoped that the work presented in this thesis will motivate further research in this direction.

PART I

2D photonic crystal components

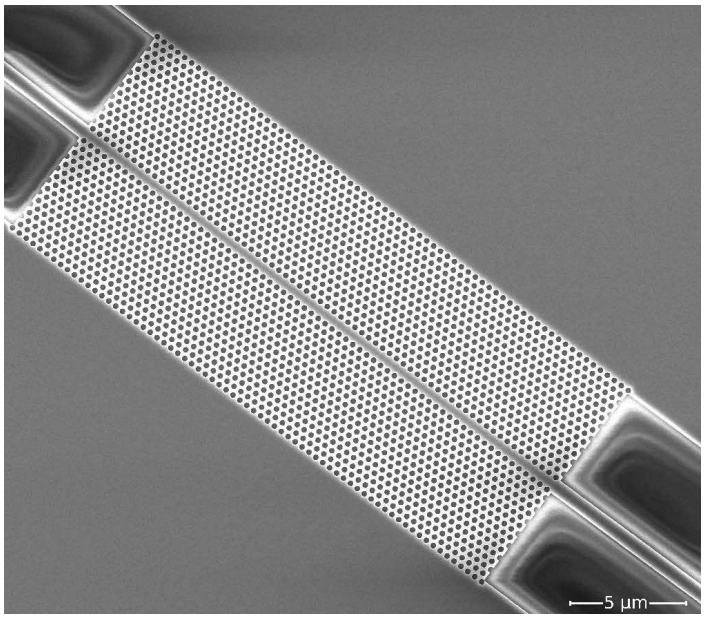

CHAPTER 2

Introduction to 2D photonic crystal components

In 1887 Lord Rayleigh was the first to study the propagation of electromagnetic waves in periodic media. He noticed peculiar reflective properties of a crystalline mineral with periodic twinning planes. These periodic planes correspond to one-dimensional photonic crystals, and he identified a narrow bandgap prohibiting light propagation through the planes. Since it is a one-dimensional periodicity, the bandgap is angle-dependent and it produces a reflected color that varies sharply with angle. This effect can often be observed in nature such as on butterfly wings (Fig. 2.1(a)). Multilayer films (or more commonly called thin films) have experienced intensive study during the last century and this technology can be found in many commercial products nowadays such as thin films mirrors and filters. It took 100 years before the concepts of omnidirectional photonic bandgaps were extended to two (Fig. 2.1(b)) and three (Fig. 2.1(c)) dimensions by Yablonovitch [11] and John [12] in 1987. This extension of the principle, which joined the tools of electromagnetism and solid-state physics, led to the name of *photonic crystals*. This field of research has undergone major developments during the last 20 years in the fabrication, the theory, as well as the different applications, from integrated optics to negative refraction and optical fibers that guide light in air.

(a)

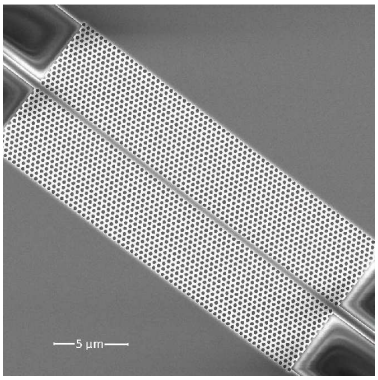

(b)

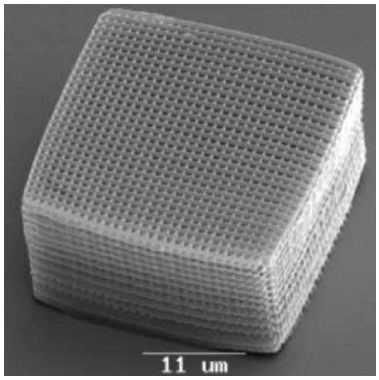

(c)

Figure 2.1: (a) Picture of a blue morpho butterfly, which has periodically structured wings (From [13]). (b) 2D photonic crystal waveguide. (c) 3D photonic crystal (From [14]).

More specifically, 2D photonic crystals are believed to be of great potential to lead to specific integrated optical devices with nanoscale features. Components based on this concept have been one of the major centers of interest in integrated optics in the last few years and they have experienced major improvements. This progress is mainly due to better

fabrication techniques and design of these components. Many optimisation methods have been applied to photonic crystal waveguides in order to improve their broadband performances. One of these methods, called topology optimisation, originally developed in mechanical engineering, was used for improving the transmission properties of photonic crystal waveguide components [15]. Even though the results have been greatly improved, performances are still lower than for more conventional ridge waveguides of comparable size, fashionably called photonic wires [5,16].

More recently research has been reoriented in a more focused way towards distinct characteristics of photonic crystal waveguides such as, for example, the unique dispersion properties of these devices, which can lead to a reduction of the group velocity of light by a factor of 200 to 300 [7, 17]. A reduction of the group velocity of light means an enhancement of light-matter interactions and different groups have taken advantage of this feature to obtain optical modulation in silicon [7, 8]. Nevertheless, issues like propagation and coupling losses still need to be addressed to improve the overall response. In this regard, topology optimisation has been used to decrease the propagation loss in photonic crystal 60° bend waveguides and to also decrease the in-coupling loss to the slow light mode in photonic crystal waveguides.

In order to understand better theses subjects, the theory of photonic crystal components and an introduction to the topology optimisation method will be detailed in the next chapter. This will be followed by details of the fabrication and characterisation of 2D photonic crystal structures. Chapter 6 will present the different results concerning 2D photonic crystal waveguides obtained during this project. This includes a discussion on the propagation of TM-polarised light in photonic crystal components topology-optimised for TE polarisation, and the optimisation of in-coupling to the slow-light regime and the propagation of slow-light in photonic crystal 60° bend waveguides.

CHAPTER 3

Modeling of 2D photonic crystal components

In a crystalline material like a semiconductor, the periodic potential, as depicted in Fig. 3.1(a), creates an electronic bandgap in which no electronic state exists. The optical analogy is photonic crystals (PhC), where the periodicity of the dielectric constant of the material (Fig. 3.1(b)) opens a photonic bandgap (PBG), i.e. a range of frequencies for which no optical state exists. This phenomenon arises when the periodicity of the dielectric constant is of the order of the wavelength of the electromagnetic wave propagating in the material.

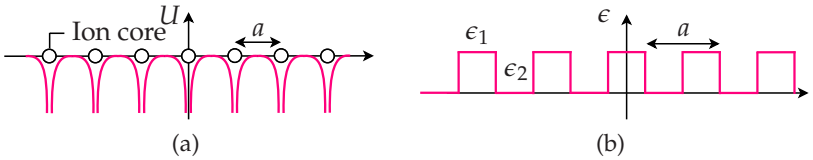

Figure 3.1: Periodic (a) potential and (b) modulation of the dielectric constant.

In order to describe and understand the propagation of light in a periodic medium such as PhC, the so-called Maxwell's equations are used.

They relate, through differential equations, the time- and space-dependent electric field (**E**), magnetic field (**H**), and the density of free charges (ρ) and currents (**J**). They take the following form:

$$\nabla \cdot \epsilon \mathbf{E}(\mathbf{r},t) = \rho(\mathbf{r},t) \quad (3.1)$$

$$\nabla \cdot \mu \mathbf{H}(\mathbf{r},t) = 0 \quad (3.2)$$

$$\nabla \times \mathbf{E}(\mathbf{r},t) = -\mu \frac{\partial \mathbf{H}(\mathbf{r},t)}{\partial t} \quad (3.3)$$

$$\nabla \times \mathbf{H}(\mathbf{r},t) = \mathbf{J}(\mathbf{r},t) + \epsilon \frac{\partial \mathbf{E}(\mathbf{r},t)}{\partial t} \quad (3.4)$$

where μ and ϵ are respectively the permeability and the permittivity of the material. Some simplifications can be made in the present case since the type of materials serving as a platform for PhC presented in this thesis are non-magnetic, isotropic, and their losses are negligible. Moreover, the materials are dispersionless, which means that μ and ϵ are real functions independent of field magnitude, direction, and frequency. Furthermore, no free current and charge are present ($\rho = 0$, $\mathbf{J} = 0$). Finally, the field energy is considered low so that the material is in the linear regime. Maxwell's equations therefore reduce to:

$$\nabla \cdot \epsilon \mathbf{E}(\mathbf{r},t) = \nabla \cdot \epsilon_0 \epsilon_r(\mathbf{r}) \mathbf{E}(\mathbf{r},t) = 0 \quad (3.5)$$

$$\nabla \cdot \mu_0 \mathbf{H}(\mathbf{r},t) = 0 \quad (3.6)$$

$$\nabla \times \mathbf{E}(\mathbf{r},t) = -\mu_0 \frac{\partial \mathbf{H}(\mathbf{r},t)}{\partial t} \quad (3.7)$$

$$\nabla \times \mathbf{H}(\mathbf{r},t) = \epsilon \frac{\partial \mathbf{E}(\mathbf{r},t)}{\partial t} = \epsilon_0 \epsilon_r(\mathbf{r}) \frac{\partial \mathbf{E}(\mathbf{r},t)}{\partial t} \quad (3.8)$$

where ϵ_0 is the permittivity in free space and $\epsilon_r(\mathbf{r})$ is the dielectric constant of the material. In the case of PhC, there is a discrete translational symmetry of the dielectric constant, that is it is invariant under translation of distances that are a multiple of a fixed length, which is called the lattice constant **a** (see Fig. 3.1(b)). Because of this symmetry, the dielectric constant can be written as:

$$\epsilon_r(\mathbf{r}) = \epsilon_r(\mathbf{r} + l\mathbf{a}) \quad (3.9)$$

where l is an integer.

Given Eq. 3.9, Eq. 3.5-3.8 can rarely be solved analytically. The next two sections will present two different numerical methods used to solve Eq. 3.5-3.8 for PhC structures. The first approach, called *plane-wave expansion method*, gives the modal distribution of the field and the dispersion diagram of a PhC structure. The second approach, the *finite-difference time-domain method*, is used to obtain the propagation in time and space of the electromagnetic fields. Both methods will then be applied to a perfect PhC and a PhC waveguide. Finally, the optimisation method relevant to this thesis, called topology-optimisation, will be introduced.

3.1 Plane-wave expansion method

In the frequency domain, one set of solutions of Maxwell's equation are monochromatic electromagnetic waves, which are harmonic functions of time t of a given angular frequency ω. The electric and magnetic field can thus be separated into a spatial- and time-dependent part:

$$\mathbf{E}(\mathbf{r},t) = \mathbf{E}(\mathbf{r})e^{i\omega t} \tag{3.10}$$

$$\mathbf{H}(\mathbf{r},t) = \mathbf{H}(\mathbf{r})e^{i\omega t}. \tag{3.11}$$

where $\mathbf{E}(\mathbf{r})$ and $\mathbf{H}(\mathbf{r})$ are the amplitudes of the electric and magnetic fields respectively as a function of the position $\mathbf{r}$, and $e^{i\omega t}$ describes the harmonic time dependence of the fields. Substituting $\partial/\partial t$ by $i\omega$ in Eq. 3.7-3.8, dividing Eq. 3.8 by $\epsilon_r(\mathbf{r})$, and taking the curl of Eq. 3.7 and Eq. 3.8, one gets:

$$\nabla \times \nabla \times \mathbf{E}(\mathbf{r}) = \left(\frac{\omega}{c}\right)^2 \epsilon_r(\mathbf{r})\mathbf{E}(\mathbf{r}) \tag{3.12}$$

$$\nabla \times \left(\frac{1}{\epsilon_r(\mathbf{r})}\nabla \times \mathbf{H}(\mathbf{r})\right) = \left(\frac{\omega}{c}\right)^2 \mathbf{H}(\mathbf{r}) \tag{3.13}$$

with $c = 1/\sqrt{\epsilon_0\mu_0}$ the speed of light in vacuum. Unlike Eq. 3.12, Eq. 3.13 is an eigenvalue equation that governs the propagation of monochromatic light of frequency ω in a dielectric material described by $\epsilon_r(\mathbf{r})$. Therefore it is convenient to solve for $\mathbf{H}(\mathbf{r})$[1] and then determine $\mathbf{E}(\mathbf{r})$ via Eq. 3.7 [18].

[1] Since the operator acting on $\mathbf{H}(\mathbf{r})$ is Hermitian, it simplifies the problem to solve for the magnetic field.

The *master equation* (Eq. 3.13) has orthogonal solutions each having real eigenvalues $(\frac{\omega}{c})^2$.

Because of the periodicity of the dielectric constant for PhC, Bloch's theorem can be applied. It states that for any kind of periodic dielectric constant variations (Fig. 3.1(b)) the solutions to the master equation are of the form $\mathbf{H}(\mathbf{r}) = e^{i\mathbf{k}.\mathbf{r}} u_{n,\mathbf{k}}(\mathbf{r})$ with eigenvalues $\omega_n(\mathbf{k})$. $\mathbf{u}_{n,\mathbf{k}}(\mathbf{r})$ is an envelope function with the periodicity of the photonic crystal lattice satisfying:

$$(\nabla + i\mathbf{k}) \times \frac{1}{\epsilon_r(\mathbf{r})}(\nabla + i\mathbf{k}) \times \mathbf{u}_{n,\mathbf{k}}(\mathbf{r}) = \left(\frac{\omega_n(\mathbf{k})}{c}\right)^2 \mathbf{u}_{n,\mathbf{k}}(\mathbf{r}) \qquad (3.14)$$

where $\mathbf{k}$ is the Bloch wave vector and $n = 1, 2, \ldots$ is an index that labels the discrete eigenvalues. These eigenvalues $\omega_n(\mathbf{k})$ are continuous functions of $\mathbf{k}$, forming discrete *bands* in a dispersion diagram.

In the plane-wave expansion (PWE) method the solutions of Eq. 3.13 are expanded in a truncated basis of plane waves. These plane waves can easily be expressed as a Fourier expansion series in k-space (reciprocal space), which facilitates the computation. In order to obtain the dispersion diagram presented in this thesis, the freely available programme "MIT Photonic-Bands" (MPB) was utilised [19]. MPB is a fully-vectorial eigenmode solver of Maxwell's equations with periodic boundary conditions. To model a PhC structure defined by hexagonal lattice of air holes in a high dielectric material, the unit cell depicted in Fig. 3.2(a) with a dashed red line is repeated infinitely in space, following the primitive vectors $\mathbf{a_1}$ and $\mathbf{a_2}$. Because of the symmetry of the structure, the modal distribution and the dispersion relation $\omega_n(\mathbf{k})$ for the structure can be found by applying the plane-wave expansion to the unit cell. Moreover, since the symmetry holds also in the k-space, it is sufficient to compute the solutions of Eq. 3.14 along the high-symmetry points Γ, M, and K of the irreducible Brillouin zone (Fig. 3.2(a)).

Moreover, this method also allows the computation of the modal distribution and the dispersion relation of PhC structures containing defects. To obtain a PhC waveguide, one has simply to create a defect line by removing one or more rows of holes in the Γ-K direction. A supercell approximation is adopted in order to model this kind of structure. It consists of defining a supercell, i.e. a matrix of $n \times m$ unit cells as illustrated in Fig. 3.2(b). The defect, in this case the waveguide, is created by omitting the hole in one of the unit cells of the supercell. The supercell

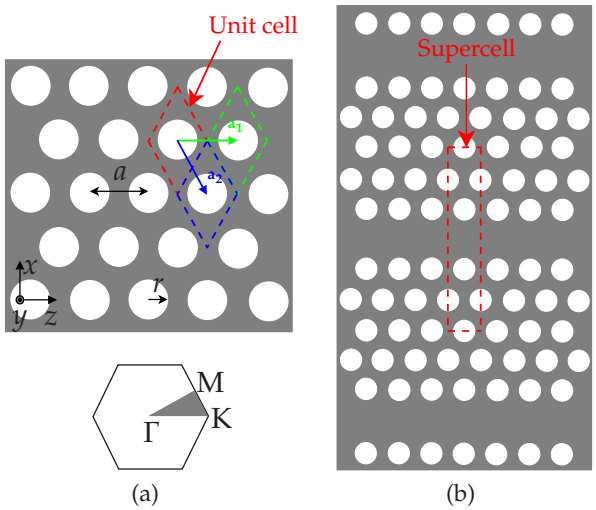

Figure 3.2: (a) Schema of a 2D PhC of hexagonal lattice of air holes in a high dielectric material. The unit cell, depicted by the red dashed diamond, is repeated infinitely along the primitive vectors $\mathbf{a_1}$ and $\mathbf{a_2}$. Its first Brillouin zone, with the high symmetry points, is shown underneath. (b) A 2D PhC waveguide defined by the repetition of a supercell.

is then repeated infinitely in space, giving a modelled structure having an infinite number of waveguides. It is therefore important to define a supercell big enough so that there is no coupling between the different waveguides. A 1×11 was found to be an appropriate choice to model a PhC waveguide [20]. Since the symmetry of the structure is broken by the introduction of a line defect, the translational symmetry persists only along the line defect. The $\mathbf{k}$ vectors are then projected onto this direction and the solutions of Eq. 3.13 for the waveguide structure are found only along the Γ-K direction.

3.2 Finite-difference time-domain method

In order to know how the electromagnetic fields are propagating in space and time in a PhC structure, the finite-difference time-domain (FDTD) modelling method is used. Unlike the plane wave expansion method, FDTD is a time domain method, from which transmission and reflec-

tion of a structure over a broad range of frequencies can be obtained. The method is widely use to model PhC structures since it is flexible as regard to the geometry of the structures and can handle large index variations [21]. The idea behind the technique is to discretise the time-dependent Maxwell's equation using central-difference approximations to the space and time partial derivatives. The structure under investigation is divided into a finite lattice of grid points, and the finite-difference equations are solved at these grid points for a given instant in time. The computation is repeated for each time step.

By applying a simple centered difference approximation to the derivatives of Eq. 3.8, one gets the following finite difference equation:

$$\frac{H^n_{i+1,j} - 2H^n_{i,j} + H^n_{i-1,j}}{(\Delta s)^2} + \frac{H^n_{i,j+1} - 2H^n_{i,j} + H^n_{i,j-1}}{(\Delta s)^2} = \mu_0 \epsilon_{ij} \frac{H^{n+1}_{i,j} - 2H^n_{i,j} + H^{n-1}_{i,j}}{(\Delta t)^2} \quad (3.15)$$

where i, j correspond to indices of the grid points in space separated by Δs and n corresponds to the indices of the time steps, separated from each other by Δt. Only derivatives of the magnetic field in the plane (xz) are kept since the solutions looked for are in the plane of the photonic crystal (see Fig. 3.2(a)). A similar derivation can be made for the electric field. By a careful choice of initial field vector (usually a Gaussian distribution), the future component of the magnetic field $H^n_{i,j}$ can be computed. Moreover, special boundary conditions, called perfectly matched layer (PML), need to be applied at the edges of the modelled structure in order to absorb light and avoid unwanted reflections back into the structure.

In this thesis, the commercially available software CrystalWave from the company Photon Design [22] was used in order to gain information on the wave propagation in the designed PhC components. This modeling technique has been described in more detail elsewhere [23–25].

3.3 Photonic crystal structures

The 2D photonic crystal of interest to this work, which is made on a silicon-on-insulator (SOI) platform, is illustrated in Fig. 3.3. The lattice of air holes defining the PhC is etched in the top silicon layer that is typically $\sim$300 nm thick while the buried oxide layer is between 1 and 3 μm

thick. This configuration, often called the slab configuration, gives a confinement of the mode via photonic bandgap in the plane (xz) and via total internal reflection in the out of plane direction (y). For SOI-based 2D PhC operating in the telecommunication window ($\sim$1550 nm), the lattice constant is usually around $a = 400$ nm while the radius of the holes can be varied between $0.25-0.4a$. The following sections describe the behavior of photonic crystal structures with the help of the modeling techniques presented previously. A perfect photonic crystal, a PhC waveguide, and the different group velocity regimes will be described.

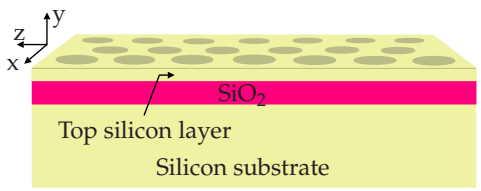

Figure 3.3: 3D sketch of a 2D PhC made on a SOI platform.

3.3.1 Perfect photonic crystal

In a 2D PhC, the electromagnetic fields can be classified into two distinct polarisations:

Transverse magnetic (TM) The magnetic field has field components in the xz-plane ($\mathbf{H} = (H_x, 0, H_z)$) while the electric field is perpendicular ($\mathbf{E} = (0, E_y, 0)$);

Transverse electric (TE) The electric field has field components in the xz-plane ($\mathbf{E} = (E_x, 0, E_z)$) while the magnetic field is perpendicular ($\mathbf{H} = (0, H_y, 0)$).

Figure 3.4 shows the dispersion diagram ($\omega_n(\mathbf{k})$) for a perfect 2D PhC for both TE and TM polarisations calculated with the PWE in two dimensions[2] along the high symmetry points Γ, M, K. Due to the approximate scalability of Maxwell's equation [18], it is common to express the frequency in normalised units. The normalised frequency is then defined as a/λ.

[2]The structure is infinite in the out of plane direction (y).

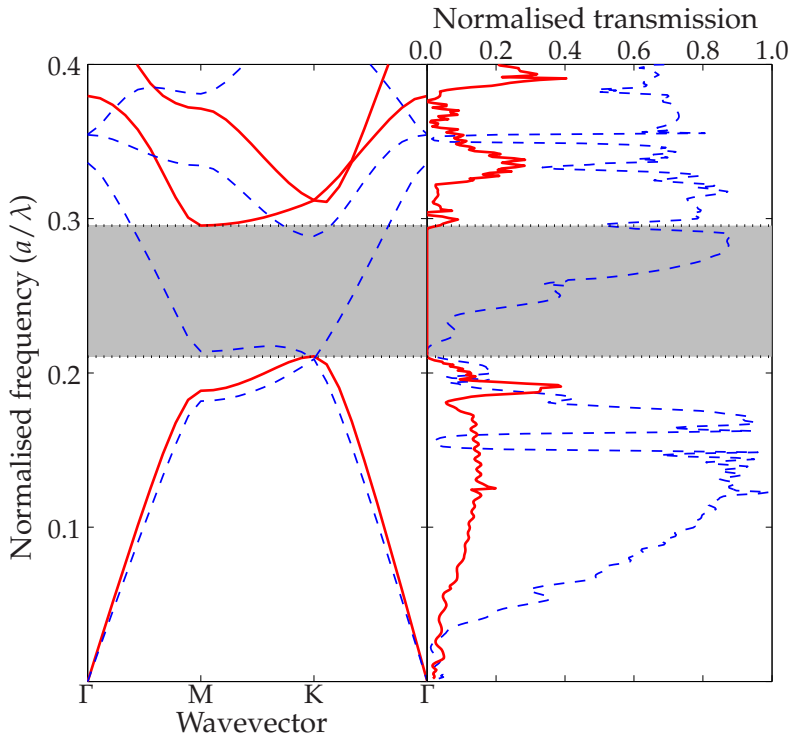

Figure 3.4: Left: Dispersion diagram of a perfect 2D photonic crystal calculated using the PWE method. Air holes are defined in silicon ($\epsilon = 12.083$) in a triangular lattice where the radius of the holes is $r = 0.325a$. Right: Transmission through the same photonic crystal in the Γ-K direction obtained by 2D FDTD method. The behavior for both polarisations (TE: plain red and TM: dashed blue) is shown. The shaded area corresponds to the PBG for the TE polarisation.

The modelled structure behind Fig. 3.4 is a triangular lattice of air holes in silicon ($\epsilon = 12.083$), where the radius of the holes is $r = 0.325a$. This structure presents a complete PBG for the TE polarisation, illustrated by the shaded rectangle in Fig. 3.4, i.e. no optical TE mode exists for this normalised frequency range ($0.21-0.295$). For the TM polarisation, there is no PBG. It is possible to obtain an omnidirectional PBG for both TE and TM polarisations. However the conditions to obtain a PBG are different for the two polarisations [18] making is difficult to fabricate such a com-

ponent. Since the triangular lattice of air holes in silicon presents a large bandgap for the TE polarisation, the fabricated structures presented in this thesis have been designed for this polarisation. Other configurations presenting PBG for TE- or TM-polarised light can be found elsewhere [18].

The right part of Fig. 3.4 shows the normalised transmission through the structure described above for both polarisations in the Γ-K direction, calculated with the FDTD method in two dimensions. While the TM-polarised light is transmitted trough the structure for almost all frequencies, the TE-polarised light is blocked in the frequency range corresponding to the PBG for the TE polarisation, confirming the results obtained with the PWE method.

3.3.2 Photonic crystal waveguide

As described previously, a PhC waveguide is obtained by introducing a line defect in the otherwise perfect crystal (see Fig. 3.2(b)). By doing this, several *guided* modes are introduced in the dispersion diagram.

In Fig. 3.5 the dispersion diagram for a PhC waveguide, formed by removing one row of holes, calculated with the PWE method, is presented. The parameters of the structure (r, ϵ) are the same as in the previous section and the structure was modelled with a supercell containing 1×11 unit cells. The shaded zones correspond to allowed modes in the crystal. These modes are therefore not confined in the line defect and they are called slab modes. The slab modes would be the only ones present in the dispersion diagram in the absence of the line defect. The introduction of the line defect gives rise to 7 defect bands. They correspond to the plain curves in the dispersion diagram. The 3 green curves under the first slab modes region represent modes that are purely index-guided, while the red and blue curves are referred to as PBG modes. The PBG modes are labeled even (red curves) and odd (blue curves) depending on the parity of the magnetic field with respect to the direction of propagation. The mapping of the fundamental even and odd modes at $ka/2\pi = 0.2$ are illustrated in Fig. 3.6 where the color difference signifies that the intensity of the field is of different sign with respect to the out of plane direction (y). As opposed to the other PBG modes, the fundamental even mode presents a large bandwidth in the PBG and also an even field distribution similar to the one of the fundamental mode of an index-guided waveguide, which makes it attractive and easy to couple to.

The right part of Fig. 3.5 shows the transmission of TE-polarised light through a 10 μm long waveguide with $r = 0.325a$ obtained by 2D FDTD

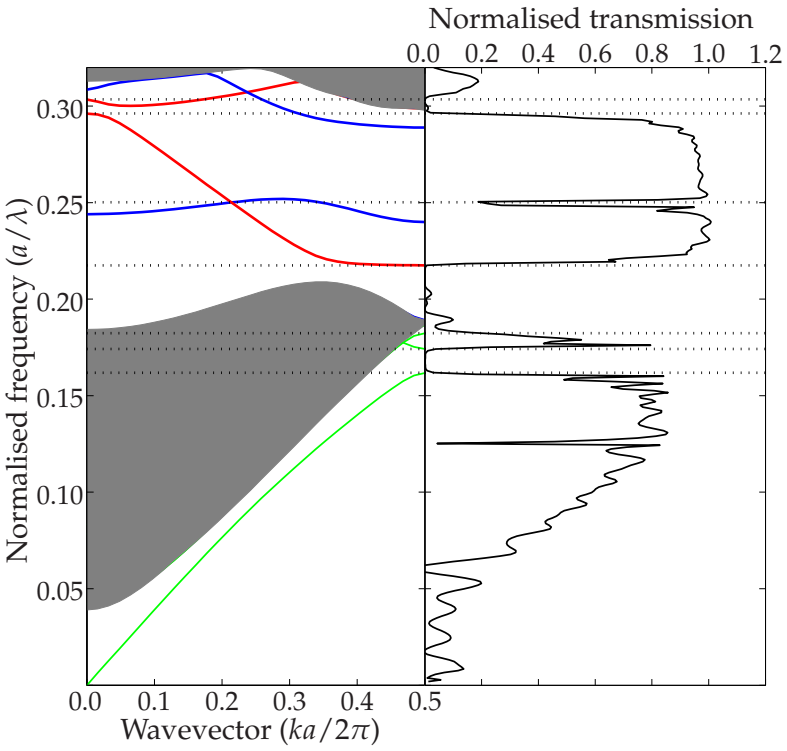

Figure 3.5: Left: Dispersion diagram for the TE polarisation of a 2D PhC waveguide calculated using the PWE method. Air holes are defined in silicon ($\epsilon = 12.083$) in a triangular lattice where the radius of the holes is $r = 0.325a$. The waveguide is obtained by removing one row of holes in the Γ-K direction. Right: Transmission through the same PhC waveguide in the Γ-K direction obtained using 2D FDTD method.

(a) Even (b) Odd

Figure 3.6: Mapping of the y component of the magnetic field H_y for the two fundamental modes of a photonic crystal waveguide at $ka/2\pi = 0.2$: (a) even mode and (b) odd mode.

simulation. It can be seem that the features in the spectrum are directly related to features in the dispersion diagram. First of all, the index-guided modes below the first slab modes region allow light to propagate in the structure up to a frequency of 0.18. One can also relate the very low transmission through the structure between 0.18 and 0.22 to the absence of guided modes in the dispersion diagram for this frequency range. Futhermore, the high transmission in the frequency range $0.22-0.295$ can be correlated to the fundamental even mode in the dispersion diagram. The high and low frequency cutoffs correspond well in both cases. The transmission above 0.3 can be associated with the second order even mode of this structure. Moreover, the dip in transmission at 0.25 is connected to an artificial coupling between the fundamental even and odd mode occuring due to the finite discretisation of the structure in the FDTD simulation [25]. Increasing the resolution in the FDTD calculation will reduce the numerical coupling. However coupling between these two modes having different parity can be experimentally observed [26]. This theoretically forbidden coupling is allowed by structure imperfections, such as sidewall roughness and irregularities, or by vertical asymmetry like in the case of SOI-based structures.

When modelling fabricated 2D PhC components, one has to take into account the third dimension. The lack of translational symmetry in the vertical direction has several consequences. The first one concerns the polarisation states, which are not purely TE and TM modes anymore. However, they can still be classified as being even or odd as introduced earlier. These even and odd modes have strong similarities with TE- and TM-modes, respectively. Therefore, they are often referred as TE- and TM-like modes. For simplicity, these modes will be referred as being TE- and TM-polarised.

The second consequence of the broken symmetry in the vertical direction is that the bands in the dispersion relation are shifted to higher frequencies, as shown in Fig. 3.7. This is due to a decrease in the effective dielectric constant seen by the mode, because of the lower dielectric constant of air and silica as respect to silicon. The modelled structure is a 320 nm silicon slab, sandwiched between a layer of air and one of silica, in which there is a triangular lattice of air holes having $r = 0.325a$. Because of the different guiding mechanism in the third dimension, the dispersion relation of the material surrounding the slab has to be taken into account. In Fig. 3.7, the air-dispersion relation (air line) and the silica-dispersion relation (silica line) are indicated. All combinations of $(k, a/\lambda)$

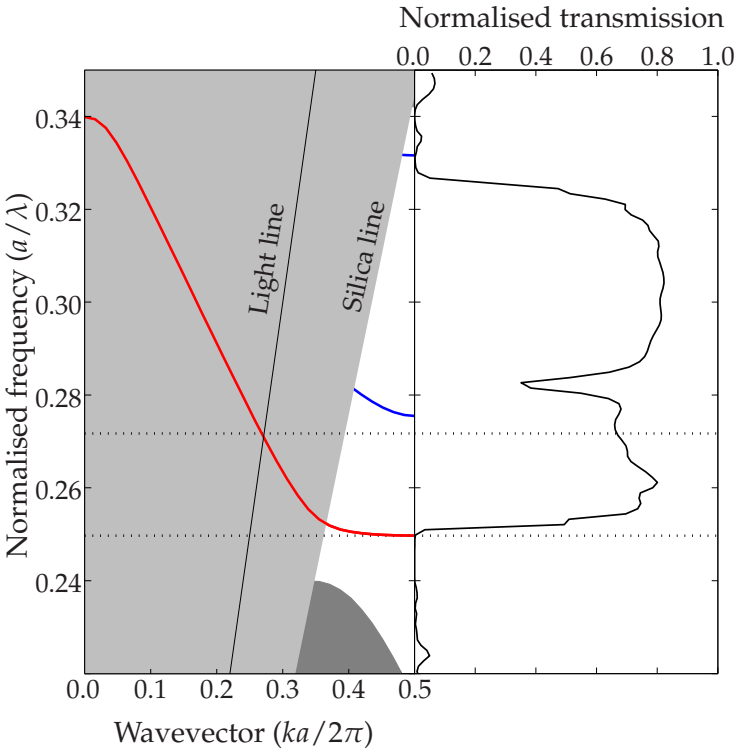

Figure 3.7: Left: 3D dispersion diagram for the TE polarisation of a 2D PhC waveguide calculated using the PWE method. Air holes are defined in a 320 nm thick silicon slab ($\epsilon = 12.083$) in a triangular lattice where the radius of the holes is $r = 0.325a$. The waveguide is obtained by removing one row of holes in the Γ-K direction. The silicon slab is sandwiched between a layer of air and one of silica. Right: Transmission through the same PhC waveguide in the Γ-K direction obtained using 3D FDTD method with a resolution of $a/24$.

above the air (silica) line are allowed in air (silica). Therefore, to minimise the coupling to the substrate modes, $(k, a/\lambda)$ should be chosen below the corresponding substrate line. It is easy to conclude that the air-silicon-air (membrane) configuration gives a larger bandwidth in the leakage-free region. For this reason, the membrane configuration has attracted a lot of attention as a platform for low-loss PhC waveguides. Futhermore, the bandwith under the silica line can be increased by reducing the core

of the PhC waveguide by 30% [20], but the resulting structure may not present the same slow-light regime behavior (see section 3.3.3).

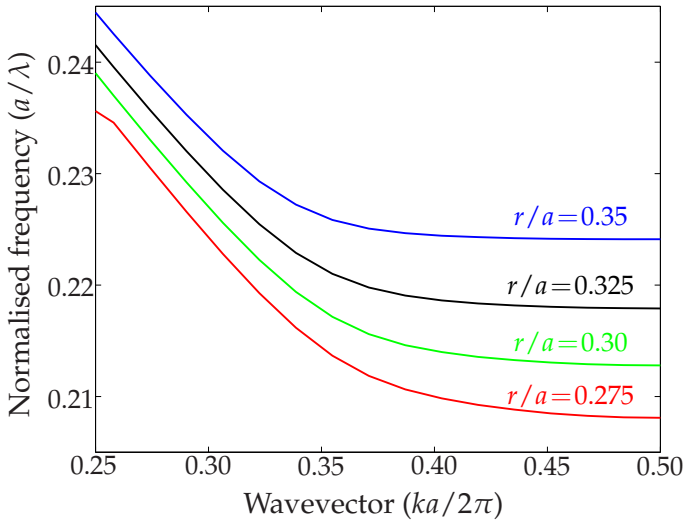

Figure 3.8: Shift in frequency of the fundamental PBG mode of a PhC waveguide as a function of the radius of the holes.

The right part of Fig. 3.7 shows the transmission through a 10 μm long waveguide calulated by 3D FDTD simulation with the same parameters as for the dispersion diagram calculation. Due to the difference in the vertical boundary conditions between the two modeling techniques, a shift of 1% in normalised frequency was applied to the 3D FDTD spectrum in order to match the low frequency cutoff of the dispersion diagram. Normally a narrow frequency window should be transmitted through the waveguide since a small portion of the fundmental even mode lies under the silica line. However, the relatively short length of the waveguide explains the high broadband transmission. The artificial even-odd coupling can also be seen. Futhermore, a higher transmission in the silica-only leaking region can be seen. The transmission drops at frequency higher than 0.27 since there is leakage in both silica and air.

A lot of parameters have to be taken into account while designing PhC waveguides. In order for the interesting features of a component to lie in the right frequency range without suffering too much loss, tuning of the PhC is often required. The top silicon layer of the SOI platform is usually fixed, but one can play with the size and spacing of the holes.

As an example Fig. 3.8 shows the frequency shifting of the fundamental mode of a PhC waveguides by increasing the size of the holes. Since the effective dielectric constant of the top silicon layer decreases when increasing the size of the holes, the mode is shifted to higher frequencies. The holes can also be enlarged by oxidising a sample after fabrication [27] leading to a shift to higher frequency, thus enabling a post fabrication tuning of the structures.

3.3.3 Group velocity regimes

One interesting feature of a photonic crystal waveguide is its nonlinear dispersion relation leading to low group velocity. As opposed to conventional index-guiding silicon waveguide for which the dispersion relation of the modes is a straight line ($\omega = ck$), the modes of a photonic crystal waveguide have a different behavior as described in the previous sections. It is well known that from the dispersion relation, one can obtain the group velocity:

$$v_g = \frac{\partial \omega}{\partial k}. \tag{3.16}$$

The group velocity of the modes is a function of k and can be obtained by differentiating the dispersion relation of the modes. Figure 3.9(a) shows the dispersion relation (plain green curve) and the group velocity (dashed blue curve) for the fundamental PBG mode of a photonic crystal waveguide. By inspection of Fig. 3.9, one can see that the spectrum can be divided into two regimes: one where v_g is almost constant for $ka/2\pi \in [0.1, 0.3]$ (linear regime) and one where v_g is reduced considerably for $ka/2\pi \in [0.35, 0.5]$ (slow-light regime). In the linear regime, the group velocity is approximatively one fourth of what it would be in vacuum, which corresponds well with the effective index of refraction of an index-guided mode in a conventional silicon waveguide. The mapping of the magnetic field H_y (Fig. 3.9(b)) shows that the mode is well confined in the core just like it is for an index-guided mode. On the other hand, as the mode approaches the end of the Brillouin zone the group velocity tends to zero and the mode penetrates deep into the PhC, as shown in Fig. 3.9(c). This slow-light phenomenon originates from the periodic dielectric constant around the waveguide core and has attracted a lot of interest since its potential applications range from optical buffering [28] and low threshold lasing [29] to optical switching [7].

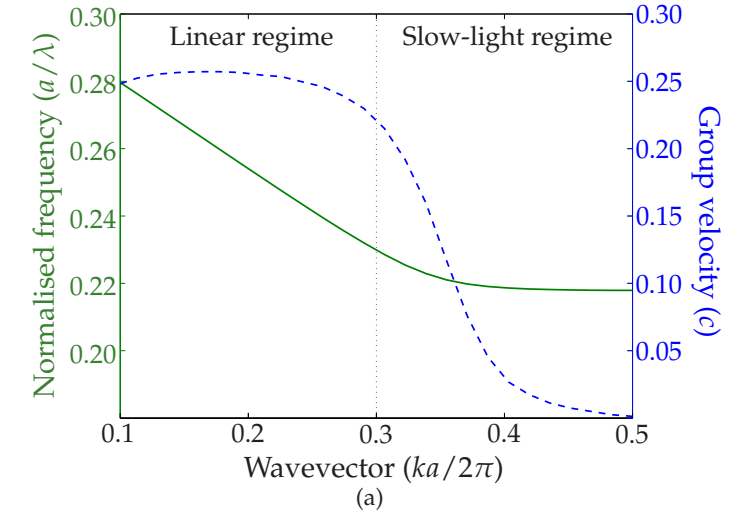

(a)

(b) $ka/2\pi = 0.25$ (c) $ka/2\pi = 0.5$

Figure 3.9: (a) Dispersion relation (plain green) and group velocity (dashed blue) of the fundamental PBG mode. (b) and (c) show the mapping of the y component of the magnetic field H_y for the PBG fundamental mode at two different wavevectors corresponding to the two different regimes.

3.4 Topology optimisation

The design and optimisation of PhC components are not intuitive. An impressive number of publications can be found in the literature in which researchers describe optimised structures obtained by moving and/or re-shaping parts of a PhC component in an iterative trial-and-error procedure (see [30,31] for examples). This kind of approach is time-consuming, non-trivial, and there is no guarantee that the structures found are optimal. Hence, it motivated the interest in applying inverse design optimisation strategies for PhC components [32–35], where an objective function is passed on to an algorithm which returns a distribution of the dielectric constant that fullfill the objective. The technique presented in this thesis is called *Topology Optimisation Method*. This method was first employed in mechanical engineering to optimise structures such as airplanes and bridges [36] by rearranging a minimum of material while keeping the

stiffness of the structure as high as possible. Applied to photonic crystal waveguide structures, it consists of a free redistribution of material in a design domain in a way which maximises the transmission through the device for a given polarisation of the light [15,37,38]. The method will be described for the optimisation of 60° bends for the slow-light regime.

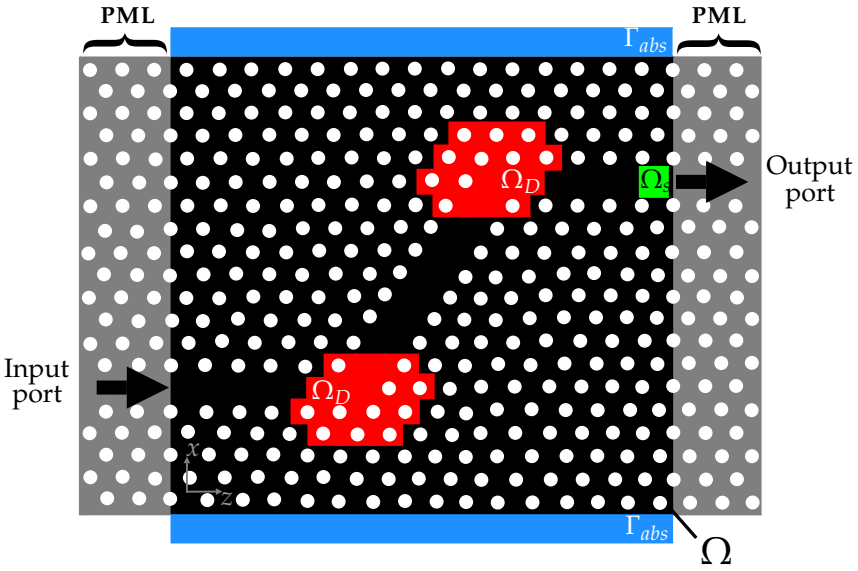

Figure 3.10: Sketch of a photonic crystal waveguide containing two consecutive 60° bends where design domains (red) have been chosen for the topology optimisation.

The algorithm is based on the two-dimensional Helmholtz equation in a discretised domain, Ω. For TE-polarised light, the wave equation is:

$$\nabla \cdot \left(\frac{1}{\epsilon_r(\mathbf{x})} \nabla u(\mathbf{x}) \right) + \frac{\omega^2}{c^2} u(\mathbf{x}) = 0 \qquad \text{in } \Omega \tag{3.17}$$

where $u(\mathbf{x})$ is the unknown field in the plane $\mathbf{x} = (x, z)$. In the particular case depicted in Fig 3.10, the domain consists of a repetition of unit cells in a triangular lattice. The unit cell is composed of an air hole of radius $r = 0.3a$ in silicon ($\epsilon_d = 12$). As explained in the previous sections, this configuration shows a band gap for the TE polarisation. Two 60° bends are created by removing a single row of holes as shown in Fig 3.10.

An incident wave is then specified at the input port of the structure and absorbing boundary conditions (Γ_{abs}) are defined at the top and the bottom of the design domain Ω. In order to eliminate reflections at the input and output ports of the waveguide, anisotropic PML are added. In these layers, complex functions governing the damping are taken into account in the resolution of Helmholtz equation. A finite element procedure is applied to the structure leading to a discretised set of equations:

$$\mathbf{S}(\epsilon_r^{-1}(\mathbf{x}), \omega)\mathbf{u} = \mathbf{f}(\omega) \tag{3.18}$$

where $\mathbf{f}(\omega)$ is the wave input vector, $\mathbf{S}$ is the frequency-dependent system matrix, and $\mathbf{u}$ is the vector for which the equation will be solved. The discretisation of the domain has to be sufficiently detailed to obtain the response of the structure for a given frequency with enough accuracy, and sufficiently small so that the calculation is fast and can be used in the iterative optimisation algorithm.

The domains in which a redistribution of the material will take place are called design domains Ω_D. They are subdomains of Ω, as indicated by the red area in Fig 3.10, in which each finite element is attributed a design parameter x_e such that the element-wise dielectric constant in the design domains is:

$$\epsilon_e^{-1} = 1 + x_e(\epsilon_d^{-1} - 1) \tag{3.19}$$

where

$$x_e \in \Re, \qquad 0 \leq x_e \leq 1. \tag{3.20}$$

In that way, with $x_e = 0$ the material in the element will be air and with $x_e = 1$ it will be silicon. The design parameter x_e is a continuous variable, allowing the use of a gradient-based optimisation strategy.

Next, the optimisation is applied to the defined system by redistributing the material in the design domains Ω_D in order to maximise the Poynting vector through the area Ω_s in Fig 3.10. The objective function for the optimisation is thus the component of the Poynting vector in the output direction P^{out} averaged over all finite elements in the domain Ω_s:

$$P^{out} = \frac{1}{N} \sum_{e \in \Omega_s} P_e^{out} \tag{3.21}$$

where N is the total number of elements in the domain Ω_s. The optimi-

sation problem can then be formulated as:

$$\max_{x_e} P^{out}(\omega) \tag{3.22}$$

The transmitted light through the structure is calculated for a given initial distribution x_e and sensitivity analysis is used in order to determine how the changes in the design parameter x_e affect the objective function (Eq. 3.21). The sensitivity analysis is done by differentiating the objective function with respect to the design parameter $\frac{\partial P^{out}}{\partial x_e}$. A numerical method of moving asymptotes [39] suggests a improved transformation of the design parameter x_e for which the objective function and sensitivity analysis can be recalculated. The procedure is repeated until there is no significant changes of the design parameter between successive iterations.

Two additional features are added to the optimisation procedure [38]. First, in order to avoid undesired local extrema, an artificial damping is introduced to smooth the dynamic response of the structure. Secondly, since the design parameter x_e is a continuous variable, the resulting optimised structure can contain *gray elements*, that is elements having a dielectric constant in between the one of air and silicon, which makes the optimised structure impossible to fabricate. A damping term is introduced in the design parameter inducing energy loss for elements $0 < x_e < 1$ and hence be costly for the objective function. This parameter is typically set to a low value at the beginning of the optimisation in order to allow for a redistribution of the material and gradually increased as an optimised structure is reached.

The topology optimisation method has successfully been used to optimise photonic crystal components like 60° bends [40], 90° bends [41], and Y-splitter [42]. The optimisation algorithm was developped by Ole Sigmund and Jakob S. Jensen at MEK•DTU [43]. They implemented their algorithm into a software package called *TopOpt*, which was used to optimised the PhC components presented in this thesis.

3.5 Summary

The aim of this chapter was to introduce the principle of photonic crystal and photonic crystal waveguide in a SOI-based configuration. It was accomplished with the help of two different modeling techniques based on Maxwell's equations: the plane-wave expansion method and the finite-

difference time-domain method. The first method gives the electromagnetic field distribution in the structure together with the dispersion relation, which can be correlated with the transmission spectra through the structure obtained by the second method. The configuration of air holes arranged in a triangular lattice in silicon shows a photonic band gap for TE-polarised light. Futhermore, a PhC waveguide is obtained by removing one row of holes in an otherwise perfect crystal. By doing so photonic band gap guided modes are introduced in the dispersion diagram. The fundamental even PBG mode presents a significant bandwidth under the air line, which limits the leakage of the mode in the substrate. Moreover, this mode can be scaled in frequency by changing the size of the holes of the photonic crystal surrounding the waveguide. Another important feature of the even mode is that it can be divided into two different group velocity regimes: the linear regime for which the mode behaves just like an index-guided mode and a slow-light regime where the group velocity of the mode tends to zero at the edge of Brillouin zone. The knowledge of the electromagnetic field distribution in the photonic crystal waveguide for the slow-light regime, was exploited in the optimisation of the components that will be presented in chapter 6.

CHAPTER 4

Fabrication of 2D photonic crystal components

The fabrication of 2D PhC presents techonological challenges since the size of the features are down to a few tens of nanometer for operation in the telecommunication window (∼1500 nm). High-resolution lithography and anisotropic etching are required in order to reach this resolution. Conventional photolithography using ultraviolet light (∼365 nm) is insufficient as the feature size for dense patterning is ∼600 nm. Recently, deep ultraviolet lithography, using excimer lasers (KrF operating at 248 nm), was used to fabricated PhC components [6,44–48]. The feature size achievable is just at the limit to fabricate generic PhC for the telecommunication window, but not low enough for optimised structures like cavities. The most common technique used to fabricate PhC components is electron beam lithography (EBL), followed by reactive ion etching (RIE) offering the high anisotropy required to efficiently transfer the pattern in the substrate. The PhC components presented in this thesis have been fabricated in the DANCHIP cleanroom facilities using EBL followed by RIE.

The main steps of the procedure used to fabricate the components are:

- **Design preparation:** The components required are drawn with mask editor software and converted into the EBL file format.
- **Cleaning the substrate:** The substrate is cleaned on a spin-coater (Karl

Suss RC8) with acetone, ethanol, and isopropanol, and it is finally blown-dry with N_2.

- **Spin-coating of the resist:** A ∼100 nm thick layer of resist (ZEP-520a) is spun on top of the substrate.
- **Pre-baking:** The sample is then baked for 2 min on a hotplate at 130°C, in order to remove the solvent and harden the resist.
- **Cleaving the substrate:** The substrate is cleaved in pieces of about 1.2 × 5 cm^2 in order to fit in a 2" carrier of the EBL machine and blown-dry with N_2 in order to remove any dust on the substrate.
- **EBL writing:** The pattern is written in the resist using EBL.
- **Development of the pattern in the resist:** The exposed regions are dissolved with the developer ZED-N50 for 1 minute, and the sample is rinsed 30 s with isopropanol.
- **Post-baking:** Before the etch, the sample is baked for 5 minutes on a hotplate at 110°C.
- **Dry etching:** The pattern is transferred from the resist to the top silicon layer using a dry etch.
- **Lift off of the resist:** The residual resist is removed with an oxygen plasma.
- **Cleaving the sample:** The sample is finally cleaved in order to access the waveguides.

Figure 4.1 illustrates the fabrication process. The platform used to make the silicon-based 2D PhC presented in this thesis is SOI substrate. The thickness of the top layer of silicon and the oxide are around 300 nm and 1-3 μm respectively. The wafers of SOI were bought from Soitec[1] where they are fabricated using the Smart Cut(R) technique [49]. The high resolution and high sensitivity resist ZEP-520a [2] 5.5%, diluted 1:1 in methoxybenzene to decrease its viscosity, is spun on top of the substrate. This resist is a positive tone resist, which means that the exposed regions are the ones that will be removed after the EBL process. The resulting thickness of the resist is ∼100 nm, which was found to be a good

[1] http://www.soitec.com/

[2] http://www.zeon.co.jp/business_e/enterprise/imagelec/imagelec.html

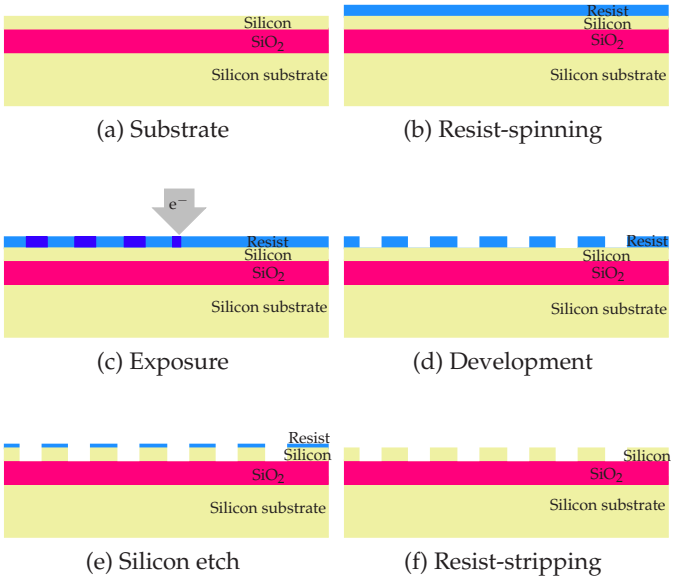

Figure 4.1: Fabrication steps for 2D photonic crystal on a SOI substrate: (a) SOI substrate, (b) spinning of the resist, (c) lithographic definition of the structure, (d) development of the resist, (e) etching process, and (f) resist stripping.

compromise to achieve a precise transfer of the pattern to the top silicon layer while being thick enough to attain enough resistance to the etching process. Prior to the EBL writing, the resist is pre-baked in order to remove the solvent and harden the resist. During the writing process, the electrons cause breakage in the resist leading to a higher solubility of the exposed regions. After the writing process, the exposed regions are dissolved with a developer (ZED-N50). The resulting patterned resist acts as a mask for the etch, i.e. the unmasked regions of the substrate are etched away, resulting in a transfer of the pattern from the resist to the top silicon layer of the SOI wafer. The following sections will discuss important issues when fabricating 2D PhC components. More details on the preparation of the files prior to the EBL writing, and the different parameters used for the EBL writing will be given. This will be followed by an introduction to the reactive ion etching processes used for the transfer of the pattern in the silicon layer.

4.1 Design preparation and EBL writing

The first step in the fabrication process is to draw the components to be written in the required EBL file format. The pattern to be written is first edited using the mask editor software L-Edit from Tanner Research[3]. Since the ZEP-520a resist is a positive resist, the design consists of holes arranged in a hexagonal lattice. It has been shown that defining the holes as dodecagons was a good compromise in order to get a round shape while being able to convert the mask file into the EBL file format (V30) [20]. Since PhC waveguides are quite lossy, they are usually defined to be maximum a few tens of micrometers long. To facilitate the cleaving of samples and to ensure a good optical coupling to the PhC structures, ridge waveguides 2 mm long are defined on each side of the PhC waveguides (see Fig.4.2). The ridge waveguides are tapered from 4 μm to $\sim$700 nm to improve the mode matching between the ridge waveguide and the PhC waveguide. These ridge waveguides are designed as two trenches separated from each other by the size of the desired ridge waveguide as illustrated in Fig.4.2. The mask is finally exported in a GDSII file format.

The design GDSII file is then passed on to the software PROXECCO[4], in order to prevent proximity effects during the writing of the design. Proximity effects are due to electron scattering in the resist and the substrate, resulting in a non uniform exposition of the design, i.e. the isolated features are under-exposed, whereas the dense features are over-exposed. The PROXECCO software calculates the distribution of the exposition required to compensate for proximity effects. If no correction is applied, the hole diameter can vary by $20-30\%$ along a waveguide, which has drastic consequences on the performance and properties of the PhC structures. More information on proximity correction can be found in [20,50,51]. The GDSII file can finally be converted to the EBL file format (V30) using the software JBXFILER available at DANCHIP facilities.

The pattern is written in the resist by exposing it to a focused electron beam. The system used is a JEOL JBX-9300FS Electron Beam Lithography System [52]. The thermal field emission gun (ZrO/W TFEG) source emitter can be accelerated from 50 kV up to 100 kV. A complex lens system focuses the beam on the sample, which gives a resolution below 20 nm. At an acceleration voltage of 50 kV (100 kV) the maximum writing field

[3] http://www.tanner.com/
[4] http://www.aiss.de/PROXECCO/PROXECCO.html

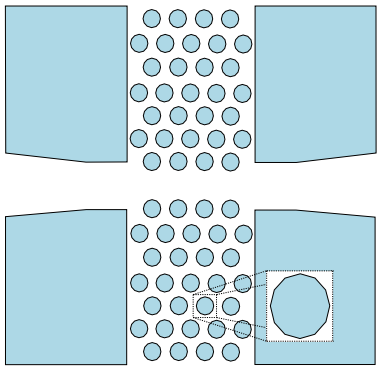

Figure 4.2: Example of a design file of a PhC waveguide where the filled zones correspond to the exposed zones. The holes are defined as dodecagons.

is 1000 μm$\times$1000 μm (500 μm$\times$500 μm) and the maximum scan speed is 25 MHz. The positioning of the sample is controlled by an interferometric system with a resolution below 1 nm. Several parameters have to be taken into account when writing the PhC pattern, notably the smallest feature size of the structure. It has been shown that a dose of 200 μC/cm^2 and a current of 0.2 nA for a step size of 4 nm were good parameters in order to write proximity corrected structures [20]. For more information on EBL the reader is referred to [53, 54].

4.2 Dry etching

To transfer the pattern from the resist to the top silicon layer, a dry etching technique is used, either conventional RIE [55] or inductively coupled plasma etching (ICP) [56]. Both techniques were used in order to fabricate the structures presented in this thesis. In both cases, the resist acts as a mask to the etch process and the pattern is transferred to the top silicon layer of the SOI wafer by a SF_6-based reactive ion etch. The dissociation of SF_6 in the plasma into atomic fluorine and heavy SF_5^+ allows the absorption of fluorine on the substrate surface where it reacts with the Si atoms to form volatile compounds (SiF_4) that desorb and are pumped away [57]. The overall reaction is the following:

$$SF_6 + e^- \rightarrow SF_5^+ + F + 2e^- \quad (4.1)$$
$$Si(s) + 4F(g) \rightarrow SiF_4(g) \quad (4.2)$$
$$(4.3)$$

where (s) and (g) stand respectively for solid and gas phases. An inherent electrical potential between the plasma and the substrate results in a bombardment of the substrate surface by the ions in the plasma, sputtering away the reaction products at the surface and thus enhancing the etch rate. The etch is made more preferentially vertical, or in other words more anisotropic, by adding carbon-fluorides or oxygen, which forms protective films on the substrate surfaces. The vertical/horizontal etch rate ratio (or anisotropy of the etch) is then increased since the directionality of the ions bombardment is even more important in removing these films. Since the etching rate of SiO_2 is really slow, the oxide layer of the SOI wafer acts as a etch stop. One must be careful when over etching the top silicon layer since it leads to line-broadening of the hole diameter, i.e. the vertical etch is slowed down, which may result in an increase of the horizontal etch.

In earlier experiments conventional RIE was used to transfer the pattern in the top silicon layer of the SOI wafer. In this configuration, the RF electric field is applied between two parallel plates, where the positive one is placed under the sample to be bombarded. The available system at DANCHIP is manufactured by Surface Technology Systems (STS). However, it was found, after a thorough investigation, that the etching conditons were suffering significant day-to-day variations. Moreover a large line-broadening of the pattern was obtained, which is unacceptable when fabricating fine-detailed structures like topology-optimised ones. More information on the recipe used for the silicon etch using RIE can be found in [20].

Because of the low efficiency of the conventional method of RIE another system, STS Advanced Silicon Etch (ASE), was used to transfer fine detailed structures to the top silicon layer. This is an ICP system where the RF electric field is provided by a coil surrounding the plasma chamber. This configuration gives a higher plasma density, which results in a $5-10$ times higher etching rate than in traditional RIE systems. In addition, the pressure can be kept low in the chamber, reducing the ion scattering in the plasma and thus maintaining the directionality of the ion bombardment [56]. Moreover, the ASE system offers the possibility

of using the Bosch process method, where the etching process is divided into sequential etching (SF_6 and O_2 gases) and passivation (C_4F_8) steps. During the passivation step, CF_2 is formed from C_4F_8:

$$C_4F_8 + e^- \rightarrow C_3F_6 + CF_2 + e^- \tag{4.4}$$

which is absorbed at the surfaces and forms a teflon-like polymer:

$$nCF_2 + * \rightarrow (CF_2)_n. \tag{4.5}$$

Due to the directionality of the ion bombardment of the substrate, the polymer layer formed on the surfaces is removed faster on the horizontal surfaces and the sidewalls remain protected during the etching phase. In this way, a high degree of anisotropy can be achieved.

The recipe used in the fabrication of the structures presented in this thesis insures a high anisotropy, which gives a high fidelity of the transfer of the pattern to the silicon top layer of the SOI wafer. Line-broadening below 40 nm, which may be due to over-etching the top silicon layer, was obtained. Moreover, the structures show nice and steep sidewall profile (see Fig.4.3), which is critical for the performance of PhC devices [58, 59].

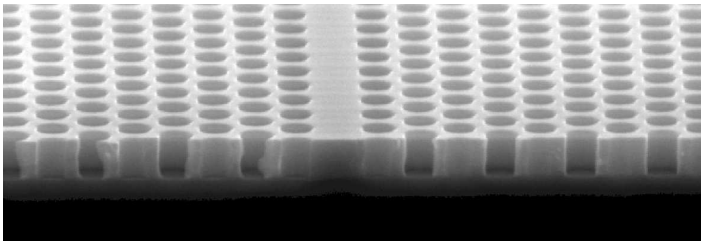

Figure 4.3: SEM micrographs of a 2D photonic crystal seen from the side (from [20]). The etch was done using the ASE system.

4.3 Summary

The fabrication process for photonic crystal components was presented in this chapter. Electron beam lithography and reactive ion etching are the two key techniques used respectively to write the pattern in a resist on top of the substrate and transfer this pattern in the top silicon layer of the substrate. In order to obtain high fidelity of the components, several considerations have to be taken into account, such as the design of the

holes, the proximity effect, and the writing parameters. Overall, the process established at DANCHIP facilities allows the successful fabrication of photonic crystal components with high fidelity and steep sidewall profiles.

CHAPTER 5

Characterisation of 2D photonic crystal components

Once fabricated, the photonic crystal components must be characterised in order to verify if their characteristics and performance fulfill expectations. Two techniques were used to characterise components in this thesis. First scanning electron microscopy (SEM) was utilised to gain physical information on the components, such as the diameter and the shape of the holes and the lattice constant. The second technique involves measuring the optical performances of the components. Both techniques will be described in the following sections.

5.1 Scanning electron microscopy

Scanning electron microscopy is an important characterisation technique in the process of fabrication of PhC components. It can be and was employed in order to verify the structures after different preparation steps, such as the development of the pattern in the resist or after the transfer of the pattern in the silicon top layer (see Fig. 5.2 for an example of a SEM image of a 2D PhC waveguide). In the first case, the SEM inspection allows the verification of the pattern written by electron beam lithography, to check that it corresponds to the wanted one. The diameter and

the shape of the holes are the important parameters to look at. A SEM inspection is always done at the end of the fabrication process to get the final diameter, shape of the holes and lattice constant. These parameters are important if one wants to simulate the structure using the techniques discussed in sections 3.1-3.2 and compare the simulation results with experimental results.

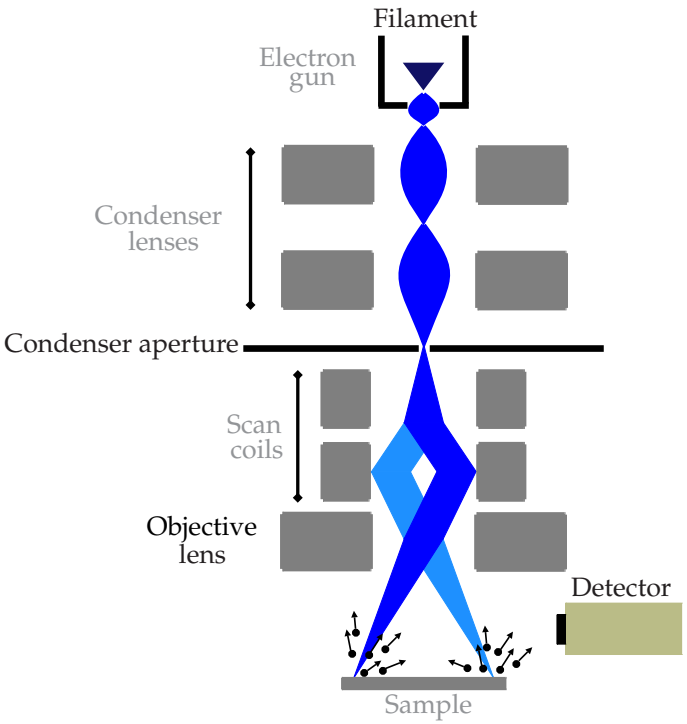

Figure 5.1: Schematic diagram of a scanning electron microscope.

Scanning electron microscopy is a part of the family of electron microscopy techniques. It allows high resolution images of a sample surface to be obtained. A sketch of a scanning electron microscope (SEM) is found in Fig.5.1. One of the most important parts of such a microscope is the electron column, which consists of an electron gun and two or more electron lenses, all kept under high vacuum. The electrons generated by the gun are accelerated to an energy in the range $0.1-30$ keV and focused by the electron lenses on the sample. The beam focused on the sample typically has a size of 10 nm and interacts with the sample to a depth of ~ 1 μm. Another important part of the microscope is the deflection

system, which allows the beam to scan the surface of the sample. It consists of two pairs of electromagnetic deflections coils (or scan coils) that sweep the beam across the sample. When the beam of electrons enters the sample, two types of scattering can occur: elastic scattering, leading to back-scattering electrons (BSE), and inelastic scattering, leading to secondary electrons (SE). These two types of signals carry information such as the sample composition, the shape of the sample and the local fine-scale surface texture. In the present case, SEM was used to visualise the topography of the sample. This is possible with SEM since the signals (BSE and SE) depend on the local inclination of the sample relative to the direction of the beam. The signals are recorded with a detector and converted into point-by-point intensity changes by the electronics. An image of the sample under investigation can then be constructed. More information concerning scanning electron microscopy can be found in [60].

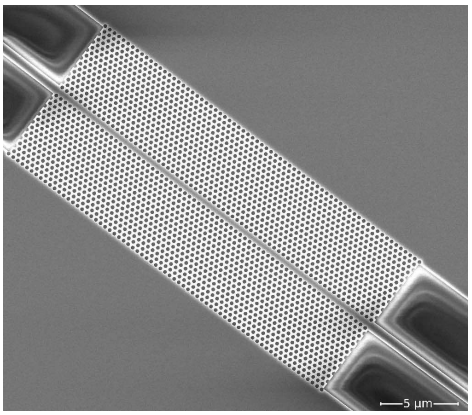

Figure 5.2: SEM picture of a straight 2D photonic crystal waveguide.

5.2 Optical transmission setup

The setup used to measure the amplitude response of the components is shown in Fig. 5.3. The light source can either be a broadband light emitting diode (LED) or a tunable laser (TL), depending on the properties of the components under investigation. The LED is mainly used to obtain a broadband characterisation of the components, whereas the TL is utilised to resolve fine details in the optical response of a component. As the behavior of PhC components is highly polarisation dependent, some ad-

justment of the polarisation of the light coming out of the source and injected in the components is required. First a polarisation controller helps to rotate the polarisation of the light coming out of the source, so that it is aligned with the axis of the polariser. The high extinction ratio of the polariser ($>$ 35 dB) ensures a precise selection of the polarisation. The polarised light is then rotated with a second polarisation controller in order to match the polarisation axis of the waveguide under investigation. Tapered lensed fibers enable the coupling to the device under test (DUT). The transmitted signal is collected via another tapered lensed fiber and is finally measured with a optical spectrum analyser (OSA) as a function of wavelength.

The sample is held in place by a vacuum chuck on a translational stage placed under a microscope. This allows for visual inspection and also for coarse alignment of the tapered lensed fibers at each end of the waveguide to be measured. The fibers are mounted on three-dimensional translation stages equipped with piezo-resistive elements ensuring accurate positioning and thus a maximum in- and out-coupling to the waveguide. To align the fibers, their position is adjusted until the transmission through the sample is maximised.

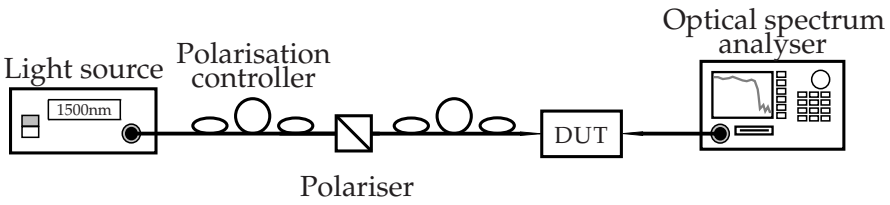

Figure 5.3: Setup for characterisation of photonic crystal components.

To facilitate the coupling of light between the tapered lensed fibers and the photonic crystal waveguide, tapered ridge waveguides are included in the design. The width of the ridge waveguide is gradually changed from 4 μm to $\sim$700 nm to improve the mode matching between the ridge waveguide and the photonic crystal waveguide.

For most of the measurements presented in this thesis, TE polarisation was selected as the components were mainly designed for this polarisation. To select the proper polarisation, the fibers are first aligned with respect to a ridge waveguide[1]. Due to its asymmetric shape ($\sim$ 300 nm$\times$4 μm), the ridge waveguide preferentially guides TE polarisa-

[1] A ridge waveguide is always included in the design for normalisation purposes.

tion. By maximising the transmission through the ridge waveguide with the help of the polarisation controller, a coarse selection of the TE polarisation can be done. Fine tuning is achieved by coupling to a PhC component and maximising the pronounced drop in transmission at the cutoff of the fundamental PBG mode, by adjusting the second polarisation controller. In order to select TM polarisation, the polariser needs to be rotated by 90° after the optimisation for TE polarisation has been done.

5.3 Summary

The two main characterisation techniques used for PhC components were presented in this chapter. The principle of a scanning electron microscope was introduced. The diameter and the shape of the holes and the lattice constant are the important parameters to extract from SEM images of PhC components. This information helps the modelling of structures in order to compare the simulation results with the experimental ones. The other technique consists of an optical transmission setup, which enables the measurement of the transmission spectrum of a PhC component. The two methods described in this chapter made it possible to obtain the experimental results presented in chapter 6.

CHAPTER 6

Experimental results for 2D photonic crystals waveguide-based components

This chapter will present the different experimental results related to photonic crystal components obtained during this project. The first section will deal with the propagation of TM-polarised light in photonic crystal waveguide-based components, topology-optimised for the TE polarisation. This will be followed by details of the optimisation of photonic crystal waveguide-based components for the slow-light regime. Both in- and out- coupling and 60° bends have been improved for the slow-light regime using the topology optimisation method.

6.1 Propagation of TM-polarised light in photonic crystals waveguide-based components optimised for the TE polarisation

As introduced earlier in this thesis, the topology optimisation method has been used to improve the TE-polarised light propagation performance of photonic crystal waveguide components. Although there is no nearby band gap for TM polarisation (Fig. 3.4), the propagation of TM-polarised

light in photonic crystal waveguide-based components, originally optimised for the TE polarisation, has been investigated. The experimental and numerical study of the propagation of TM-polarised light in topology-optimised 60° and 90° bends and a Y-splitter will be presented.

The components have been fabricated using e-beam lithography and standard anisotropic reactive-ion etching to define the photonic crystal structure into the 300 nm top silicon layer of a SOI wafer. The photonic crystal structure has a lattice constant of $a = 400$ nm in a triangular configuration of air holes of radius $r \approx 145$ nm. This arrangement gives rise to a large band gap below the silica line for TE-polarised light. The waveguides were obtained by removing a single row of holes in the Γ-K direction of the lattice. Figure 6.1 shows the SEM micrographs of the resulting optimised structures for a 60° bend [40], a 90° bend [41], a Z bend [15], and a Y-splitter [42]. More information on the optimisation of each structure can be found in the respective reference.

Characterisation of the waveguides was carried out with the setup illustrated in Fig. 5.3 with a light emitting diode where the TM-polarised light was selected via the polariser and the polarisation controllers. The choice of light source was motivated by the investigations of the broadband characteristics of the components.

The two 60° bends (Fig. 6.1 (a)) are separated by a straight $7a$ long photonic crystal waveguide with identical ridge waveguides for in- and out- coupling. The topology optimisation method has been applied to the bend region including the inner and outer parts. Figure 6.2 shows the loss per bend for this component for TM-polarised light. The transmission spectrum is normalised to a straight photonic crystal waveguide of similar length as the device, with identical ridge waveguide coupling structures. The Fig. 6.2 also shows the performance of an un-optimised 60° bend with ordinary holes in the bend region. Both the experimental results (plain curves) and the 3D FDTD (dashed curves) results are shown for the two configurations. The optimised component has an average loss per bend of 0.4 ± 0.3 dB in the range $1400-1650$ nm for TM-polarised light. A slight shift of 1% in absolute wavelength was applied to the 3D FDTD spectrum to better fit the experimental data. Apart from this, the simulation curves are in agreement with the measured spectra. The topology optimisation method reduced the propagation loss of TM-polarised light by ~ 7 dB per bend for this 60° bend device. Thus, the optimisation technique improves the transmission through the 60° bend for TM as well as TE polarisation as seen previously in [40].

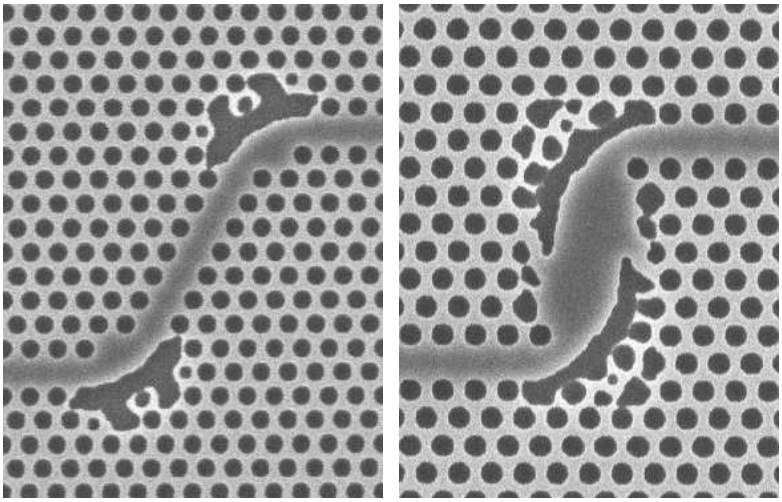

(a) 60° bend (b) 90° bend

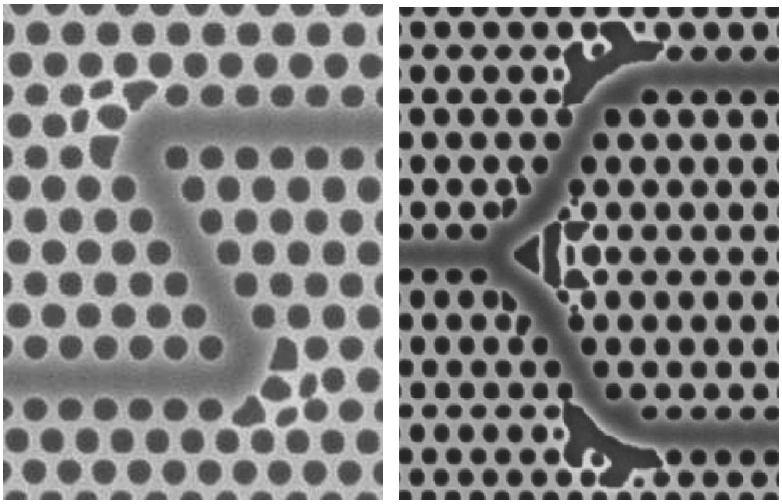

(c) Z bend (d) Y-splitter

Figure 6.1: SEM micrographs of topology-optimised components for TE-polarised light: (a) 60° bend, (b) 90° bend, (c) Z bend, and (d) Y-splitter. For all structures, the lattice constant is $a = 400$ nm.

In the same way, Fig. 6.3 shows the loss per bend for an optimised and un-optimised 90° bend for TM-polarised light. As depicted in Fig. 6.1 (b), the two 90° bends are separated by seven rows with two or three missing holes. The topology optimisation has been applied to a predefined do-

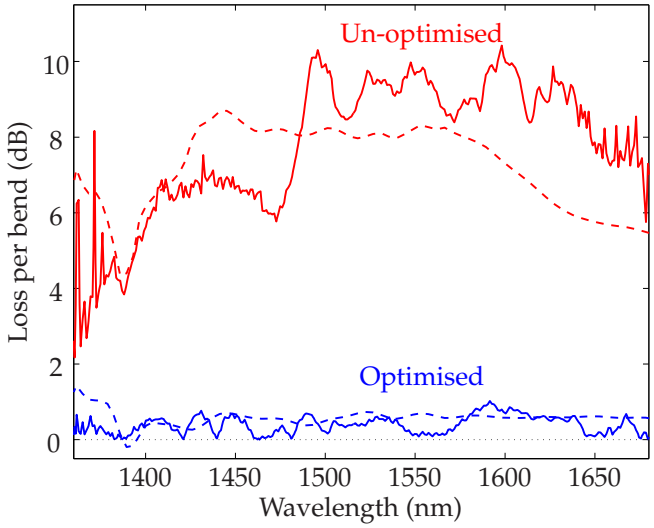

Figure 6.2: Loss per bend (dB) for an optimised (blue) and un-optimised (red) 60° for TM-polarised light (plain curves: experimental results, dashed curves: 3D FDTD simulations).

main as explained in detail in [41]. Again, the optimisation technique was done for TE-polarised light and also improved significantly the performance for TM-polarised light, reducing the loss per bend by ~ 7 dB and keeping it on average below 1 dB over the 250 nm range (0.9 ± 0.3 dB).

Another important component investigated is a Y-splitter. It consists of a Y-junction and two 60° bends, as shown in Fig. 6.1 (d). Figure 6.4 shows the normalised measured transmission of TM-polarised light for the two output ports of the Y-splitter (plain curves). The 3D FDTD results (TM polarisation) are also shown for the two outports of the splitter (dashed curves). The difference between the two simulated curves is probably due to a rough discretisation of the structure leading to an asymmetry in the simulated structure. Even though the component was initially optimised for TE-polarised light [42], it exhibits a bandwidth of 180 nm with an average excess loss of only 1.6 ± 0.5 dB for TM polarisation.

The propagation of TM-polarised light in 2D PhC components has been reported previously. In Ref. [61] un-optimised straight and bent waveguides were investigated with TM polarisation. A broad low-loss transmission window in the range 1500−2000 nm predicted by theory has been confirmed experimentally. Propagation loss as low as $2.5 \pm$

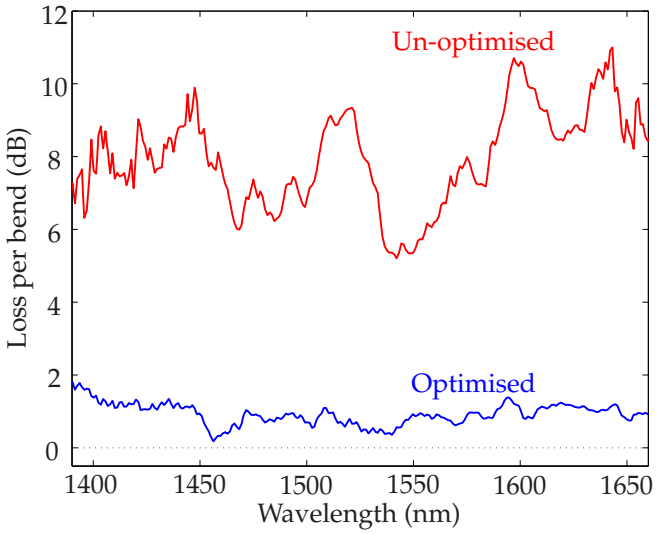

Figure 6.3: Loss per bend (dB) for an optimised (blue) and un-optimised (red) 90° bend for TM-polarised light.

4 dB/mm around 1525 nm has been measured. The region of low loss for TM-like modes is dominated by index-guiding. Moreover, it overlaps one of the TE PBG modes. Since the components were topology optimised for a large bandwidth that exceeds the bandwidth of the TE photonic band gap, the obtained structures favours the index-guiding properties. It would explain why TM-polarised light can be well guided in the 60° bend, the Y-splitter, and the 90° bend making them suitable for both polarisations.

On the other hand, for the Z bend component shown in Fig. 6.1(c), the topology optimisation method improved the performance of TE-polarised light [15] much more than for TM-polarised light. The optimisation method has been applied to the outer part of the two bends. Figure 6.5 shows the loss per bend for this component. The optimised component is compared to an un-optimised Z bend, that is two consecutive 120° bends with ordinary holes. The improvement introduced by the optimisation method is about 2 dB, which is much less than for the previous components. The Z bend is probing the PBG effect with strong reflection due to the 120° bend whereas the 60° and 90° bends and the Y-splitter have a more index-guiding-like behaviour. The guiding in the optimal 120° bend is dominated by band gap effects and, therefore, it does not work

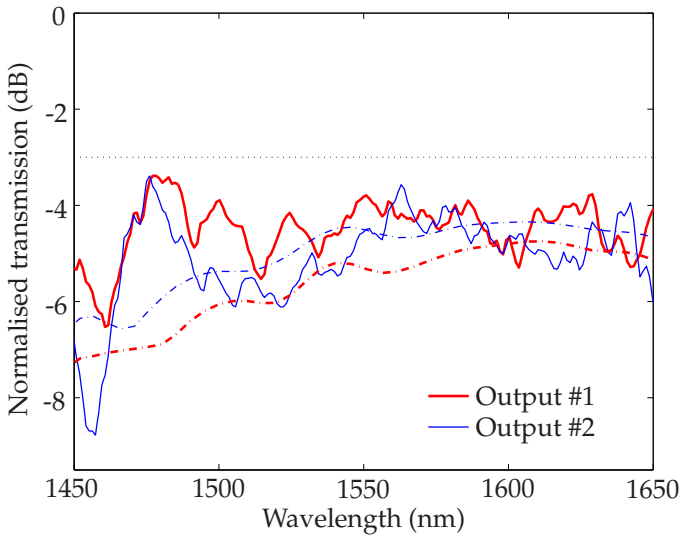

Figure 6.4: Normalised transmission (dB) for TM-polarised light for the two outports of a topology-optimised Y-splitter (plain curves: experiments, dashed curves: 3D FDTD simulations).

as well for TM-polarised light.

In conclusion, it was shown that it is possible to obtain photonic crystal waveguide components which work for both TE and TM polarisations using the topology optimisation method. This method reduced loss by rearranging the material in some definite regions of the different components bringing losses, for TM-polarised light, to 0.4 ± 0.3 dB per bend for the 60° bend, to 0.8 ± 0.3 dB per bend for the 90° bend, and to 1.6 ± 0.5 dB for the Y-splitter, over a bandwidth of more than 150 nm. This technique is increasing the performance of the index-guiding region for the TE-polarised light, and thus also for TM-polarised light. Interestingly, the topology optimised parts of the structures resemble ridge waveguide structures, as intuitively might have been expected, since it has been demonstrated previously that straight and sharply bent single-mode ridge waveguides can display very low losses [5]. Hence, the result demonstrates the reliability of the topology optimisation method because it gives, in these cases, simple and intuitive optimised designs. On the other hand, in the case of the sharp Z bend TM- and TE-polarised light does not give similar results as this structure is probing deeper into the photonic crystal area due to its shape. In most cases the topology opti-

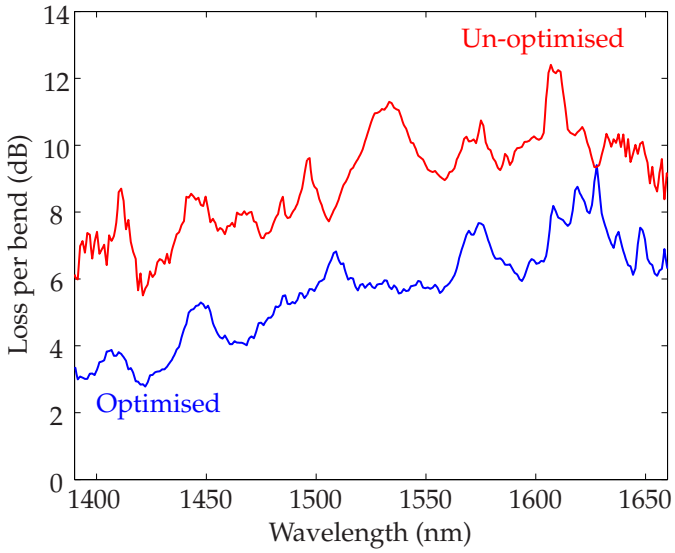

Figure 6.5: Loss per bend (dB) for an optimised (plain curve) and un-optimised (dashed curve) Z bend for TM-polarised light.

misation method removed the periodicity and proposed index-guiding structures. Even when the photonic crystal structures are optimised, the photonic wires (small dimension ridge waveguides) are an order of magnitude or more better in terms of loss. The topology optimisation method confirmed that the periodic arrangement of circular air holes in the bending and splitting regions of the component is not the preferred solution to guide the light over a broadband range.

6.2 Topology optimisation of the slow-light regime

Presently, there is a strong shift towards design and deployment of photonic crystal structures for all-optical integral circuits. One area of considerable interest is the slow-light regime due to the enhancement of light-matter interactions; group velocities 200-300 times lower than the propagation speed in vacuum have been reported recently in direct interferometric [7] and time-of-flight [17, 62] measurements. This feature has also been used for optical modulation [7, 63, 64], and there are proposals to build delay lines [65] and optical storage [28]. Slow-light modes exhibit extraordinary dispersion properties and typically experience very high losses due to coupling and also to propagation through non straight wa-

veguides. These two issues have been investigated and optimised using the topology optimisation method, which has been detailed previously. The results of the optimisation will be presented in the following sections.

6.2.1 Enhancement of coupling to the slow-light regime in photonic crystal waveguides using topology optimisation

As mentioned earlier, one of the most interesting properties of photonic crystal waveguides is the low group velocity that can be achieved. However, an efficient way of coupling light into the slow-light regime of the photonic crystal waveguide is required in order for this characteristic to be useful. The position of the coupling interface between the ridge waveguide and termination of the photonic crystal lattice is believed to be important for improving the mode matching [66–68]. Surface states localised at the interface of the photonic crystal could have a major influence on the coupling [69–71]. Recently, several configurations to improve the coupling to the slow-light in photonic crystal waveguides have been theoretically proposed [72, 73] and investigated experimentally [74–76]. Here, the topology optimisation method [15, 41] has been applied to enhance the in- and out-coupling to the slow-light mode in photonic crystal waveguides.

The components have been fabricated using e-beam lithography and inductively coupled plasma etching to define the photonic crystal structure into the $\sim$320 nm top silicon layer of a SOI wafer. The photonic crystal structure has a lattice constant of $a \approx 400$ nm in a triangular configuration of air holes of radius $r = 130$ nm. As shown previously, this arrangement gives rise to a photonic band gap for TE-polarised light (Fig 3.4). Waveguides were obtained by removing a single row of holes in the Γ-K direction of the lattice.

The topology optimisation method was utilised to improve the incoupling to the slow-light regime of a straight photonic crystal waveguide. A 1×12 unit lattice constant rectangle, as depicted on Fig 6.6(b), was chosen as the model domain in which the optimisation algorithm should redistribute the material. This choice is made to address the impedance matching between the two different types of waveguides. Figure 6.6 shows scanning electron micrographs of the un-optimised ((a), (b), and (c)) and optimised ((d), (e), and (f)) fabricated structures.

As shown in Fig. 6.6 (a)-(b)-(c), three different starting points for the optimisation were investigated. In Fig. 6.6 (a) there is a left shift of $a/7$ of the termination of the lattice, in Fig. 6.6 (b) the termination is exactly in

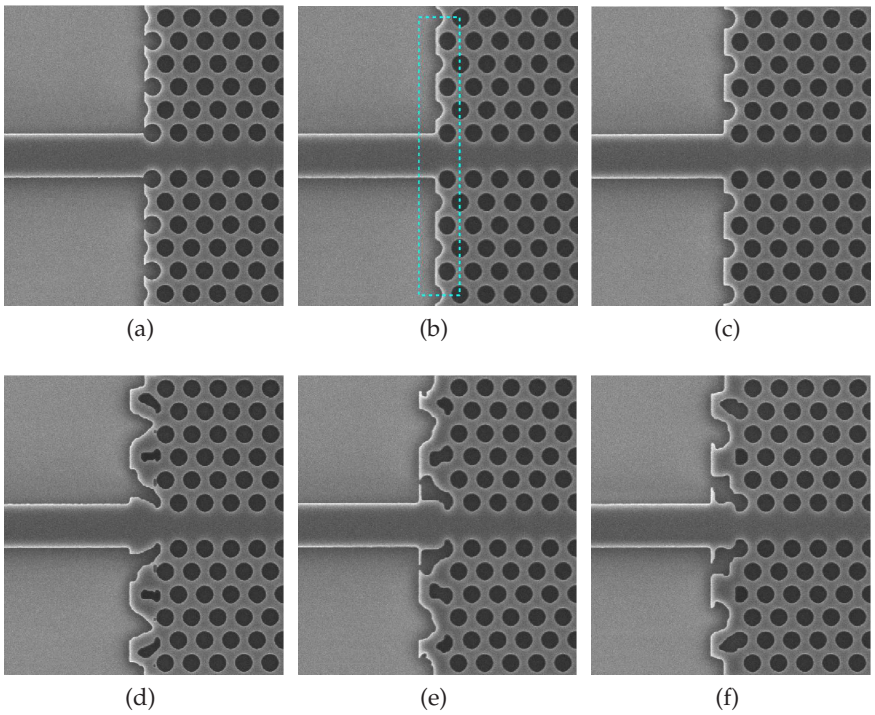

Figure 6.6: SEM micrographs of topology-optimised coupling components for the slow-light regime: Left shifted (a) un-optimised and (d) optimised structure, Middle (b) un-optimised and (e) optimised structure, and Right shifted (c) un-optimised and (f) optimised structure.

the middle of the first column of holes, and in Fig. 6.6 (c), there is a right shift of $a/7$ of the termination of the lattice. The results for the topology optimisation of Fig. 6.6 (a) is (d), Fig. 6.6 (b) is (e), and Fig. 6.6 (c) is (f). For each of the six structures the out-coupling regions are designed and fabricated identically to the in-coupling regions.

Figure 6.7 shows the transmission spectra for the six structures shown in Fig. 6.6. The photonic crystal waveguides are ~ 12 μm long. Figure 6.7 (a) corresponds to a left shift of $a/7$ of the termination of the lattice, Fig. 6.7 (b) corresponds to the termination being exactly in the middle of the first column of holes and Fig. 6.7 (c) corresponds to a right shift of $a/7$ of the termination of the lattice. In all cases, the spectrum for the optimised structure (red curve) is compared to the un-optimised one (blue curve). It is seen that for the three structures, the topology optimi-

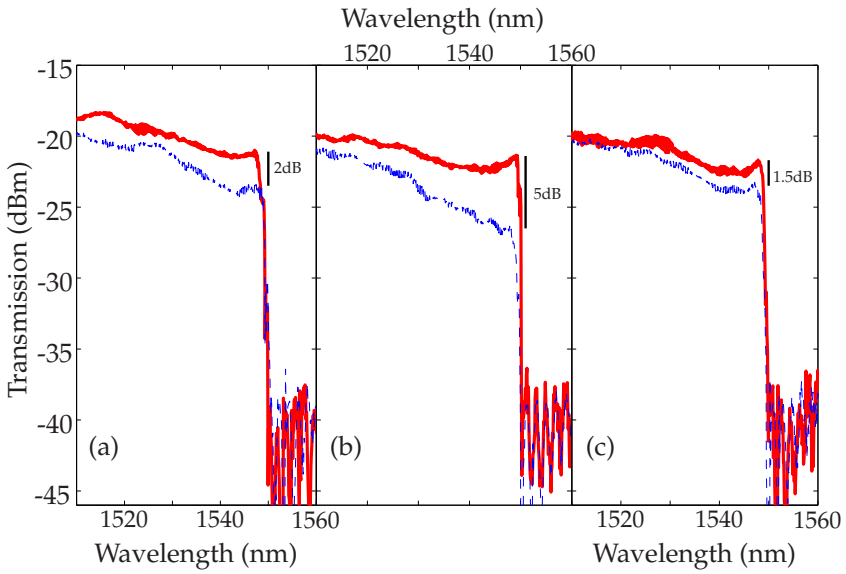

Figure 6.7: Measured transmission through coupling components for the slow-light regime: (a) Un-optimised (blue) and optimised (red) left shifted structure, (b) Un-optimised (blue) and optimised (red) middle structure, and (c) Un-optimised (blue) and optimised (red) right shifted structure.

sation method improves the overall transmission through the waveguides. Moreover, an enhancement in the combined in- and out-coupling of 1.5, 2, and 5 dB is observed in the slow-light regime just before the cut-off at $\sim$1550 nm for the left shifted, right shifted, and middle structure respectively. Futhermore, the middle structure presents unique high transmission in the last 1 nm before the cutoff.

In summary the topology optimisation method can be used to enhance the in- and out-coupling to the slow-light regime in photonic crystal waveguides resulting in compact structures. Three different starting point structures have been tested and for all of them, the optimisation procedure resulted in designs having nearly the same performance regardless of the initial configuration, showing once more the robustness of the optimisation technique.

6.2.2 Optimisation of 60° bends for the slow light regime

Effective bends in photonic crystal waveguides may be advantageous in all-optical integrated circuits, but the design of these has been a great challenge as a sharp bend constitutes a severe discontinuity in the photonic crystal lattice and introduces high losses. Different optimisation approaches for bends in waveguides formed by removing one row of holes have been shown in numerous papers [31, 37, 40, 77–87] providing acceptable bend losses in the so-called normal group velocity regime (section 3.3.3).

Some attempts have been made to improve the slow-light transmission in photonic crystal waveguides containing 60° bends [83, 88]. Design criteria were based on changing the effective dielectric constant directly in a region of the bend by shrinking the size of the radius of carefully selected holes. The linear dispersion regime is thereby extended to lower frequency (see Fig. 3.8). The idea works for the slow-light regime as reported both in theoretical predictions and experiments in this section, however at the cost of a decreased pass band window. This section presents broadband transmission for 60° bends optimised for the slow-light regime.

The design proposed by Moll *et al.* [83] has been modified using the mapping of the field introduced previously (Fig. 3.9), which unambiguously shows the importance of the design of the second nearest row of holes, and also the ideas by Moll and Bona [83], who state that the Bloch mode is dragged out into the outer corner of the bend. The inner corner of the bend was made smoother by removing the outermost hole, as shown in Fig 6.10(b). In the outer corner, the radius was decreased for selected holes both in the first and second rows. This configuration will be referred as the *naïve design*. The approach has been confirmed by 3D FDTD calculations as shown in Fig 6.8. The transmission spectrum for the resulting bend is much wider than those presented in references [83, 88] and higher in absolute transmission. However, in the very slow-light regime the transmission is slightly lower than Moll's design [83].

As a next step the topology optimisation method is employed to increase the bandwidth further. One optimisation scheme, called DESIGN 1, is based on optimising both the first and second nearest rows of holes (Fig 6.9(a)), while the other scheme, called DESIGN 2, optimises only in the region of the second row of holes (Fig 6.9(b)). The same range of frequencies within the slow-light regime was addressed for the optimisation of both structures.

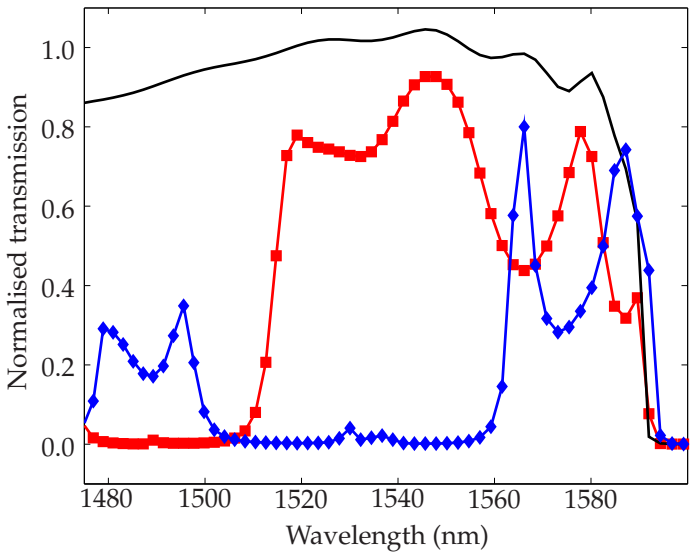

Figure 6.8: Transmission spectra for the different designs of the 60° bend obtained by 3D FDTD: straight photonic crystal waveguide (black line), Moll's design with 4 holes of radius $r \approx 0.24a$ (blue diamond line), and naïve design with $r \approx 0.24a$ (red square line).

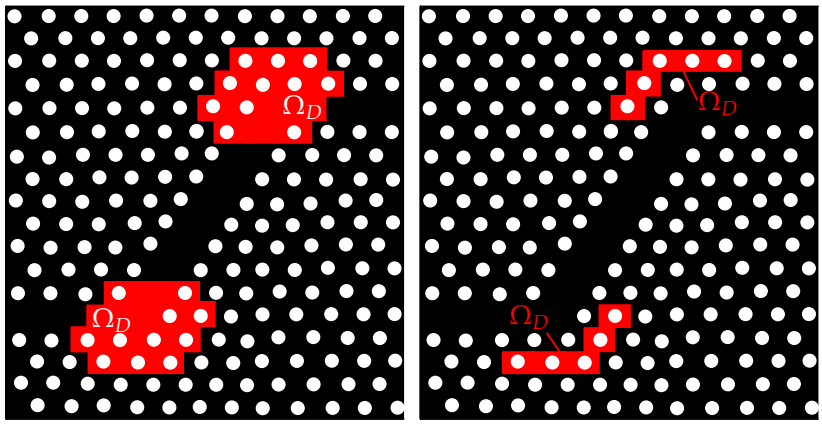

(a) (b)

Figure 6.9: Two different domains for the topology optimisation of 60° bends for the slow-light regime: (a) DESIGN 1, (b) DESIGN 2.

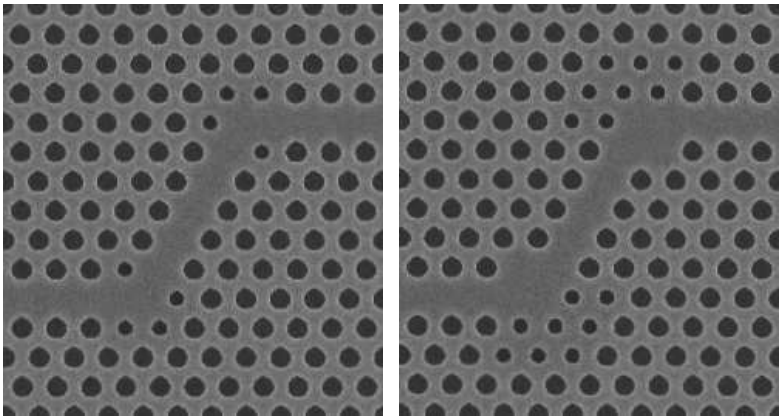

(a) Moll's design (b) Naïve design

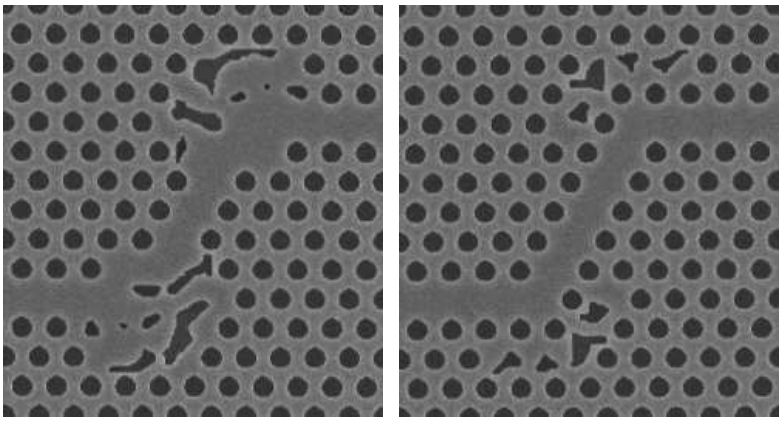

(c) DESIGN 1 (d) DESIGN 2

Figure 6.10: SEM micrographs of 60° bends: (a) Moll's design, (b) naïve design, (c) topology-optimised DESIGN 1, and (d) topology-optimised DESIGN 2. For all structures, the lattice constant is $a = 400$ nm.

The components were fabricated in the same way as described in section 6.2.1. Figure 6.10 shows the fabricated 60° bends. The smaller holes in Fig. 6.10 (a)-(b) have a radius of $r \approx 49$ nm. It is interesting to note that the topology optimisation method removed the corner hole on the inner side of the bend in DESIGN 1, supporting the design rules chosen for the naïve design.

Figure 6.11 presents the transmission through fabricated bends based on reference [83], the naïve design, topology-optimised DESIGN 1, and

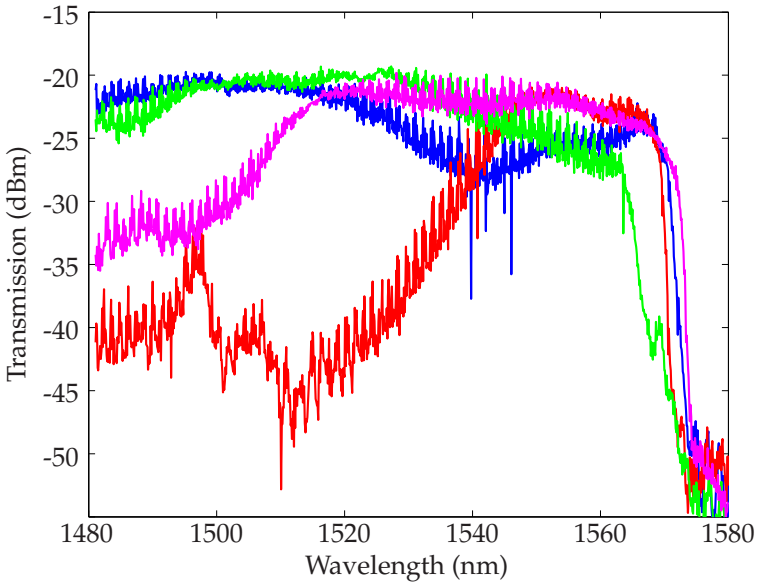

Figure 6.11: Measured transmission through fabricated bends of different designs: Moll's design (red), naïve design (green), topology-optimised in both rows regions (pink) and topology-optimised second row only (blue).

topology-optimised DESIGN 2 (see Fig. 6.10). The naïve design has a wide transmission bend compared to Moll's design, however with less transmission close to the cutoff in the slow light regime, as predicted by 3D FDTD calculations. Moreover, the two row topology-optimised bend improved the slow light regime. The lower transmission for wavelengths below 1510 nm could be attributed to design parts lying in the waveguide, hindering the propagation of the linear dispersion regime. By changing only the second row of holes (Fig. 6.11 blue curve), an enhancement of the transmission in the slow light regime together with broadband transmission can be achieved. This confirms the importance of the second row of holes at the bend for the propagation in the slow-light regime, which in turn does not affect the linear regime [89].

Numerical and experimental results showing consecutive improvements of the slow-light transmission through a photonic crystal waveguide 60° bend have been presented. A wide transmission window in the linear regime was maintained with the help of naïve design ideas based on changing the effective index locally in the bend regions, and taking

the field distribution in the slow-light regime into account. Further improvements of slow-light transmission have been made by applying the topology optimisation method. Good correlation between modeled and measured results has been found.

6.3 Summary

During this project photonic crystal waveguide-based components fabricated using electron beam lithography have been optimised and characterised. It was shown that it is possible to obtain photonic crystal waveguide components working for both TE and TM polarisations using the topology optimisation method. The principle behind this technique is to rearrange the material in some definite regions of different components in order to reduce losses. Given the optimisation parameters used, the technique increased the performance of the index-guiding region for the TE-polarised light, thus also for TM-polarised light. In most cases, the topology optimisation method removed the periodicity and proposed index-guiding structures, which have been shown to be an order of magnitude or more better in terms of loss [5]. The topology optimisation method confirmed that the periodic arrangement of circular air holes in the bending and splitting regions of the component is not the preferred solution to guide the light over a broadband range.

The topology optimisation method was futhermore used to improve the performance of photonic crystal waveguide-based components for the slow-light regime, which is a more promising characteristic of photonic crystal components. It was first used to enhance the in- and outcoupling to the slow-light regime in photonic crystal waveguides from 1.5 dB up to 5 dB. The robustness of the technique was established futher by obtaining a similar structure showing nearly the same performance regardless of the initial configuration to be optimised.

Improvements to the slow-light transmission through photonic crystal waveguide 60° bends were finally presented. It was shown that it is possible to improve the performances of the bends in the slow-light regime, while keeping a wide transmission window in the linear regime. Both intuitive design based on the mapping of the field in the slow-light regime and topology optimisation were successfully applied to change the structure in the bend area. The results have been confirmed theorically and experimentally.

CHAPTER 7

Conclusion

The 2D photonic crystal is an interesting platform to develop specific integrated optical devices. In order to learn more on this subject the fundamentals of photonic crystal waveguides have been introduced including a way to fabricate and characterise these devices. Moreover, an optimisation technique called topology optimisation has been briefly described. Applied to photonic crystal waveguides, it consists of a redistribution of the material in order to maximise the desired property of the given component for a given range of frequencies. Photonic crystal components optimised for TE polarisation with this technique were investigated for TM-polarised light. The optimisation method gives structures that resemble ridge waveguides leading to an index-guiding-like behaviour, which explains the improved performance of the devices for both polarisations. These results seam to indicate that photonic crystal waveguides are not the ideal choice to simply guide light. On the other hand, the remarkable dispersion seen in these components has attracted much interest in the field. In order to use this feature, the topology optimisation method was employed to reduce the propagation loss through photonic crystal 60° bends waveguides and also to improve the coupling to the slow light mode in straight photonic crystal waveguides. In both cases noticeable improvement was achieved giving more opportunities to use slow-light in photonic crystal waveguides.

PART II

Preparation and characterisation of InSb nanocrystals embedded in SiO_2

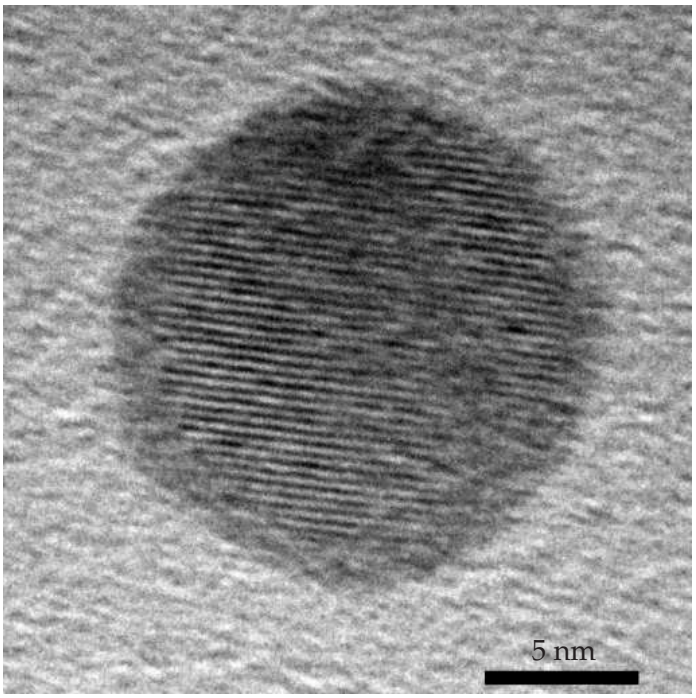

CHAPTER 8

Introduction to InSb nanocrystals

Light emitting nanocrystals have attracted the attention of many research groups around the world because of their potential applications. The possibility of tuning their absorption and photoluminescence spectra over a very wide range of energy, by varying the crystal size, gives the opportunity of fabricating nanocrystal-based light sources (Fig. 8.1). Certainly one of the most prominent potentials of nanocrystals is to turn silicon into an optically active material. Due to its indirect band gap, bulk silicon is a bad candidate for light emission. However, silicon nanocrystals have proven to be efficient light emitters [2, 9, 90]. Moreover, nanocrystals of direct- and indirect-band gap semiconductors can be embedded in a SiO_2 matrix, which is compatible with CMOS fabrication technology developed for microelectronics.

In order to obtain an integrated light source in silicon which can be coupled to waveguide components, the light emission must lie in the transparency window of silicon (>1.1 μm) to avoid absorption. Silicon nanocrystals are a bad choice for this purpose since the emission is between 700 and 1000 nm. Fujii *et al.* recently reported that the presence of silicon nanocrystals in Er-doped SiO_2 considerably enhances the effective erbium absorption cross section leading to an enhancement of the photoluminescence at 1.54 μm [91]. Even though this configuration is very promising, the efficiency of the light emission must still be improved by

an order of magnitude to reach the level of industrial production. Another approach is to have efficient light emission in the right wavelength range from nanocrystals of another semiconductor material in SiO_2. InSb and InAs are semiconductors with small band gaps displaying a large electron-hole pair Bohr radius. In the form of nanocrystals, they hold the possibility of tuning the band gap over a large range of wavelengths (Fig. 8.1), and possibly in the wavelength range of interest for silicon photonics.

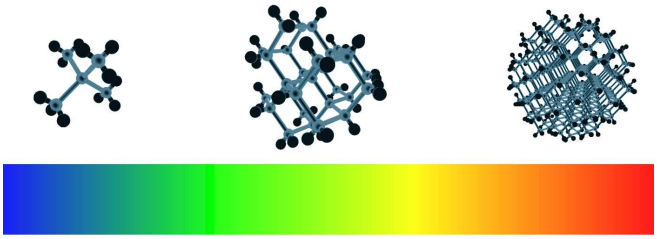

Figure 8.1: Illustration of the effect of the size of nanocrystals on their emission spectrum [92].

In the present work attention was focused on InSb because of its large potential tunability. Several attempts have been made to synthesize this material on the nanoscale, most of them on a III-V platform, and recent experiments with InSb-based quantum dots have seen photoluminescence at room temperature in the mid-infrared [93]. There have only been two studies of the formation of InSb nanocrystals in SiO_2 [94, 95]. While one reported quantum confinement effect via absorption measurements [94], the other did not report any size dependency features [95].

This part of the thesis details the work done on the formation of InSb nanocrystals in SiO_2 and their characterisation. First, the concept of quantum confinement will be introduced and applied to the case of InSb nanocrystals. The theoretical and experimental results from the literature on InSb nanostructure will also be summarised. It will be followed by the description of the method used for the synthesis of InSb nanocrystals in SiO_2. The main charaterisation techniques used in this project will be presented in detail. Finally, the results obtained for the formation of the InSb nanocrystals in SiO_2 will be discussed. This includes a study of the important parameters required in order to obtain the nanocrystals, but also the experimental and theoretical results for the melting and solidification of InSb nanocrystals embedded in SiO_2 showing both superheating and undercooling.

CHAPTER 9

InSb nanocrystals and their properties

Nanocrystals of semiconductors are often referred to as artificial atoms because their electronic structure resembles those of atoms. Several interesting physical properties arise from scaling down the size of crystals to the nanometer scale. The tunability of their absorption and emission of light over a very wide range of energy by varying the crystal size is probably their most interesting feature.

The semiconductor of interest in the present work is InSb. InSb nanocrystals are believed to be a good candidate for IR emission because of the low band gap energy of the bulk material ($E_g = 0.17$ eV at 300 K) and its large electron-hole pair Bohr radius. Thus, by synthesizing InSb nanocrystals in SiO_2 an attractive silicon compatible light source can be achieved.

This chapter will first explain briefly the quantum confinement effect expected and observed in semiconductor nanocrystals. This will be followed by a discussion on InSb nanocrystals from results found in the literature, which motivated the present work.

9.1 Quantum confinement in nanocrystals

The energy shift introduced by scaling the size of nanocrystals or quantum dots is due to the effect called *quantum confinement*. This effect can be understood by looking at the problem of a "particle in a box" known from quantum mechanics. In this problem, a particle experiences no force inside the box or well and is constrained inside it since its sides are at an infinite potential (Fig 9.1(a)). The solutions of this problem are obtained by solving the Schrödinger equation and give a quantization of the energy, i.e. there are discrete energy levels allowed for the particle, which for the 1D problem are:

$$E_n = \frac{\hbar^2 \pi^2}{2mL^2} n^2, \quad n = 1, 2, 3, ... \tag{9.1}$$

where $\hbar$ is Planck's constant, m is the mass of the particle, and L is the width of the well. Figure 9.1(b) illustrates the two first eigenfunctions of the particle corresponding to the two first energy levels ($n = 1$ and $n = 2$). It is important to notice that the lowest energy level ($n = 1$) of the particle is non zero. Futhermore, this level increases by decreasing the width of the well (L) as seen with Eq. 9.1. The quantum confinement effect can thus be summarized as giving rise to a quantization of the energy levels, which can be scaled in this case by changing the width of the well.

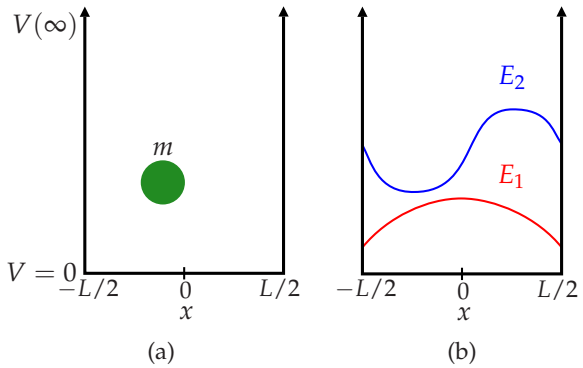

Figure 9.1: (a) A particle of mass m confined in an infinite potential well of width L. (b) The two first eigenfunctions of a particle in an infinite potential well.

In the case of nanocrystals, there is confinement of particles (elec-

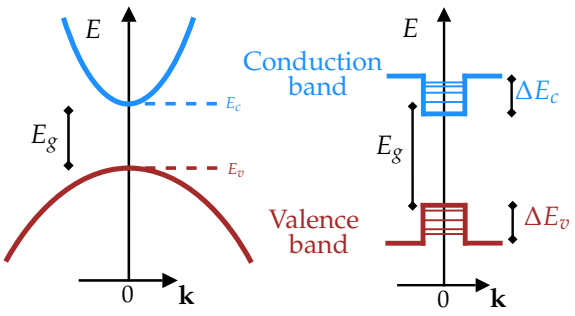

(a) Bulk (b) Nanocrystal

Figure 9.2: (a) Band diagram illustration for a direct semiconductor. (b) Band diagram illustration for a semiconductor nanocrystal.

trons, holes, phonons) in all three dimensions. In the present case, the system of interest is InSb nanocrystals embedded in a medium which has a higher band gap energy, namely SiO_2 (∼9 eV). InSb is a direct band gap semiconductor and its band diagram is schematized in Fig. 9.2(a), where $E_g = 0.17$ eV at 300 K [96]. As will be shown later (chapter 12), the nanocrystals of InSb embedded in SiO_2 are spherical. A simple model [97] is to consider that the nanocrystal of radius R has a barrier at the conduction band (ΔE_c), which can be seen as a square well potential of height ΔE_c for $r > R$ and 0 for $r < R$ (Fig. 9.2(b)). Assuming zero angular momentum, the Schrödinger equation for an electron can be separated into a radial and an angular part. The radial equation is given by:

$$-\frac{\hbar^2}{2m_e}\frac{\mathrm{d}^2\phi}{\mathrm{d}r^2} + \left(V(r) + \frac{l(l+1)\hbar^2}{2m_e r^2}\right)\phi = E\phi \tag{9.2}$$

where m_e is the effective mass of the electron, $V(r)$ is the potential and l is the angular quantum number. When $l = 0$, Eq. 9.2 reduces to:

$$-\frac{\hbar^2}{2m_e}\frac{\mathrm{d}^2\phi}{\mathrm{d}r^2} + \Delta E_c\phi = E\phi \quad r > R \tag{9.3}$$

$$-\frac{\hbar^2}{2m_e}\frac{\mathrm{d}^2\phi}{\mathrm{d}r^2} = E\phi \quad r < R. \tag{9.4}$$

The eigenvalues are then obtained by solving the transcendental equa-

tion:

$$\cot\left(\sqrt{\frac{2m_e\left(\Delta E_c - E\right)}{\hbar^2}}R\right) = -\sqrt{\frac{E}{\Delta E_c - E}} \tag{9.5}$$

There are no bound states ($0 < E < \Delta E_c$) to Eq. 9.5 unless a critical radius of the nanocrystal (R_c) is defined, such as:

$$R_c^2 > \frac{\pi^2\hbar^2}{8m_e\Delta E_c}. \tag{9.6}$$

The critical radius is thus dependent on the effective mass of the particle, i.e. R_c will be different for holes and electrons. It is interesting to note that for $R > R_c$ there is no quantized state. For InSb in SiO_2, the critical radius is of the order of $\sim$1 nm for the electron ($m_e = 0.015m_o$, where m_o is the mass of the electron).

There is also an upper limit to the quantum confinement effect. As a rule of thumb, the electron-hole pair Bohr radius a_o^* is often taken as the upper critical quantum measurement, that is a nanocrystal should present quantum confinement if its radius is smaller than a_o^*. For InSb, a_o^* is as high as 65.5 nm. This implies that quantum confinement can be obtained over a much wider size range than for other materials such as Si ($a_o^* \approx 4$ nm), GaAs ($a_o^* \approx 12$ nm) or InAs ($a_o^* \approx 30$ nm). A large number of physical properties are altered by the quantum confinement. In particular, the blue shift of the photoluminescence energy and of the optical absorption edge threshold compared to the bulk semiconductor is worth noting.

9.2 Results for InSb nanostructures

In the literature, the size dependency of the band gap for InSb nanocrystals has been calculated with more elaborate methods than the one presented in the previous section and corresponding experimental investigations have been carried out on different platforms by a few groups. Figure 9.3 summarizes the results of InSb nanostructures including both experimental data and calculations. The size dependency of the band gap has been calculated by the Tight Binding method (TBM) [100] and the Effective Mass Approximation (EMA) [99], where the structures considered are free of defects and the interface/surface is idealized. The modeling of nanostructures in different environments is a field of study on its

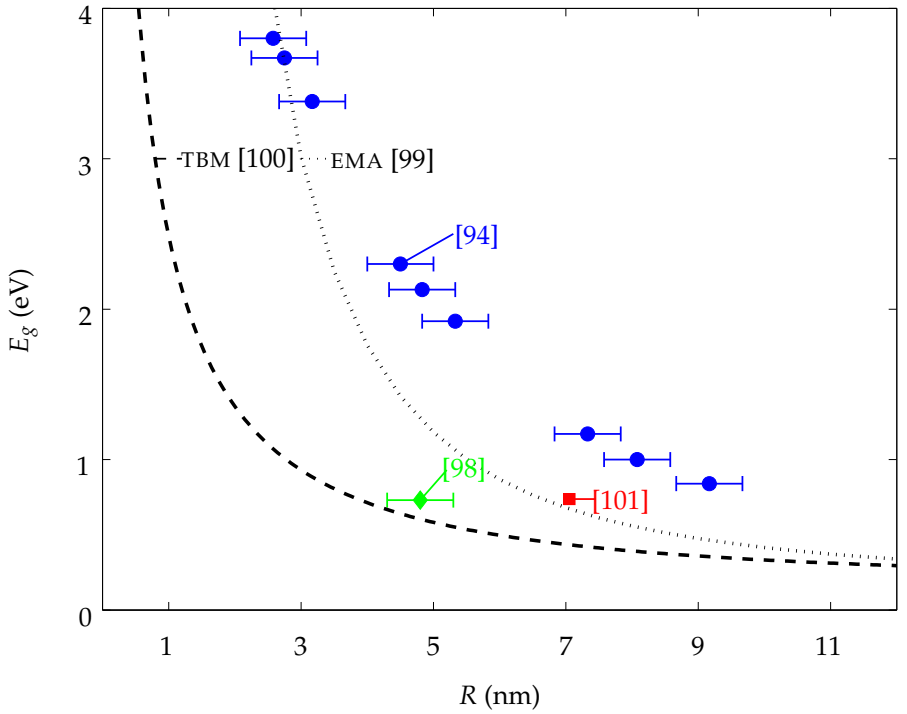

Figure 9.3: Experimental and theoretical values for the band gap of InSb nanostructures as a function of the radius. The experimental values has been extrapolated from the different references specified on the figure.

own, which is not the subject of the present project. The important message is that all numerical calculations, including the simple model presented earlier, exhibit the quantum confinement effect, i.e. the opening of the band gap with decreasing size. This effect has also been observed experimentally via photoluminescence studies as shown in Fig. 9.3 by the diamond (◆) [98] and square (■) [101] points[1]. In these two studies, the light emission observed from InSb quantum dots grown on GaSb substrate was at a much higher energy than what is expected from bulk InSb ($E_g = 0.17$ eV). Futhermore, an optical transmission study was done on InSb nanocrystals in SiO_2 by Zhu *et al.* (●) [94] where a blueshift of the

[1] In these two studies, the quantum dots have a cylindrical shape. For comparison purposes, the equivalent radius of the quantum dots was calculated from their volume.

absorption edge with decreasing size was reported. However, no photoluminescence was observed from InSb nanocrystals embedded in SiO_2, which is generally believed to be due to the existence of non-radiative recombination channels as is the case for other similar systems [102,103]. Nevertheless, the strong quantum confinement expected from models makes futher investigations on InSb nanostructures interesting.

9.3 Summary

The quantum confinement effect expected and observed in semiconductor nanostructures gives rise to interesting physical properties, such as the tunability of the absorption and emission of the structures by scaling their size on the nanometer scale. In the case of InSb nanocrystals, calculations predict that photoluminescence from the far IR up to the visible could be possible by scaling the radius of the nanocrystals from 12 nm down to 1 nm. The photoluminescence observed so far was limited to a III-V platform. Only one group reported quantum confinement of InSb nanocrystals embedded in SiO_2 by optical transmission studies. The possibility of having this highly tunable system in SiO_2, which is silicon technology compatible, is the key motivation for the work presented on the subject in this thesis.

CHAPTER 10

Formation of InSb nanocrystals

The formation of InSb nanocrystals in SiO_2 requires several steps, which will be detailed in this chapter. The first step is to deposit an alloy of InSb in SiO_2. The technique employed in this project is RF magnetron sputtering and will be described in the next section. An overview of the chambers used for this procedure is also included. After deposition, the film is heat treated in order to activate the nucleation of InSb nanocrystals and their growth. The basic principles of nucleation and growth will be outline in section 10.2 and finally, the heat treatment equipment will be briefly described.

10.1 RF magnetron sputtering

Sputtering is part of the physical vapor deposition (PVD) process family and consists of bombarding the surface of a target with high velocity positive ions, which results in ejecting the surface atoms from the target to coat a substrate. This technique presents many advantages, for example, a high uniformity of the thickness of the deposited films, a good adhesion to the substrate, a good reproducibility of the films, the ability of the deposit to maintain the stoichiometry of the original target composition, and the relative simplicity of the film thickness control. For these reasons, it became an unavoidable technique in the semiconductor and

optical device industries.

In the present project, RF magnetron sputtering was used to prepare the nanocrystals of InSb embedded in SiO_2. The following sections contain an introduction to the deposition technique and a description of the systems used in this project.

10.1.1 Basic principle

The basic setup for sputtering is to set a target on a cathode in a vacuum chamber into which an inert gas is flowed, typically argon. The initially positively charged ions will strike the target, liberating neutral surface atoms, which will eventually condense on the substrate facing the target as illustrated in Fig 10.1. When charged ions impact on the target, secondary electrons will be generated. They are accelerated towards the substrate and help ionise the gas molecules, thus sustaining the plasma or, in other words, the glow discharge. Under the right pressure conditions, the glow discharge is self-sustaining. If the pressure of the gas molecules is too low, the secondary electrons, having a free main path much higher than the ions, cannot undergo sufficient ionising collisions before they hit the substrate. On the other hand, if the pressure is too high, the ions are slowed down by inelastic collisions and do not have enough energy to produce secondary electrons. It is thus important to reach a balanced pressure in the chamber.

The most important parameter for characterising the efficiency of the sputtering process is the sputtering yield. It corresponds to the number of atoms ejected from the surface per incident particle and gives a rough estimate of the deposition rate of a material. The energy of the incident ions, the masses of the ions and target atoms, the binding energy of atoms in the target, and the geometry of the experiment are all parameters the sputtering yield depends on.

A variety of techniques are used to modify the plasma properties to achieve the optimum sputtering conditions, including usage of radio frequency (RF) alternating current and the utilisation of magnetic fields. In order to sputter isolating material, like SiO_2, RF sputtering is used. In a conventional direct-current (DC) sputtering system, the target should be a conductor in order to coat the substrate. If an insulator is substituted for the metal target, a surface positive charge is built up at the surface of the target during bombardment. In an RF sputtering configuration, an RF potential is applied to the metal electrode placed behind the target. The oscillating electrons in the alternating field caused by the RF potential

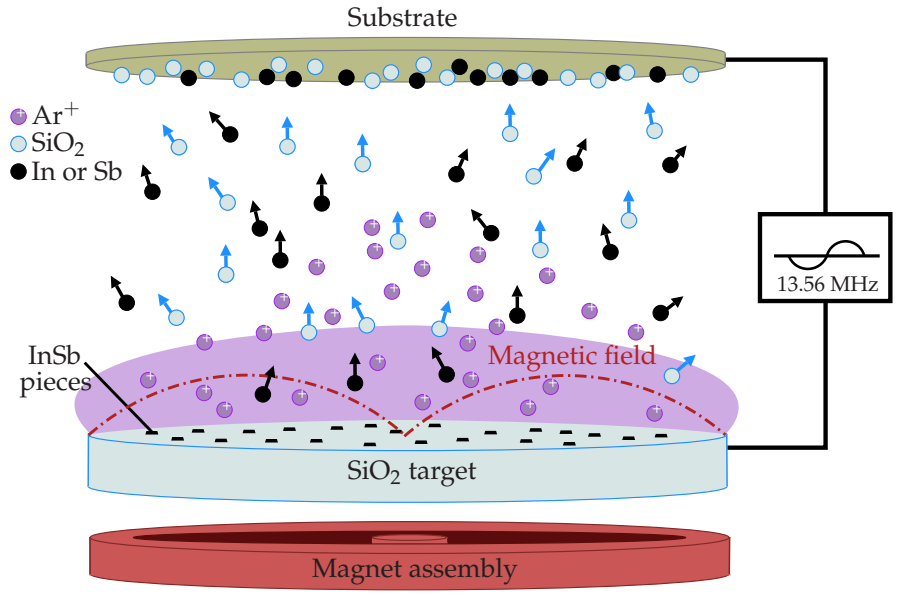

Figure 10.1: Illustration of the deposition by RF magnetron sputtering of SiO_2 thin films containing traces of In and Sb.

have enough energy to ionise the gas atoms, and the glow discharge becomes self-sustained. Due to the high mobility of electrons, as compared to ions, many more electrons will reach the surface of the target in a positive half cycle than ions in a negative half cycle. As a consequence, the target will be self-biased negatively, no positive charge will accumulate at the surface, and sputtering of the target will take place.

In order to increase the sputtering rate, RF magnetron sputtering is used. In this configuration, a magnet is placed behind the target and parallel to it. The magnetic field acts as a trap for the electrons, which travel in a helical motion along the field lines parallel to the surface of the target. The path of the electrons near the target is then extended, increasing according to the ionisation probability of the ions, which in turn increases the sputtering rate. Thus, lower power as well as lower pressure can be used, which gives films of higher quality. The drawbrack is that the electron density is not homogeneous and reaches a critical value, resulting in an irregular erosion of the target. The typical amount of target material used in a magnetron configuration is 20–30%. However, research is currently being done on the subject to obtain an optimum configuration of the magnet-target assembly. The reader is referred to reference [104] for

futher details on the subject.

10.1.2 Sputtering chambers

During this project two different chambers have been used in order to produce two different configurations of InSb nanocrystals in SiO_2. A custom-built sputtering system was first employed to obtain randomly distributed nanocrystals of InSb in SiO_2. A 100 mm diameter piece of high purity SiO_2 (99.995%) on which 5×5 mm^2 pieces of InSb (111) were attached, was used as a target. The number of pieces of InSb on the target determines the concentration of InSb in the resulting thin films, since the coverage of the target increases (decreases) by increasing (decreasing) the number of pieces. With this system, a maximum of five 2×2 cm^2 pieces of a given substrate, typically silicon and/or quartz, are coated at a time in order to obtain a good uniformity of the films for all substrate pieces. These pieces are placed at 70 mm from the target on a water cooled ($\sim$15°C) holder. High vacuum is needed in order to obtain a deposit of good quality. The chamber is thus pumped down by means of a turbomolecular pump to a base pressure of 1×10^{-7} mbar. High purity Ar (99.999%) serves as the sputter gas, which is flooded in the chamber with a flow of 30 sccm and an Ar pressure of 2×10^{-3} mbar is set for the deposition. A sputtering power density for the target of 2.6 Wcm^{-2} was found to be an appropriate choice for the deposition of the films.

Secondly, a commercial sputtering system (ATC Orion, AJA International, Inc.) was used to deposit multilayer samples of InSb and SiO_2. The multilayer configuration is achieved by alternating the sputtered target. In the present case, two 2" targets of high purity SiO_2 (99.995%) and high purity InSb (50 at% In, 50 at% Sb) are placed in the chamber and the latter is pumped by means of a turbomolecular pump down to a base pressure of $10^{-7}-10^{-8}$ mbar. With this system a whole 4" wafer can be coated and good uniformity (2%) is obtained by placing the substrate to be coated on a rotating substrate holder 100 mm over the targets. High purity Ar (99.99990%) is again used as the sputter gas at a flow of 20 sccm and the Ar pressure during the deposition is fixed to 3×10^{-3} mbar. A sputtering power of 200 W and 60 W is applied for the SiO_2 and InSb targets respectively. It is possible to heat the substrate during the deposition up to a temperature of 850°C. Finally, the deposition time determines the thickness of the layers and thus the size of the nanocrystals, as will be explained later in chapter 12.

10.2 Driving processes for the formation of nanocrystals in SiO_2

Several mechanisms are involved in the formation of nanocrystals in a SiO_2 matrix and they are highly dependent on the initial configuration of the films. The rate at which the nucleation of InSb from SiO_2 occurs depends on two factors: the thermodynamic driving force and the kinetic factor (mobility) [105]. In order for the formation of the nanocrystals to occur, it must be energically favourable. The driving force is then the decrease in the Gibbs free energy of the system that results from the formation of the nanocrystals. The second factor is the kinetic factor, which depends exponentially on temperature. It is the proportionality constant that links the driving force for nucleation and the rate of formation of nanocrystals. These two aspects are described in detail in [106] and will be outline briefly in the next section.

10.2.1 Nucleation and growth

In order for the nucleation of InSb to occur in SiO_2, there must first be a diffusion of the atoms of In and Sb to form a small volume of In and Sb atoms. From this small volume, clusters of InSb can be formed. The free energy change associated with the nucleation process can be written as:

$$\Delta G = -V\Delta G_v + A\sigma + V\Delta G_s \tag{10.1}$$

The first term in Eq. 10.1 corresponds to a volume free energy reduction ($-V\Delta G_v$) caused by the creation of a cluster of volume V. The creation of the cluster automatically leads to the creation of an interface of area A between the cluster and the host matrix and thus an increase in free energy $A\sigma$[1], where σ is the interfacial free energy. The formation of the cluster does not necessarily fit perfectly in the host matrix. In order to take this into account, a misfit strain energy (ΔG_s) is introduced in Eq. 10.1, which leads to an increase in free energy $V\Delta G_s$. Since the system under study has a spherical symmetry, Eq. 10.1 becomes:

$$\Delta G = -\frac{4\pi r^3}{3}(\Delta G_v - \Delta G_s) + 4\pi r^2\sigma \tag{10.2}$$

where r is the radius of the cluster. Equation 10.2 is illustrated in Fig. 10.2. By differentiating Eq. 10.1, one gets:

[1]The interfacial energy is assumed isotropic.

$$r^* = \frac{2\sigma}{\Delta G_v - \Delta G_s} \tag{10.3}$$

$$\Delta G^* = \frac{16\pi\sigma^3}{3(\Delta G_v - \Delta G_s)^2} \tag{10.4}$$

A cluster of $r = r^*$ is in unstable equilibrium with its surrounding. r^* is therefore called the critical cluster radius and it is associated with a maximum excess free energy ΔG^*. Hence, ΔG^* is an activation energy barrier the cluster has to cross in order to become stable.

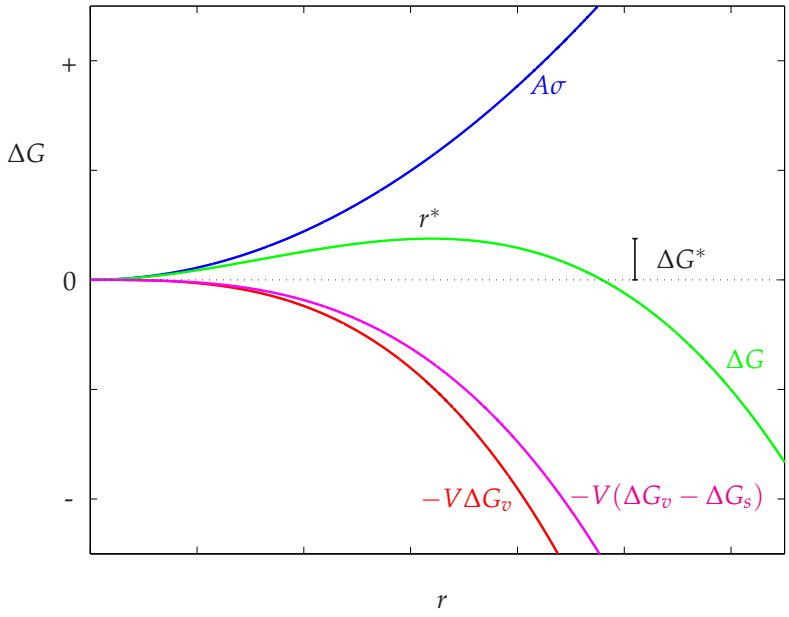

Figure 10.2: The change in free energy for a homogeneous nucleation as a function of the cluster radius r.

Given the probability of achieving this activation energy:

$$P^* = \exp(-\Delta G^*/k_B T) \tag{10.5}$$

where k_B is Boltzmann's constant and T is the temperature, the concentration of clusters of size r^* is given by [106]:

$$C^* = C_{\text{InSb}} \exp\left(\frac{-\Delta G^*}{k_B T}\right) \tag{10.6}$$

where C_{InSb} is the number of atoms of In/Sb per unit volume in the films. From Eq. 10.6, it can be seen that post-deposition heat treatment can provide the necessary thermal energy in order to ensure and increase the concentration of nucleation centers in the system, which are the seeds of the nanocrystals.

If the growth of the nanocrystals is due to mass diffusion, the InSb[2] concentration profile (C_{InSb}) at the vicinity of a nanocrystal will fulfill Fick's second law for diffusion. In spherical coordinates this equation is given by [106]:

$$\frac{\partial C_{InSb}(r,t)}{\partial t} = D_o \left(\frac{\partial^2 C_{InSb}(r,t)}{\partial r^2} + \frac{2}{r} \frac{\partial C_{InSb}(r,t)}{\partial r} \right) \tag{10.7}$$

where r is the distance from the center of the nanocrystal, t is time, and D_o is the diffusion constant of InSb in SiO_2. The molecules of InSb near the nanocrystal will tend to attach to it since it is energically favourable. Hence the concentration of InSb close to the nanocrystal will be lowered, giving rise to a concentration gradient around the nanocrystal. This will result in diffusive mass transport towards the nanocrystal, causing it to grow.

Assuming a constant concentration of InSb molecules at the surface of the nanocrystal (C^S_{InSb}), a constant concentration of InSb molecules in the nanocrystal (C^{nc}_{InSb}), a constant concentration of InSb molecules far from the nanocrystal and equal to the initial value (C^{∞}_{InSb}), and no interaction between the nanocrystals, the increase in InSb molecules in the nanocrystal ∂n needed in order for its radius to increase by ∂R is given by [107]:

$$\partial n = 4\pi R^2 (C^{nc}_{InSb} - C^S_{InSb}) \partial R. \tag{10.8}$$

The molecules will take a time ∂t to diffuse to the nanocrystal. Hence:

$$\partial n = 4\pi R^2 D_o \left. \frac{\partial C_{InSb}}{\partial r} \right|_{r=R(t)} \partial t. \tag{10.9}$$

In the limit of low supersaturation, a steady state solution to $R(t)$ can be found from Eq. 10.8-10.9:

$$R(t) = \sqrt{2 D_o S_o t} \tag{10.10}$$

[2]For simplicity, it is assumed that InSb molecules are diffusing in SiO_2. In the whole picture, the diffusion of In and Sb individually may have to be taken into account.

where S_o is the supersaturation parameter defined as:

$$S_o = \frac{C^{\infty}_{\mathrm{InSb}} - C^{S}_{\mathrm{InSb}}}{C^{nc}_{\mathrm{InSb}} - C^{S}_{\mathrm{InSb}}}. \tag{10.11}$$

In the limit of low supersaturation ($S_o \ll 1$), three main parameters influence the size of the nanocrystals: the concentration of InSb in the film, the time of the heat treatment t, and its temperature, since the diffusion constant D_o grows exponentially with the temperature[3].

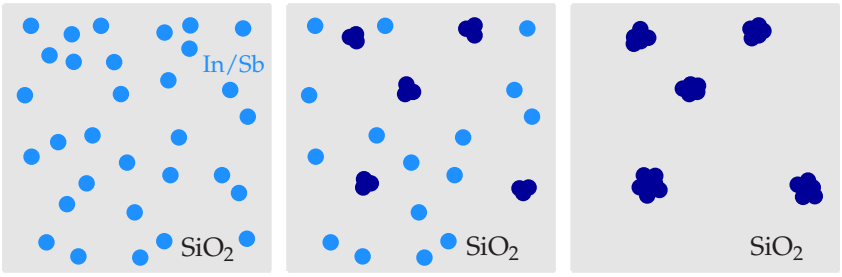

(a) Initial film (b) Nucleation (c) Growth

Figure 10.3: Illustration of the formation of nanocrystals in SiO_2. The initial SiO_2 film (a) containing atoms of In and Sb is heat treated in order to activate the nucleation (b) of nanoclusters and growth (c) of nanocrystals.

When the concentration of InSb molecules close to the nanocrystals is not sufficient to sustain their growth, the nanocrystals will start to interact. The preferential growth of large nanocrystals at the expense of the small ones will occur. This phenomenon is commonly known as Ostwald ripening. The growth rate in this situation is given by [107]:

$$\frac{\mathrm{d}R}{\mathrm{d}t} \propto \frac{1}{R^2}\left(\frac{R}{R_c} - 1\right) \tag{10.12}$$

where R_c is called the critical radius. It depends on both the supersaturation of the film and the nanocrystal/SiO_2 tension. At this stage of the process, only nanocrystals having a radius larger than R_c will continue growing.

The formation of InSb nanocrystals is summarised in Fig 10.3.

[3]The diffusion constant is often found to be well predicted by Arrhenius law.

10.2.2 Heat treatment equipment

In order to provide the necessary thermal energy for the formation of InSb nanocrystals in SiO_2, two different heat treatment setups have been used in the present project. The first is a furnace (Carbolite furnaces), which can reach 1200°C. The sample is introduced in a quartz tube in the center of the oven next to a thermocouple, which allows a precise measure of the temperature near the sample. A constant N_2 flow (40 ln/h) is used to control the atmosphere during the annealing. This technique was mostly employed for the multilayer samples.

The other system employed is a rapid thermal annealing (RTA) furnace. The system used is a Jipelec JetFirst furnace having a halogen lamp as a heat source. The emissivity of the sample is measured by a pyrometer, which in turn gives a measure of the temperature of the sample. As sharp annealing profile up to 300°C/s can be obtained. An atmosphere of N_2 (150 ln/h) and vacuum ($\sim 5 \times 10^{-4}$ mbar) were investigated for the formation of randomly distributed InSb nanocrystals in SiO_2.

10.3 Summary

This chapter presented the steps for the formation of InSb nanocrystals in SiO_2. RF magnetron sputtering is first employed to deposit a thin film of SiO_2 containing InSb in a randomly distributed or in a multilayer configuration. In order for the nucleation of the nanocrystals and their growth to occur, the films are heat treated, providing the thermal energy necessary to activate the processes. After a description of the several characterisation techniques used in this project (chapter 11), the results of the formation of InSb nanocrystals in SiO_2 will be presented (chapter 12).

CHAPTER 11

Characterisation of InSb nanocrystals embedded in SiO_2

This chapter will present the different techniques used to characterise the SiO_2 thin films containing InSb. This includes X-ray diffraction, transmission electron microscopy and Rutherford back scattering spectrometry. The principle behind the techniques, their purposes and a description of the apparatus utilised in the present project are contained in the following.

11.1 X-ray diffraction

Due to their short wavelength ($\sim$Å) X-rays are well suited to probe the inner structure of materials. This non-destructive technique was employed on InSb nanocrystals in order to gain information such as lattice distances, macro-strains, and crystal structures. The basic theory of X-ray diffraction followed by a short description of the experimental setup will be introduced in this section.

11.1.1 Basic theory

X-ray diffraction is an elastic scattering process involving an incident monochromatic electromagnetic wave, which is scattered by all the elec-

trons of the atoms probed by the incident beam. The elementary scattering unit of an X-ray in an atom or a crystal is the electron. Considering the classical description of the scattering process, an electron placed in the electric field of an incident X-ray beam will be forced to oscillate at the same frequency and in the same direction as the incident beam, thus radiating just like a small dipole antenna. The radiated wave or the *scattered wave* from the electron at an angle ξ from the direction of propagation of the incident wave, far from the electron, can be expressed as [108]:

$$\psi_s(R) = -\psi_i r_o \frac{e^{ikR}}{R} cos\xi \tag{11.1}$$

where $r_o = 2.82 \times 10^{-5}$ Å is the Thomson scattering length. The measure of the scattering amplitude from the electron can be defined by the scattering electron factor $f^e = r_o cos\xi$.

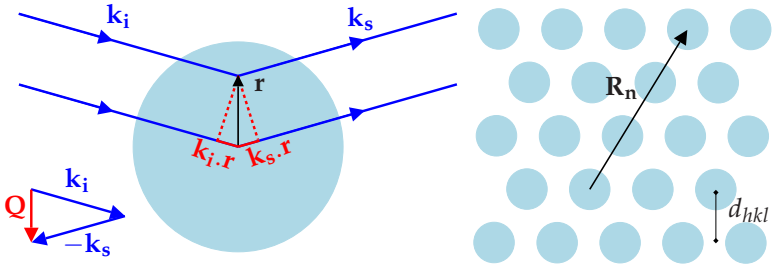

(a) Atom (b) Crystal

Figure 11.1: (a) Scattering from an atom. (b) A lattice of atoms with position $\mathbf{R_n}$, and lattice spacing of d_{hkl}.

In an atom of Z electrons, the scattered radiation field is a superposition of the contributions from different volume elements of the electron distribution, specified by a number density $\rho(\mathbf{r})$. This superposition of scattered waves makes it important to keep track of the phase. The phase difference of the scattered wave interacting from two different volume elements, as depicted in Fig. 11.1(a), can be written as:

$$\Delta\phi(\mathbf{r}) = (\mathbf{k_i} - \mathbf{k_s}).\mathbf{r} = \mathbf{Q}.\mathbf{r} \tag{11.2}$$

where $\mathbf{Q}$ is the wavevector transfer and $\mathbf{k_i}$ ($\mathbf{k_s}$) is the wavevector of the incident (scattered) wave (for elastic scattering $|\mathbf{k_i}| = |\mathbf{k_s}| = 2\pi/\lambda$, where λ is the wavelength of the X-rays). The atomic scattering factor (f^a), which is a measure of the amplitude of a wave scattered from the

isolated atom, is found by integrating the scattering amplitude from all the volume elements of the electron distribution:

$$f^a(\mathbf{Q}) = \frac{\text{Amplitude of the scattered wave from an atom}}{\text{Amplitude of the scattered wave from an electron}} \quad (11.3)$$

$$= \int \rho(\mathbf{r}) e^{i\mathbf{Q}.\mathbf{r}} d\mathbf{r} \quad (11.4)$$

This form factor is found to be the Fourier transform of the electron distribution.

In the same way, one can define the scattering factor from a crystal. A crystalline material can be constructed by repeating periodically a spatial arrangement of atoms called a unit cell. The position of the unit cells in the crystal is specified by $\mathbf{R_n} = n_1\mathbf{a} + n_2\mathbf{b} + n_3\mathbf{c}$ (Fig. 11.1(b)) where n_i are integers and $(\mathbf{a}, \mathbf{b}, \mathbf{c})$ are the primitive vectors spanning the periodic array or, in other words, the Bravais lattice. If the vectors $\mathbf{r_j}$ denote the position of the atoms within the unit cell with respect to its origin, the position of any atom in the crystal is given by $\mathbf{R_n} + \mathbf{r_j}$. The scattering amplitude of the crystal can then be written as [108]:

$$F_{crystal}(\mathbf{Q}) = \underbrace{\sum_{\mathbf{r_j}} f_j^a e^{i\mathbf{Q}.\mathbf{r_j}}}_{\text{Unit cell structure factor}} \underbrace{\sum_{\mathbf{R_n}} e^{i\mathbf{Q}.\mathbf{R_n}}}_{\text{Lattice sum}} \quad (11.5)$$

In the lattice sum in Eq. 11.5, the phase factors are located on the unit circle in the complex plane, and the sum will be of the order of unity except, for the scattering vectors fulfilling:

$$\mathbf{Q}.\mathbf{R_n} = 2\pi m \qquad m = 1, 2, ..., \quad (11.6)$$

in which case it becomes of the order of N, the number of unit cells. The unique solution of Eq. 11.6 is the reciprocal lattice vector $\mathbf{G_{Hal}} = h\mathbf{a}^* + k\mathbf{b}^* + l\mathbf{c}^*$ where (h, k, l) are integers and the reciprocal basis vectors ($\mathbf{a}^*$, $\mathbf{b}^*$, $\mathbf{c}^*$) are given by:

$$\mathbf{a}^* = \frac{2\pi(\mathbf{b} \times \mathbf{c})}{\mathbf{a}.(\mathbf{b} \times \mathbf{c})} \qquad \mathbf{b}^* = \frac{2\pi(\mathbf{c} \times \mathbf{a})}{\mathbf{a}.(\mathbf{b} \times \mathbf{c})} \qquad \mathbf{c}^* = \frac{2\pi(\mathbf{a} \times \mathbf{b})}{\mathbf{a}.(\mathbf{b} \times \mathbf{c})}. \quad (11.7)$$

This leads to the Laue condition for the observation of X-ray diffraction from a crystal lattice:

$$\mathbf{Q} = \mathbf{G_{hkl}}. \quad (11.8)$$

Each point in the reciprocal lattice (h,k,l) corresponds to a plane in the direct lattice that intercepts the points $(\mathbf{a}/h, \mathbf{b}/k, \mathbf{c}/l)$. It can be shown that $\mathbf{G_{hkl}}$ is perpendicular to the planes with Miller indices (hkl) and:

$$|\mathbf{G_{hkl}}| = \frac{2\pi}{d_{hkl}} m \tag{11.9}$$

where d_{hkl} is the lattice spacing of the (hkl) planes and n is an integer (a possible common factor of the Miller indices). In the particular case of cubic structures, the lattice spacing becomes:

$$d_{hkl} = \frac{a}{\sqrt{h^2+k^2+l^2}} \tag{11.10}$$

where a is the lattice parameter.

Since $|\mathbf{Q}| = 2|\mathbf{k}|\sin\theta$ and $|\mathbf{k}| = 2\pi/\lambda$, the Laue condition (Eq. 11.8) is equivalent to Bragg's law:

$$2d_{hkl}\sin\theta = n\lambda. \tag{11.11}$$

In the same way as for scattering from an atom, the structure factor of a crystal is the Fourier transform of the electron distribution. This means that if the structure factor is known, the electron distribution within the unit cell can be found by taking the Fourier transform of the structure factor. The measured quantity in X-ray diffraction experiments is the diffracted intensity, which is proportional to the square of the norm of the structure factor $|F_{crystal}(\mathbf{Q})|^2$. As a consequence, the phase information of the structure factor is not available. This is known as the phase problem in crystallography. However, several techniques have been developped to solve the problem and model the measured structures.

The equations derived earlier in this section assume an infinite crystal without any defect. A reduction of the direct lattice size, i.e. a finite crystal size or a finite coherence length of the diffraction domain, gives a broadening in the reciprocal lattice, which follows from the length-wavevector inverse relationship. It can be illustrated by taking the norm square of the crystal scattering amplitude while assuming a finite size in the **a** direction [108]:

$$|F_{crystal}(\mathbf{Q})|^2 = |F_{u.c.}(\mathbf{Q})|^2 \left\{ \frac{\sin\frac{N_a\mathbf{Q}.\mathbf{a}}{2}}{\sin\frac{\mathbf{Q}.\mathbf{a}}{2}} \right\}^2 N_b N_c b^* c^* \delta(\mathbf{Q_{yz}} - \mathbf{G_{hkl}}) \tag{11.12}$$

N_a, N_b, and N_c correspond to the number of unit cells in the **a**, **b**, and **c** direction respectively, $F_{u.c.}$ corresponds to the unit cell contribution to the crystal scattering amplitude, and δ is the Dirac delta function. A finite crystal size introduces a broadening of the diffraction peak since the sinusoidal term has a finite breath. From Eq. 11.12 or Eq. 11.11, it is possible to obtain a relationship between the crystal size and the broadening of the diffraction peak [109]:

$$\beta = \frac{0.89\lambda}{D\cos\theta} \tag{11.13}$$

where β is the breadth of the diffraction peak and D is the mean dimension of the crystal. Eq. 11.13 is the well known Scherrer equation.

In order to calculate the absolute intensity of the X-rays diffracted from a crystal, several parameters have to be taken into account, i.e. the polarisation of the source, the Lorentz, temperature, and extinction factors, etc [108]. However, diffractograms showing relative diffracted intensities are presented in this thesis since they containt the relevant information.

11.1.2 Experimental setup

In order to gain information on the crystalline structure of InSb nanocrystals, Bragg-Brentano X-ray diffraction (BBXRD), also called specular high-angle X-ray diffraction or $\theta - 2\theta$ scans, scattering geometry was used. The characteristic of this geometry is that the scattering vector **Q** is kept perpendicular to the sample surface as illustrated in Fig. 11.2. As a consequence, only the crystallographic planes parallel to the sample surface meet the Bragg diffraction condition and thus, only information on the out-of-plane direction of the structures can be extracted. The crystalline phases present in the sample, the crystallinity, the lattice parameter, and the out-of-plane average crystalline size are examples of the information gained with BBXRD measurements.

A Bruker D8 Discover diffractometer (Bruker AXS GmbH, Karlsruhe, Germany) was used to perform the BBXRD measurements. The X-ray source is a water-cooled stationary Cu-anode bombarded with 40 keV electrons causing bremsstrahlung and radiation characteristic of the Cu-anode. The radiation from Cu-K_α, at a wavelength of $\lambda = 1.5418$ Å[1], is selected and focused with a Göbel mirror. A 3×3 mm direct beam

[1]The Cu-K_α radiation is a weighted sum of the Cu-$K_{\alpha 1}$ and Cu-$K_{\alpha 2}$ wavelengths.

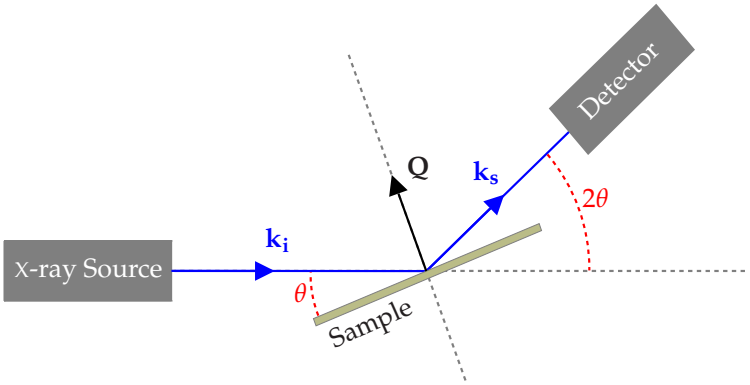

Figure 11.2: Bragg-Brentano X-ray diffraction geometry, where the scattering vector **Q** is perpendicular to the sample surface.

aperture and a Sollers slit limit the divergence of the incident beam on the sample. Finally, a pair of slits (0.6 mm and 1 mm) are placed in front of the scintillator in order to exclude from the detector all the X-rays except those emanating from the sample. The scattering angle 2θ was typically varied from 10° to 60°, which corresponds to a depth penetration ($10^3 - 10^4$ nm) exceeding the film thicknesses investigated.

11.2 Transmission electron microscope

Transmission electron microscopy (TEM) allows a better resolution due to the smaller wavelength of electrons compared to photons used in conventional optical microscopes. It was used in the current project in order to get morphological and structural details via direct imaging of the nanocrystals of InSb, together with diffraction analysis of the investigated samples. The microscope used through this project will be briefly described. This will be followed by the basic principles of the operation modes of TEM (for more information on the subject, the reader is referred to [110]) and a short description of the sample preparation techniques.

11.2.1 The microscope

A TEM can be divided in three major parts: the illumination system including the electron gun and condensers, the image forming system, which consists of the objective lens, and the projection system. The TEM used in this study is a Philips CM20. A schematic diagram of it is shown

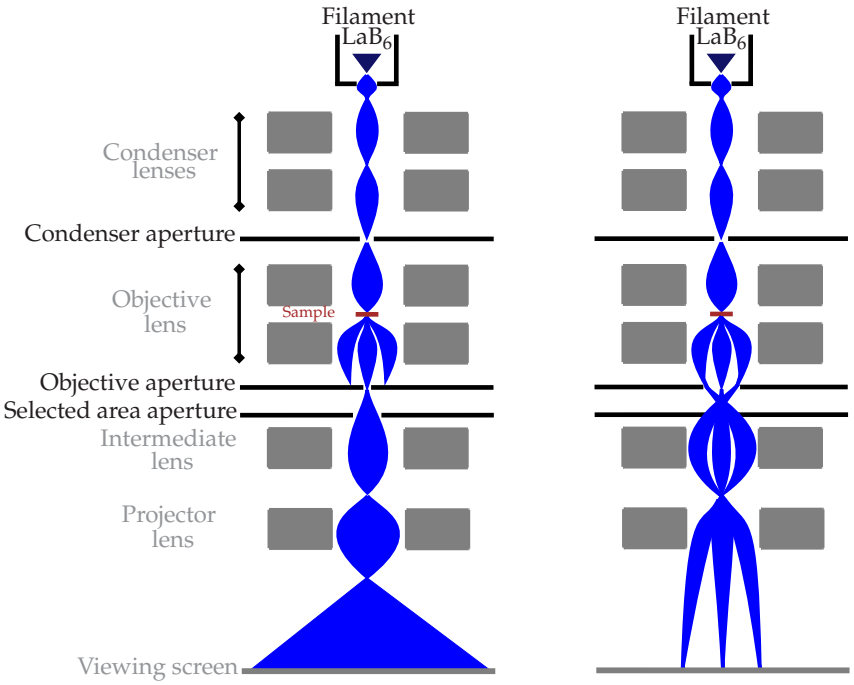

(a) Image mode (b) Diffraction mode

Figure 11.3: Schematic diagram of a transmission electron microscope in the bright-field imaging mode (a) and diffraction mode (b).

in Fig. 11.3. The thermionic emitter is a lanthanum hexaboride (LaB_6) cathode offering a high brightness and a high density beam current. The electrons are electrostaticaly accelerated at a potential of $V = 200$ keV. The corresponding wavelength of the relativistic electrons can be calculated with the following expression:

$$\lambda = \frac{h}{\sqrt{2m_o eV\left(1+\frac{eV}{2m_o c^2}\right)}} = 0.0251 \text{ Å} \tag{11.14}$$

where h is Planck's constant, m_o the rest mass of the electron, e the electronic charge, and c the speed of light. A set of condenser lenses collect the electrons over a large solid angle and focus them onto the sample. An aperture follows the condenser to limit the beam divergence, reduce the beam load on the sample, and stop stray electrons. The immersion objective lens is the first lens in the image forming system. This configuration

of the sample-objective lens helps minimise the aberration effects. An objective aperture located in the back focal plane of the objective lens can be used to control the image contrast. The image formed by the objective lens is further magnified by the projector lenses, and projected onto a fluorescent screen or coupled to a CCD camera. In order to avoid electron scattering from particles in the tube or contamination of the sample, the column is kept at a pressure of $\sim 10^{-7}$ mbar.

11.2.2 Modes of operation

Four different modes of operation were used: bright-field imaging, diffraction mode, selected area diffraction, and high resolution imaging.

Bright-field (BF) imaging uses the central spot, i.e. the beam transmitted directly through the sample, to form the image. The result contains bright regions corresponding to electrons that have not been scattered and *vice versa* for the dark regions. For amorphous structures, a better contrast of the image can be achieved by reducing the size of the objective aperture, thereby filtering more scattered electrons. In the same way, the objective aperture can be reduced to block the diffracted electrons from crystalline structures, thereby achieving a better contrast of the image.

In diffraction mode, the diffraction pattern is formed at the back focal plane of the objective lens, and then imaged on the viewing screen. As explained in the previous section (section 11.1), diffraction can give information on crystalline phases present in the sample and their orientation. In the present study, the nanocrystals are randomly oriented in an amorphous matrix of SiO_2. This means that the reciprocal lattice vectors are also randomly oriented, which leads to a diffraction pattern consisting of concentric circles. The diameter of the circles will depend on $\mathbf{Q}$ (see also section 11.1).

In order to select a specific area of the sample, a selected-area aperture is placed in the image plane of the objective lens, which acts as a virtual diaphragm in the plane of the sample, thereby limiting the size of the beam on the sample. This configuration is useful when diffraction from a precise area of the sample is needed. In the present work, the silicon contribution to the diffraction pattern was eliminated when using a cross-section TEM sample, resulting in a diffraction pattern of the thin films only.

Finally, high resolution TEM (HRTEM) was employed to confirm the crystalline structure of the nanocrystals. Some of the lattice planes of the crystals parallel to the electron beam will be close enough to the Bragg

position to diffract the primary beam. As stated before, the diffraction pattern is the Fourier transform of the periodic electron distribution in the crystal (section 11.1.1). The objective lens focuses both the direct beam and the diffracted beam, which will interfere providing an inverse-transformation leading to an enlarged picture of the periodic charge distribution. This interference pattern is magnified in the same way as the image of the sample, and both are displayed on the viewing screen. This is done by selecting the direct beam together with one or more of the diffraction rings with the objective aperture in the diffraction mode. It is important to note that only the lattice planes having the appropriate orientation will be seen. Futhermore, the image forming system has to be corrected for astigmatism since any direction dependent misalignments of the beam would destroy the interferences.

11.2.3 Sample preparation

In order to get good TEM images, the sample has to be transparent to electrons, which means having a thickness of 100 nm or less, depending on the material under study. The preparation of the TEM sample is then a critical step. Two different kinds of sample have been investigated, namely planar view samples and cross-section samples. Planar samples are prepared by dimple grinding and low-angle ion milling using 5 keV Ar^+ ions. Since the structures studied are embedded in a isolating material (SiO_2), it was necessary to coat the planar view sample with carbon[2] in order to avoid charging effects. It is important to note that planar view samples do not give any depth dependent information, since the thickness of the sample varies and only 100 nm from the surface of the sample is transparent. On the other hand, as the name indicates, cross-section sample provides depth profile resolution. It is prepared by glueing two pieces of the sample surface to surface and afterwards, mechanically thinning it by dimpling, followed by low-angle Ar-ion milling.

11.3 Rutherford back scattering spectrometry

Another analytical technique commonly used in material science is Rutherford back scattering spectrometry (RBS) [111, 112]. It is an absolute technique and it is used to obtain a depth profile of the chemical composition

[2]Carbon is preferred to gold when dealing with TEM since it is amorphous while being a conductor.

of a sample. Figure 11.4 illustrates the principle.

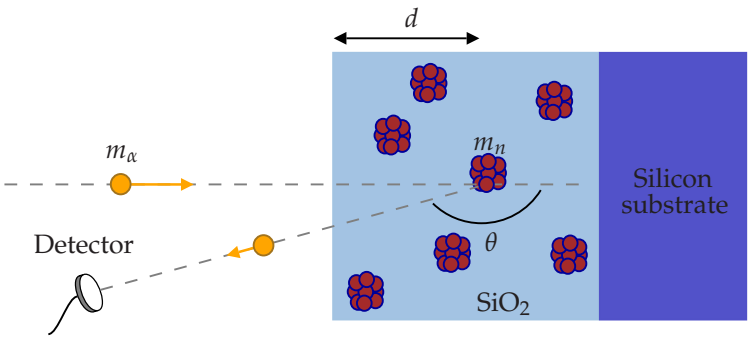

Figure 11.4: Schematic of RBS principle.

A beam of α particles (He^+) of mass m_α accelerated by a Van der Graff accelerator to a primary energy of 1.5 MeV is directed on a sample, and a detector is placed such that scattered ions from the sample at an angle θ close to 180° will be collected[3]. The Rutherford type scattering occurs because of coulomb repulsion between the positively charged incident ions and the positively charged nuclei in the sample. The recoil energy of these ions will depend on their incident energy E_i and on the mass of the scattering positively charged nuclei (m_n) in the sample. The energy of the ions after a Rutherford collision for a fixed scattering direction is given by [112]:

$$E_f = E_i \left(\frac{m_\alpha \cos(\theta) + \sqrt{m_n^2 - m_\alpha^2 \sin^2(\theta)}}{m_n + m_\alpha} \right)^2 \tag{11.15}$$

$$E_f \equiv KE_i \tag{11.16}$$

where K is known as the kinematic scattering factor. Thus, the measured energy of the scattered ions indicates the qualitative composition of the sample under investigation. Additionally, if the incident ion is not scattered by any atom at the surface, but by one deeper in the sample, the incident ion will have its energy reduced upon impact since it loses energy due to coulomb interactions with the electrons in the solid. The same holds for the outcoming scattered ions. The total energy loss can thus be

[3] In the actual measurement, the detector is placed at an angle of 19° with respect to the incident beam.

converted to a corresponding scattering depth. In this way, a RBS spectrum contains information on the chemical composition depth profile of a sample.

11.4 Summary

The different techniques used during this project in order to characterise InSb nanocrystals embedded in SiO_2 have been presented in this chapter. First, X-ray diffraction was described which is used for determining the presence of the crystals, their structures, and their strain state. Transmission electron microscopy is a powerful technique in order to verify the presence of nanocrystals and obtain their size distribution. Finally, Rutherford back scattering spectrometry was used to obtain the chemical composition depth profile of randomly distributed SiO_2 InSb-doped thin films. The results concerning the formation of InSb nanocrystals in SiO_2 are detailed in the next chapter.

CHAPTER 12

Experimental results for InSb nanocrystals in SiO_2

The formation of InSb nanocrystals in SiO_2 was first demonstrated by Zhu *et al.* [94] and attempted more recently by Capoen *et al.* [95]. Zhu *et al.* showed that InSb nanocrystals embedded in SiO_2 can be obtained by depositing a SiO_2 film doped with InSb by RF sputtering, at a RF power of 200 W, a pressure of Ar of 4×10^{-3} mbar, and by post deposition heat treatment in vacuum in the temperature range of 300-400°C. The band gap energy for different size distributions of InSb nanocrystals was extrapolated from optical transmission measurements, which showed a blue shift of the band gap expected from quantum confinement effect. However, they omitted to report the concentration of InSb in the initial SiO_2 films, which makes the results very difficult to reproduce.

In a more recent study, Capoen *et al.* investigated the structural and optical properties of InSb-doped SiO_2 films. They obtained InSb nanocrystals with a size ranging from 1 nm up to 100 nm by post deposition RTA at various temperatures of RF sputtered SiO_2 films containing 12.5 at% of InSb. The concentration of InSb was assumed by measuring the surface ratio of InSb on the SiO_2 target. The optical transmission of these films was investigated and, as opposed to Zhu *et al.*, they recorded no size-dependency of the absorption spectra.

These two studies were the starting point for the present project. Sev-

eral SiO_2 thin films containing different concentrations of InSb were investigated. Different heat treatments were tried and the results obtained by furnace annealing will be discussed first. This will be followed by the RTA investigation, which showed a concentration threshold for the formation of InSb nanocrystals in SiO_2. Preliminary results of absorption measurements of SiO_2 films containing nanocrystals of InSb will then be presented. Furthermore, the melting and solidification of InSb nanocrystals embedded in SiO_2 was studied *in situ* in the TEM. Experimental results and calculations of these processes are included in this chapter. Finally, the preliminary results for InSb nanocrystals in a multilayer configuration will be shown.

12.1 InSb nanocrystals randomly distributed in SiO_2

12.1.1 Heat treatment: furnace annealing

Different concentrations of InSb in SiO_2 films ranging from 1 at% to 6 at%, measured by RBS, were deposited on a Si substrate[1] and investigated. Figure 12.1(a) shows the InSb profile in an as deposited SiO_2 film (plain black curve) determined by RBS, together with the simulation of the depth profile (dashed green curve) enabling the determination of the concentration of InSb in the film. The simulation was done using the RUMP package [113]. The presence of In and Sb in the film can be seen by the increase in RBS yield in the channel range 220-310[2] . The concentration was determined from the simulation to be 1 at% of In/Sb. It should be noted that the kinematic factors of In and Sb are very similar, which makes it difficult to distinguish between the two elements in a RBS measurement. This is illustrated in Fig. 12.1(b). Three difference simulations of the film are presented: a film containing 0.5 at% of In and 0.5 at% of Sb (green dashed curve), a film containing 1 at% of In (■ curve), and a film containing 1 at% of Sb (◆ curve). The simulation of a film containing the same amount of In and Sb corresponds better to the measurement (plain black curve). The relative concentration of In and Sb was confirmed by proton induced X-ray emission (PIXE) [114] for a higher concentration sample, which will be discussed later in this section, and a relative amount of 52% In and

[1] In all cases, the films are deposited on a Si (100) substrate having a resistivity of 3000 Ωcm.

[2] The channel should be understood as an energy channel. The higher the channel, the higher the energy of the scattered particles.

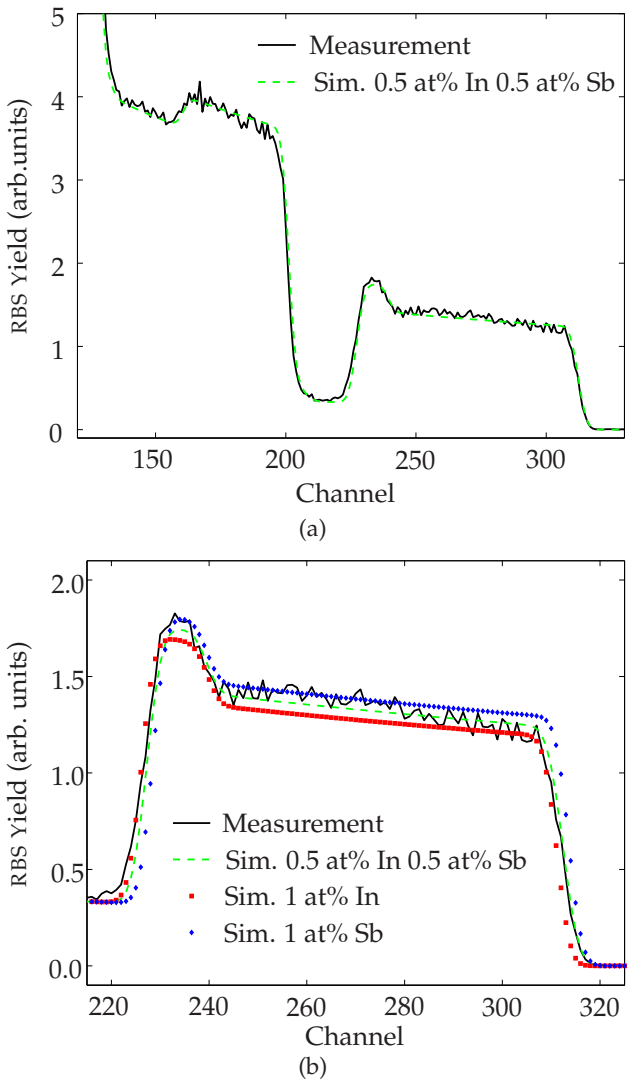

Figure 12.1: (a) RBS spectrum of a SiO_2 film containing InSb as deposited (plain black curve) and the simulation of the depth profile allowing the determination of the concentration of InSb in the film (dashed green curve). (b) Simulation of the depth profile with different relative concentration of In and Sb: 0.5 at% of In and 0.5 at% of Sb (green dashed curve), 1 at% of In (■), and 1 at% of Sb (◆)

48% Sb was found. A small amount of Ar from the deposition process is also present in the film, which contributes to the increase of RBS yield in the channel range 150-240 and a concentration of 2 at% was found from the simulation of the film.

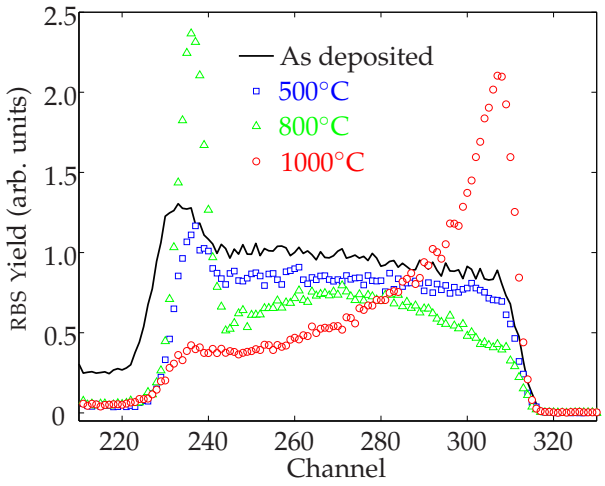

Figure 12.2: Evolution of the RBS spectrum as a function of temperature for the heat treatment of a SiO_2 film containing 1 at% of InSb: as deposited (black plain curve), at 500°C (❑), at 800°C (Δ), and at 1000°C (❍).

The sample was cleaved into several pieces and heat treated for one hour under a constant flow of N_2 in a furnace at different temperatures ranging from 200°C up to 1000°C in steps of 100°C. These were investigated by RBS in order to obtain the evolution of the InSb depth profile as a function of the heat treatment temperature. The results are presented in Fig. 12.2. For clarity, only spectra presenting changes in the InSb profile are shown. Except for the evaporation of Ar, the profile is constant up to a temperature of 500°C. For higher temperatures, a pile up of material both at the surface and at the SiO_2/Si interface is seen. These results indicate that the temperature and the time of the heat treatment were in the right range to enable the diffusion of In and Sb in the SiO_2 film. It was found that no samples contained InSb nanocrystals. Thus, it can be concluded that the formation of nanocrystals for these heat treatment conditions is not energically favoured.

Heat treatment of the same films under vacuum (10^{-6} mbar) for one hour and four hours at 300°C and 400°C, as done in [94], was also tried.

In all cases, no InSb nanocrystals were observed by XRD nor by TEM. These heat treatments were repeated for two different concentrations of InSb, 3 at% and 6 at%, without any success. The results presented in this work confirmed those of Capoen *et al.* [95], who also tried to reproduce the work done by Zhu *et al.* [94] without succeeding. The main reason for this difference is likely to be the concentration of InSb in the SiO_2 film, which was not specified in [94], even though a broad range of concentrations was tried (1 at%, 3 at%, 6 at%, and 12.5 at% in [95]).

12.1.2 Heat treatment: RTA

Inspired by the work of Capoen *et al.* [95], RTA heat treatment was also tried in order to form InSb nanocrystals embedded in SiO_2. SiO_2 films containing InSb at different concentrations (1 at%, 3 at%, 6 at%, and 10 at%) deposited on a Si substrate were heat treated by RTA at temperatures ranging from 600°C to 1000°C, for different times (60 s to 480 s) and different heat treatment atmosphere (constant N_2 flow and vacuum).

Figure 12.3 shows cross-section TEM images of SiO_2 films containing different concentrations of InSb. The films have had the same heat treatment, namely RTA at 900°C for 60 s under a constant N_2 flow. The concentration of the different samples was measured by RBS, giving 1 at% (Fig 12.3(a)), 3 at% (Fig 12.3(b)) and 6 at% (Fig 12.3(c)). Nanocrystals of InSb are present only in the high concentration sample. A high resolution TEM image of a 15 nm InSb nanocrystal is also shown in the inset of Fig 12.3(c). Low concentration films present nanoclusters, but the exact composition could not be obtained. These results indicate that there is a threshold in concentration in order for the nanocrystals to form by RTA. In order to verify this, the low concentration samples were heat treated at different temperatures (600°C to 1000°C) and for different times (60 s to 480 s). No formation of InSb nanocrystals was detected.

Two different concentrations of InSb in SiO_2 showed the formation of InSb nanocrystals after RTA heat treatment at temperature higher than 600°C: 6 at% and 10 at%. The relative concentration of In and Sb was confirmed by PIXE [114] for the 10 at% concentration sample and a relative amount of 52% In and 48% Sb was found. As expected the size of the nanocrystals formed is related to the concentration of InSb initially in the film. Figure 12.4(a) shows a cross-section TEM image of the 6 at% concentration film heat treated by RTA for 120 s at 900°C under a constant flow of N_2. The corresponding size distribution of the nanocrystals is presented in Fig. 12.4(b). The size distribution is obtained from mea-

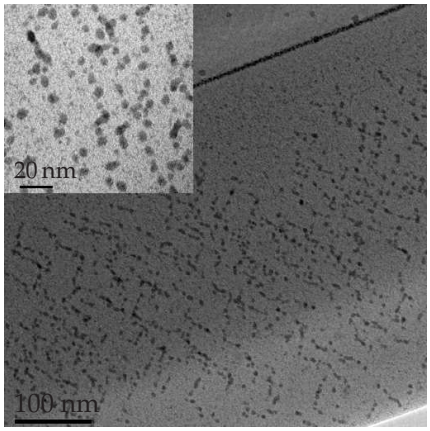

(a) 1 at%

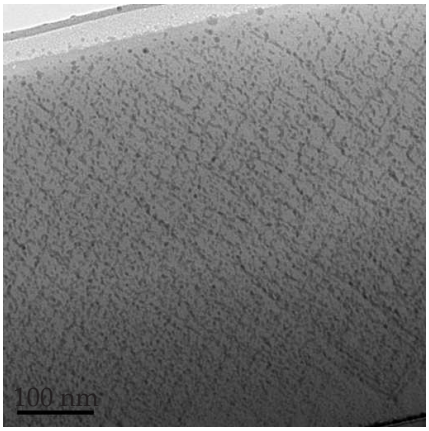

(b) 3 at%

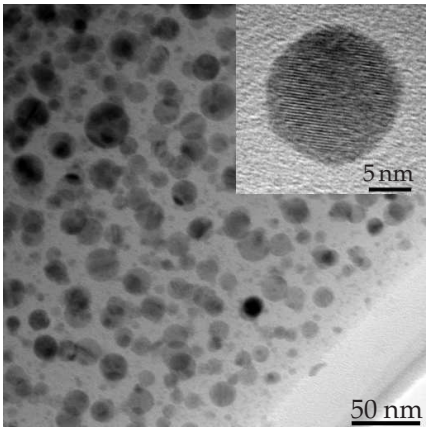

(c) 6 at%

Figure 12.3: Cross-section TEM images of SiO_2 film containing different concentrations of InSb heat treated by RTA 60 s at 900°C: (a) 1 at%, (b) 3 at%, and (c) 6 at%.

suring the diameter of each nanocrystals in the cross-section TEM image. For this sample, the nanocrystals have a mean diameter of 19.8 ± 0.3 nm. If heat treated in the same way, 10 at% concentration gives nanocrystals with a mean diameter of 22.6 ± 0.7 nm, which corresponds well with a square root dependency of the size of the nanocrystals on the concentration as presented earlier in section 10.2.

The sample presented in Fig. 12.4 was studied by RBS to obtain the evolution of the InSb profile after the RTA heat treatment. The results are

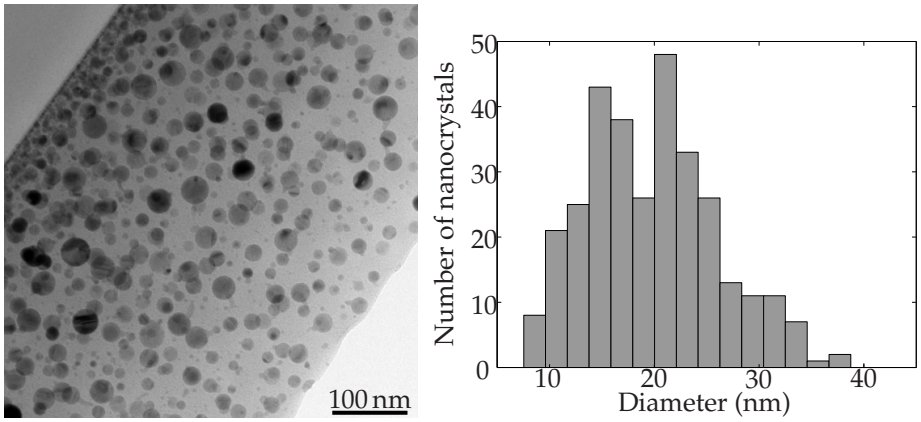

(a) (b)

Figure 12.4: (a) Cross-section TEM image of a SiO_2 film containing 6 at% of InSb heat treated by RTA for 120 s at 900 under a constant flow of N_2. The Si substrate is seen in the top left corner. (b) Size distribution of the nanocrystals presented in (a).

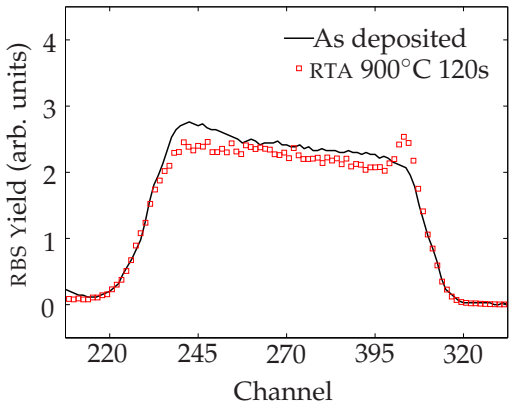

Figure 12.5: RBS spectrum before (plain black curve) and after (❑) RTA heat treatment at 900°C for 120 s for a SiO_2 film containing 6 at% of InSb.

shown in Fig. 12.5. It can be seen from the RBS spectrum that there is a pile up of material at the surface of the film after heat treatment. This accumulation of material is not present in the TEM image (Fig. 12.4), but could have been removed during the preparation of the TEM sample (see section 11.2.3). Nevertheless, the InSb profile in the film after RTA heat

treatment is rather uniform, which is confirmed by the TEM investigation showing a homogenous distribution of the nanocrystals throughout the film.

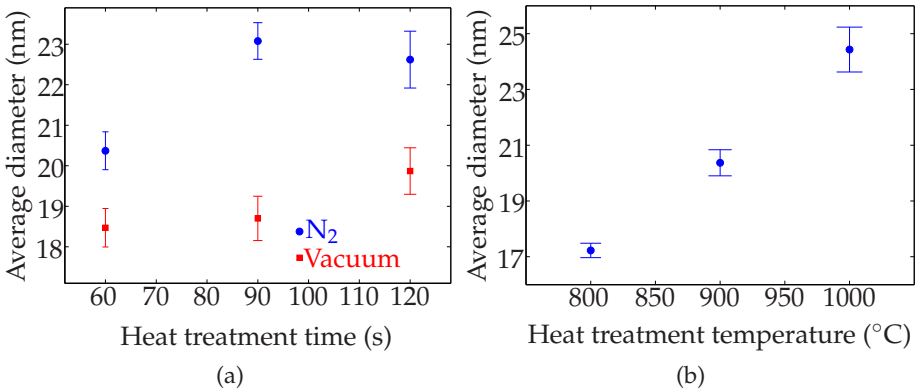

Figure 12.6: (a) Mean diameter of InSb nanocrystals RTA heat treated at 900°C as a function of the heat treatment time for two different heat treatment atmospheres: a constant flow of N_2 (●) and under vacuum (■). (b) Mean diameter of InSb nanocrystals RTA heat treated for 60 s in a constant flow of N_2 as a function of the heat treatment temperature.

The size distribution as a function of the RTA heat treatment time, atmosphere, and temperature was investigated for the 10 at% concentration. The results are shown in Fig. 12.6. In Fig. 12.6(a) an isothermal heat treatment is presented (900°C), while in Fig. 12.6(b) an isochronal heat treatment in the same atmospheric conditions is shown. Three main conclusions can be drawn from the results. First, the average diameter of the nanocrystals increases with the heat treatment time, but not in a square root manner as predicted by Eq. 10.10. This can be explained by the high concentration of InSb in the film, which means that the low supersaturation limit is not respected. Moreover, Ostwald ripening may be occuring, indicating interactions between the nanocrystals. Secondly, the average diameter of the nanocrystals is ~ 1.2 times larger when the heat treatment is done with a constant flow of N_2 compared to a heat treatment done under vacuum. Finally the average diameter increases with the temperature of the heat treatment. In addition, as expected from section 10.2, by changing the temperature of the heat treatment, a wider range for the size of the nanocrystals can be obtained.

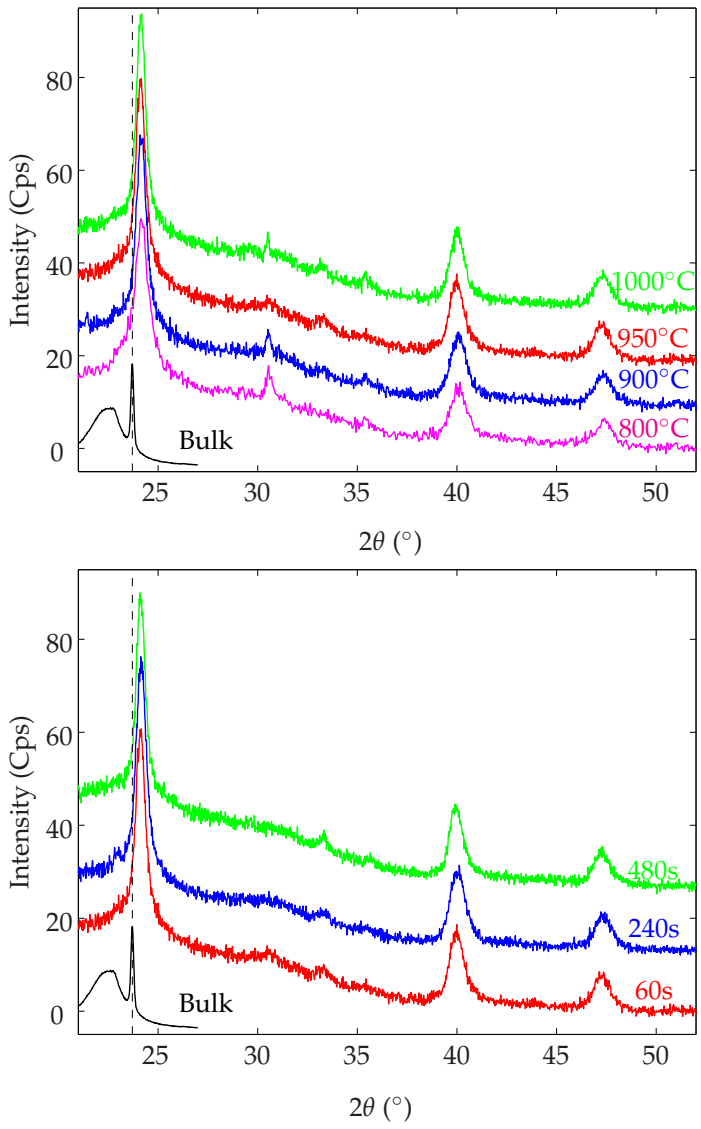

Figure 12.7: XRD spectra of InSb nanocrystals formed with different heat treatment conditions: (a) RTA for 60 s under a constant N_2 flow for different temperatures and (b) RTA at 900°C under a constant N_2 flow for different times.

The crystallinity and the structure of the InSb nanocrystals were confirmed by XRD. Figure 12.7 summarizes the results of this investigation

for different heat treatment temperatures (Fig. 12.7(a)) and time (Fig. 12.7 (b)) of a SiO_2 film containing 10 at% of InSb deposited on a Si substrate. The XRD spectra show that the nanocrystals have a cubic zinc blende structure similar to that of bulk InSb. Diffraction from the (111) plane at $\sim 24^\circ$, the (220) plane at $\sim 40^\circ$, and from the (311) plane at $\sim 47.5^\circ$ are recorded. For clarity the spectra have been translated along the intensity axis. The background levels were originally the same.

In both figures the XRD spectrum for a polycrystalline InSb deposited by RF magnetron sputtering on a Si substrate is also shown and has been scaled down to better see the spectra from the nanocrystals. The position of the (111) plane at $\sim 23.7^\circ$ corresponds well with the bulk value (23.79°) [115] and is used as a reference and referred to as bulk in the XRD spectra presented in this section. In the nanocrystals XRD spectra, the diffraction from the (111) plane is at a larger angle than expected for bulk InSb, which means that the planar distances of the nanocrystals are somewhat smaller than for the bulk crystal. This indicates that the nanocrystals are exposed to a compressive stress. Futhermore, the position of the (111) plane is constant for different heat treatment temperatures, times, and atmospheres[3], which suggests that the compressive stress on the nanocrystals originates from the SiO_2 matrix.

As introduced in section 11.1.1, the lattice constant can be evaluated from the position of the diffraction from the different planes. It is found to be 6.37 ± 0.01 Å while it is 6.48 Å for bulk InSb [116]. It is also possible to estimate an equivalent hydrostatic pressure P from the fractional change in the volume of the unit cell ($\delta V / V$) and the elastic stiffness constants of bulk InSb ($C_{11} = 0.672 \times 10^{11}$ Pa, $C_{12} = 0.367 \times 10^{11}$ Pa) [117]:

$$P = -\frac{\delta V}{3V}(C_{11} + 2C_{12}). \tag{12.1}$$

In this case, an equivalent hydrostatic pressure P as high as ~ 19 kbar is estimated[4]. It is interesting to note that no compressive stress was measured by XRD for the nanocrystals formed with a 6 at% concentration of InSb, which indicates that the initial content of the film strongly influences the stress on the nanocrystals.

It has also been seen that crystals are formed at the surface of the film as shown in Fig. 12.8, which were found to be In by energy dispersive

[3] The same shift in the position of the (111) plane was measured for a SiO_2 film containing 10 at% of InSb RTA heat treated at 900°C for 120 s under vacuum.

[4] An equivalent hydrostatic pressure of ~ 24 kbar is found when using the (220) and (311) planes.

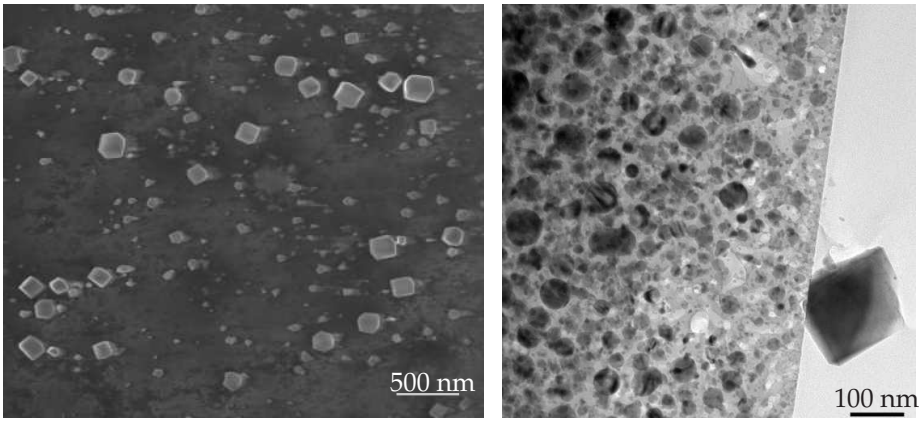

(a) (b)

Figure 12.8: (a) SEM and (b) TEM images of the surface of a SiO_2 film containing 10 at% of InSb, heat treated at 950°C for 60 s under a constant flow of N_2.

measurements [110]. This is also confirmed by XRD. The spectra presented in Fig. 12.7 show a small peak at 33.3° ($d = 2.69$ Å) which could be from In crystals ($d_{101} = 2.7165$ Å from [115]), while the two small peaks at 30.5° ($d = 2.92$ Å) and 35.5° ($d = 2.53$ Å), correspond very well to diffraction from the (222) and (400) planes of the cubic structure of In_2O_3 ($d_{222} = 2.921$ Å and $d_{400} = 2.529$ Å from [115]). This indicates that the pile up of material at the surface of the film shown in Fig. 12.5 is likely to be In. In order to limit the formation of In_2O_3 in the films[5], the samples should be kept in a dry environment, since the oxidation of In is most likely due to the diffusion of water in the films. Another solution would be to deposit a capping layer on the films, which would act as a diffusion barrier for the water molecules.

In summary, nanocrystals of InSb embedded in SiO_2 can be formed by post deposition RTA heat treatment at temperatures ranging from 800°C to 1000°C for 60 s to 480 s under a constant flow of N_2 and under vacuum. The InSb nanocrystals average diameter can be tuned by changing the initial concentration of InSb in the SiO_2 film, from 6 at% to 10 at% of InSb, or by changing the time, the atmosphere, and the temperature of the heat treatment. Futhermore, XRD investigations showed that the nanocrystals have an InSb cubic zinc-blende structure and that they are

[5]Dark field imaging in the TEM showed the presence of In_2O_3 in the films.

exposed to a compressive stress, which is independent of the heat treatment conditions, but strongly dependent on the concentration of InSb in the SiO_2 film. An equivalent hydrostatic pressure as high as $\sim$19 kbar was estimated for the highest concentration sample. The SiO_2 films containing InSb should be kept in a dry atmosphere after deposition in order to avoid the formation of In_2O_3 crystals in the films. Finally, it is interesting to note that the InSb nanocrystals formed that have been presented in this section have the theoretically calculated size to show quantum confinement. While no photoluminescence was detected, absorption was measured and will be presented in the next section.

12.1.3 Absorption from InSb nanocrystals in SiO_2

According to the calculations presented in chapter 9 and the results presented by Zhu *et al.* [94], the nanocrystals of InSb presented in the last section should exhibit quantum confinement, i.e. their photoluminescence and their absorption edge should be at a higher energy with respect to the bulk. Preliminary results for the absorption of InSb nanocrystals embedded in SiO_2 will be presented in this section.

SiO_2 films containing 6 at% (Sample 1) and 10 at% (Sample 2) of InSb were deposited on a quartz substrate. These films were RTA heat treated at 900°C for 120 s under a constant flow of N_2. The corresponding average crystal diameters based on the results presented in the last section are 19.8 ± 0.3 nm for Sample 1 and 22.6 ± 0.7 nm for Sample 2. The presence of the nanocrystals was verified by XRD measurements. The substrates were dimpled on the back side to ensure a substrate thickness variation over the probed area sufficient to suppress multiple interference in the quartz substrate.

The optical transmission of the samples was measured using a 1000M Jobin Yvon spectrometer fitted with InGaAs and Si detectors. The light source was a tungsten-halogen lamp. Due to the different wavelength sensitivity of the detectors and the spectrum of the lamp, the optical transmission spectra are recorded in two scans. The Si detector together with a low pass filter, having a cutoff at 530 nm, are used to measure from 560 nm (2.2 eV) up to 1060 nm, while the InGaAs detector in combination with a low pass filter with a cutoff at 850 nm are used to measure from 850 nm up to 1600 nm (0.78 eV). The large overlap between the two scans is used to concatenate the spectra. In both cases, the lamp spectrum is recorded and serves as reference for the calculation of the absorbance.

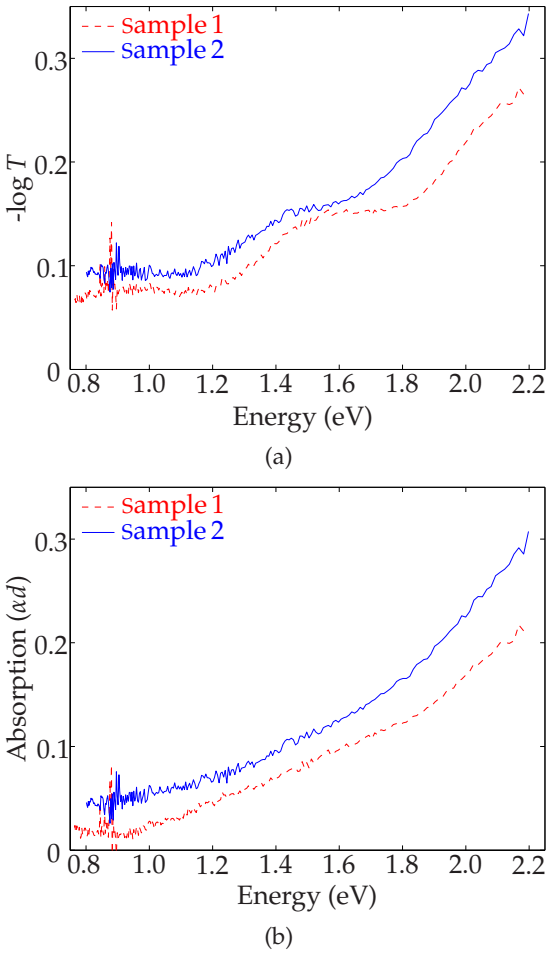

Figure 12.9: Absorbance spectra of InSb nanocrystals embedded in SiO_2 for two different initial concentrations giving two different size distributions for the nanocrystals.

The absorbance of the films is obtained with the following equation:

$$A = -\log \frac{I}{I_o} = -\log T \tag{12.2}$$

where I is the intensity of the light transmitted through the sample, I_o is the intensity of the light before entering the sample, and T is the transmittance. Figure 12.9(a) shows the absorbance of the two samples as a function of the energy of the light. For this energy range, an increase of

the absorbance with the energy of the light is clearly seen. The presence of water in the laboratory is reflected in the spectra at 0.9 eV. Optical interference features in the absorbance spectra are also observed, these are caused by the refractive index contrast between the deposited SiO_2 film containing InSb nanocrystals and the quartz substrate. Such experimental artifacts have previously been assigned to features related to optical transitions in nanocrystals [90, 118].

These oscillation features can be removed from the spectra by applying a recursive simulation of the films [119]. Some assumptions are made for the multiple interference simulation. First, no absorption results from the transmission of light in the quartz substrate. Based on experimental facts, multiple interferences occur mainly in the SiO_2 film containing the nanocrystals. Therefore, multiple interference is set to occur only in the SiO_2 film in the simulation. The effective transmission coefficient of light travelling from the air to the SiO_2 film, and finally through the quartz, at normal incidence is then given by:

$$\tau = \frac{\tau_{af}\tau_{fq}\tau_{qa}e^{i\beta/2}e^{-\alpha d/2}}{1+\rho_{af}\rho_{fq}e^{i\beta}e^{-\alpha d}} \tag{12.3}$$

where τ_{ij} and ρ_{ij} are the transmission and reflection coefficients from material i to material j, and a, f, and q correspond to the air layer, the SiO_2 film layer, and the quartz layer respectively. β is the phase change of the light going back and forth through the film once, d is the thickness of the SiO_2 film, and α is the absorption coefficient, which is related to the imaginary part of the refractive index of the SiO_2 film. In general the transmission and reflection coefficients are complex due to the imaginary part of the refractive index, which in turn is related to the absorbance. The transmittance T can be obtained by $T = \tau^*\tau$, where * denotes the complex conjugate. The logarithm of the transmittance is then given by:

$$\begin{aligned} -\log T &= -\log(\tau^*\tau) && (12.4)\\ &= \alpha d \log e + \text{transmission term} + \text{oscillation term} && (12.5)\end{aligned}$$

where αd expresses the total absorption from the film.

The modelled transmittance is adjusted by changing the optical thickness nd of the SiO_2 film, where n is the real part of the refractive index, until it matches the oscillations in the experimental spectrum. The oscillations introduced by the multiple interferences in the SiO_2 film can be

removed from the spectrum using the analytical expression for the transmittance.

Figure 12.9(b) shows the total absorption (αd) spectra for the two samples for which the oscillations were removed. An optical thickness of 1008 nm for Sample 1 and 1088 nm for Sample 2 was found with the simulation. First of all, as opposed to the results presented by Zhu *et al.* [94], no size dependency of the absorption can be seen from the spectra. Secondly, the two spectra happen to be linearly correlated, i.e. a linear transformation can be found which renders the two spectra identical within experimental error. This indicates that the absorption seen in these samples is most likely to be due to a defect in the SiO_2 which increases with the amount of InSb in the film.

12.2 Melting and solidification of InSb nanocrystals in SiO_2

The melting and solidification of solids on the nanometer scale have been studied for a century on a broad range of materials [120–122]. The scaling of crystals to the nanometer regime does not only influence their electronic properties, as introduced in chapter 9, but also their melting and solidification behaviour. This is interesting in itself and could also be of interest, for example, for the electronic industry where materials are pushed to the limit in size, sometimes reaching high temperatures.

The melting point of nanoclusters or nanocrystals is thermodynamically predicted to decrease with decreasing size [122–124]. The difference in the melting point of spherical nanocrystals with respect to the bulk is given by [124]:

$$T_m^{\infty} - T_m^{nc} = \frac{2T_m^{\infty}}{\rho_s r L_v}\left(\sigma_{sv} - \sigma_{lv}\left(\frac{\rho_s}{\rho_l}\right)^{2/3}\right) \tag{12.6}$$

where T_m^{∞} is the bulk melting point, T_m^{nc} is the nanocrystals melting point, ρ_s (ρ_l) is the number density (V/N) of the solid (liquid) phase, r is the nanocrystals radius, L_v is the latent heat of fusion per particle, and σ_{sv} (σ_{lv}) is the energy of the solid-vapor (liquid-vapor) interface. The reduction of the melting point has been observed for nanoclusters or nanocrystals of several materials [123,125]. In this section, the opposite behaviour, namely the superheating of InSb nanocrystals observed experimentally, will be presented. Details of the sample, the experiment performed, and

the results obtained will be followed by a theoretical model of the phenomenon observed.

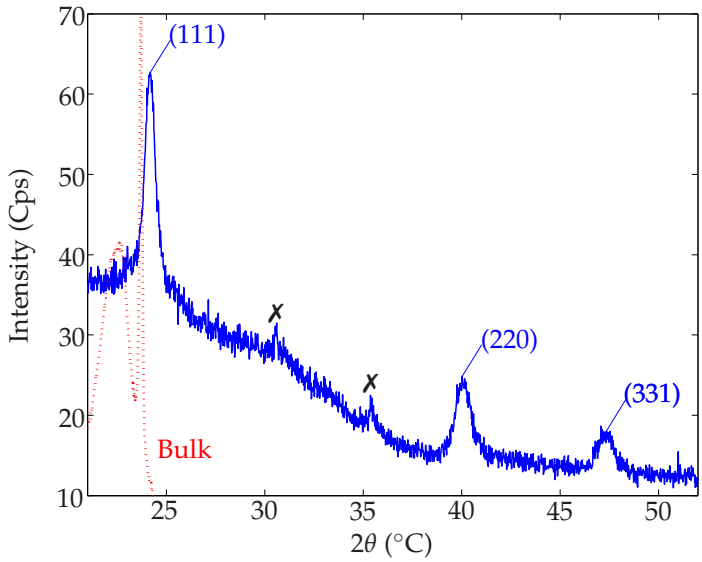

Figure 12.10: X-ray diffractogram of InSb nanocrystals embedded in SiO_2. The red-dotted curve corresponds to bulk InSb and has been divided by 10 for comparison.

The sample studied was a 600 nm thick randomly sputtered SiO_2 film containing 10 at% of InSb deposited on a Si substrate. A 1 cm^2 piece of the sample produced was subsequently heat treated at 900°C for 120 s in an N_2 atmosphere by RTA.

The sample was characterised first with XRD in order to obtain the crystal structure of the nanocrystals and their strain state. Figure 12.10 shows an XRD spectrum of the sample and for bulk InSb. The crystalline structure of InSb is evident from the three diffraction peaks corresponding to the (111), (220), and (331) planes as indicated on the figure. The XRD spectrum shows that the nanocrystals have a cubic zinc blende structure similar to that of bulk InSb and are exposed to a compressive stress. As introduced in the previous section, an equivalent hydrostatic pressure P as high as ∼19 kbar is estimated. The two additional diffraction peaks marked with a ✗ on Fig. 12.10 correspond to nanocrystals of In_2O_3 formed in the films (see section 12.1.2).

TEM was also employed to gain more information on the nanocrystals. A cross-sectional TEM sample was produced in order to obtain the

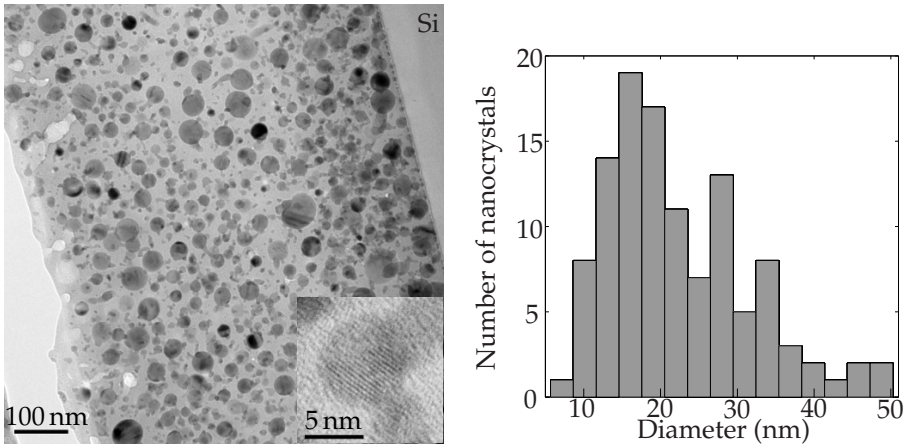

(a) (b)

Figure 12.11: (a) Cross-section TEM image of SiO_2 thin films containing InSb nanocrystals. The inset shows a high resolution TEM image of a 8 nm InSb nanocrystal. (b) Histogram of the size distribution obtained from (a).

size distribution of the nanocrystals throughout the films. Figure 12.11(a) shows a cross-section bright-field TEM image of the heat-treated films, while the inset shows a high-resolution TEM image of a 8 nm nanocrystal of InSb. From the cross-section TEM image, the size distribution was obtained, and is shown in Fig. 12.11(b). The mean diameter was found to be 22.5 nm with a standard deviation of 9.3 nm.

The melting and solidification of the nanocrystals were measured by *in-situ* heating and cooling of a sample in a TEM and recording the diffraction pattern of the nanocrystals at different temperatures. The sample used was a planar view TEM sample onto which carbon was deposited in order to avoid charging effects. It was placed in a heating stage and its temperature measured with an accuracy of $\pm 1^{\circ}C$. A low electron beam intensity was used in order to prevent additional heating of the sample. The total area probed by the electron beam was of about 40 μm^2. The melting curve was recorded from room temperature up to 713°C in steps of 20°C, with a time interval of 8 min between each measurement. The solidification curve was measured in a similar way by cooling the sample from 713°C to room temperature. The procedure was repeated with three different samples, and all gave the same results.

The diffraction patterns, recorded by the CCD camera, were integrated

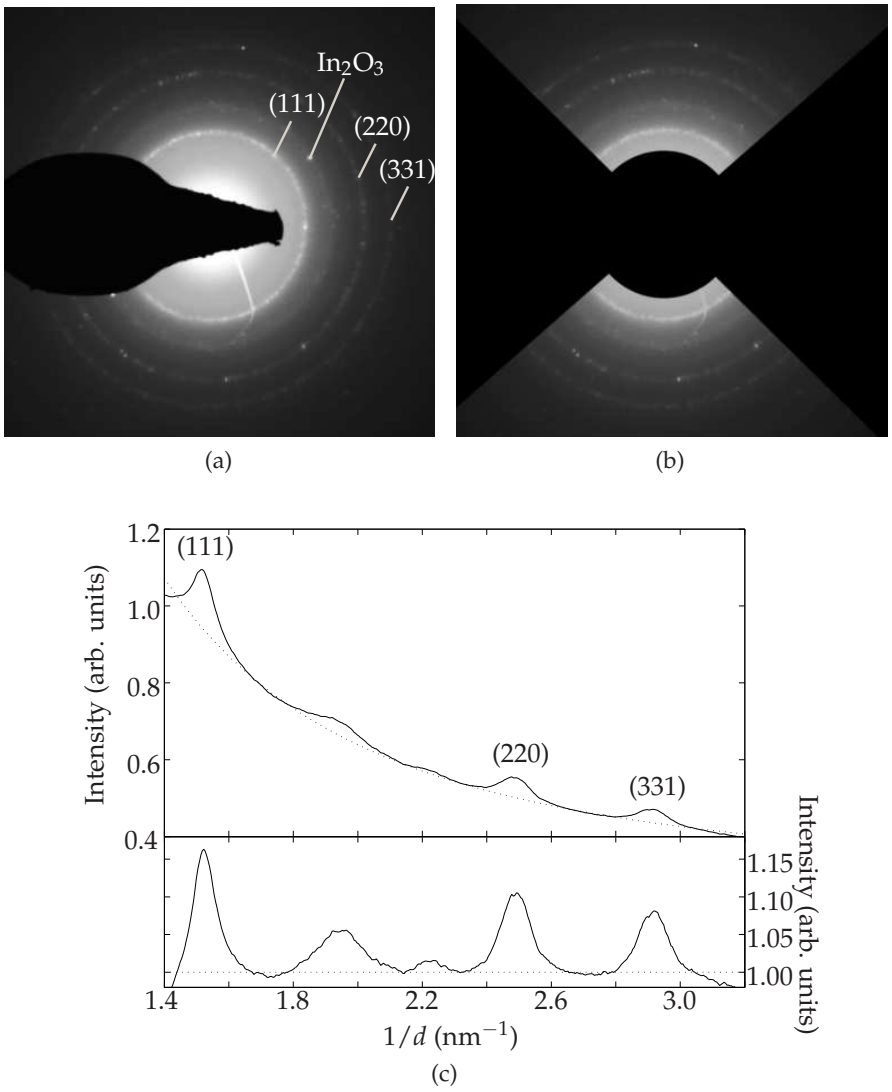

Figure 12.12: (a) A diffraction pattern from a planar view sample containing InSb nanocrystals. (b) The masked image to avoid inhomogeneities introduced by the beam stopper. (c) Circumferential integration (plain curve), and the background (dashed curve), fitted with a $y(x) = x^{-1}$ function. The bottom curve is obtained after normalisation with respect to the background.

circumferentially about the center of the diffraction rings in order to get the total diffracted intensity from the nanocrystals as a function of the temperature. The procedure to process the data is illustrated in Fig. 12.12. Firstly the center of the diffraction pattern must be found, then, the pattern is made symmetric by completely masking the beam stopper (Fig. 12.12(b))[6]. The next step is to perform the circumferential integration, which gives the black plain curve in the top of Fig. 12.12(c). Since the diffraction patterns are not all taken at the exact same place and with the same collimation, the background is not constant in all diffraction images. It is therefore needed to normalise the integrated diffracted intensity with respect to the background[7]. It has been found that a $y(x) = x^{-1}$ function models very well the background of the integrated intensity as shown by the dotted black curve in the top of Fig. 12.12(c). The integrated diffracted intensity is finally normalised with respect to the background, which gives the bottom curve in Fig. 12.12(c). This procedure is repeated for all the diffraction patterns.

Figure 12.13 shows the intensity of the (111) (●) and (220) (▲) diffraction rings as a function of the temperature for InSb nanocrystals embedded in SiO_2. The melting of the nanocrystals starts at 530°C, which is about the melting point of bulk InSb (527°C), and stops at 670°C, while solidification takes place between 540°C and 400°C. The hysteresis loop centered at the bulk melting point is of about 100°C, which corresponds to 19% of the bulk melting point. The progressive melting and solidification observed are believed to be due to the wide size distribution presented in Fig. 12.11. Furthermore, the position of the diffraction rings is the same before and after melting, which indicates that the nanocrystals are exposed to the same compressive stress upon melting. The number of nanocrystals at the end of the experiment is about 30% of the starting amount. It is likely that material at the surface starts to evaporate at temperatures higher than 600°C since the decomposition temperature of InSb is in the range 630-680°C [126]. The solidification curve has been normalised to obtain the temperature difference between the melting and solidification curves. The curvature of the solidification curve is the same as the melting one, which suggests that the behaviour observed is from the same size distribution.

Two different stability tests were done in order to make sure that

[6]The pie-shaped mask is built-in the Gatan software, which is used in the first part of the data processing. More intensity could be achieved by removing the right half of the pie-shaped mask, but it is unfortunately not available with this software.

[7]The diffracted intensity does not scale with the background level.

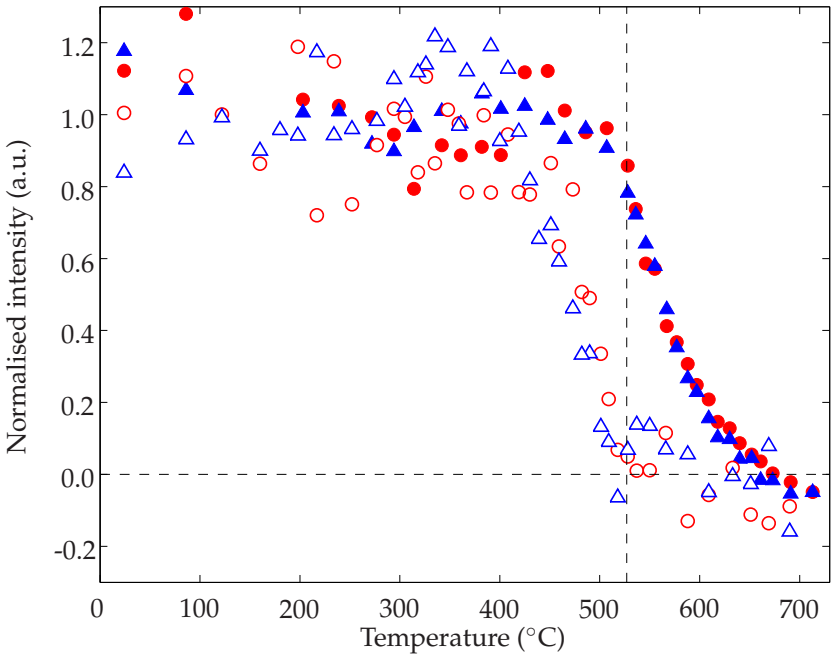

Figure 12.13: Melting (filled symbols: ● and ▲) and solidification (open symbols: ❍ and △) curves for InSb nanocrystals embedded in SiO_2. The (111) (●) and (220) (▲) peaks are followed as a function of the temperature. The vertical dashed line indicates the bulk melting temperature $T = 527°C$.

the results presented in Fig. 12.13 are not artifacts of the measurement technique. First, the melting curve of bulk InSb was measured in the same way as the one presented above. A ∼100 nm thick film of InSb was deposited by RF magnetron sputtering on a Si substrate and a planar view TEM sample of it was prepared. The results are presented in Fig. 12.14(a). The diffracted intensity from the (111) (●) and (220) (▲) planes are recorded as a function of the temperature. As expected for bulk InSb, the melting is completed at 527°C. It is interesting to notice that the diffracted intensity becomes higher at 340°C, which corresponds to the crystallisation of InSb. Futhermore, the progressive melting observed, starting at ∼450°C, is most likely due to the finite thickness of the planar sample. Since the thickness of the film investigated in the TEM is a few tens of nanometer, surface effects are believed to play a role in

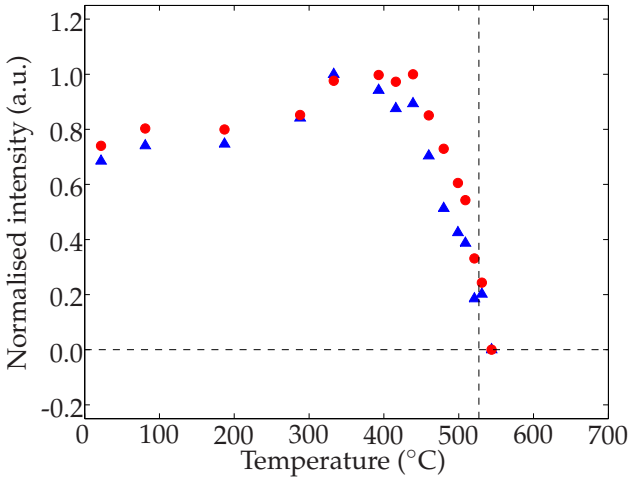

(a)

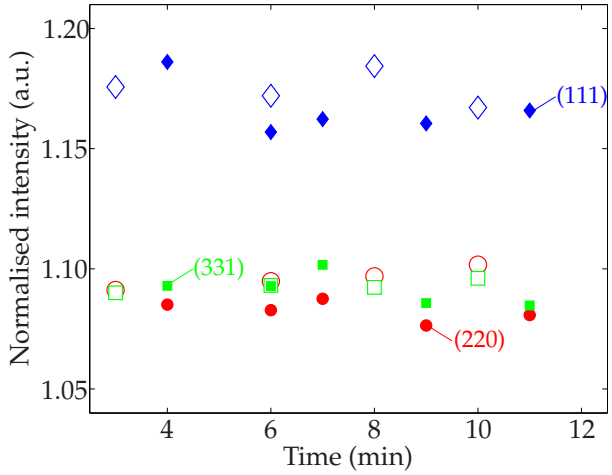

(b)

Figure 12.14: (a) Melting of a RF sputtered film of InSb followed in the TEM. The vertical dashed line indicates the bulk melting temperature $T = 527°C$. (b) Diffracted intensity from the (111) (◆), (220) (●), and (331) (■) planes of InSb nanocrystals as a function of time for two different temperatures: at 522°C (open symbols) and at 543°C (filled symbols).

the melting. Nevertheless, the melting occurs at the same temperature as expected for the bulk. The solidification curve could not be recorded since upon melting the material formed agglomerates, which were too thick and not transparent to electrons anymore.

Secondly, the stability of the diffracted intensity as a function of time was measured. Fig. 12.14(b) shows the results of this investigation. The diffracted intensity from the (111) (◆), (220) (●), and (331) (■) planes of InSb nanocrystals was recorded as a function of time at two different temperatures: 522°C (open symbols) and 543°C (filled symbols). At both temperatures, the diffracted intensity recorded is stable, which means that a delay of 8 min between the measurements is sufficient.

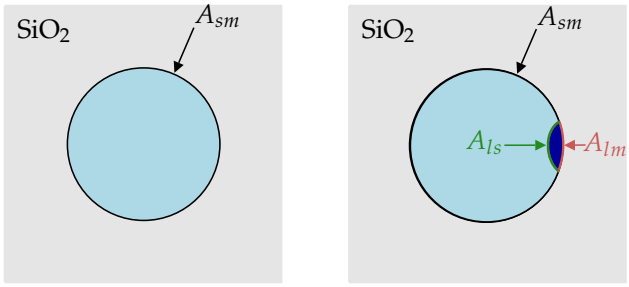

(a) G_s (b) G_{s+l}

Figure 12.15: Illustration of a (a) solid nanocrystal embedded in SiO_2 and (b) a solid nanocrystal with premelt at the interface.

In order to understand the phenomenon of superheating and undercooling of nanocrystals, a size-dependency kinetic approach for melting has recently been proposed for embedded Ge nanocrystals by Xu *et al.* [127]. Instead of looking at the difference in free energy between a solid nanocrystal and a melted one, the transition from one state to the other is developed. Consider the case of melting where a small part of the nanocrystal premelts at the interface as illustrated in Fig. 12.15. The difference in Gibbs free energy between the case where the premelting occurs (G_{s+l}) and the case of a solid nanocrystal (G_s) is given by:

$$\begin{aligned}\Delta G =& G_{s+l} - G_s \\ =& N\chi(h_l^b - h_s^b) - TN\chi(s_l^b - s_s^b) \\ &+ A_{sl}\sigma_{sl} + A_{lm}(\sigma_{lm} - \sigma_{sm})\end{aligned} \tag{12.7}$$

where N is the total number of atoms in the nanocrystal, χ is the volume

fraction of the liquid phase, h_l^B (h_s^B) is the bulk enthalpy of the liquid (solid) phase per atom, s_l^B (s_s^B) is the bulk entropy of the liquid (solid) phase per atom, and A_{ij} and σ_{ij} are the area and interface energy of the interfaces respectively. The interface areas are dependent on χ since they depend on the volume of the premelt. s, l, and m stand for solid, liquid, and matrix respectively. At a temperature close to the bulk melting point, the difference in entropy between the two phases becomes $\Delta s = L_v/T_m^\infty$. In the same way, the difference in enthalpy ($h_l^b - h_s^b$) is the latent heat of fusion at the melting point. For $T \geq T_m^\infty$, Eq. 12.7 reduces to:

$$\Delta G = N\chi L_v \left(1 - \frac{T}{T_m^\infty}\right) + A_{sl}(\chi)\sigma_{sl} + A_{lm}(\chi)(\sigma_{lm} - \sigma_{sm}) \qquad (12.8)$$

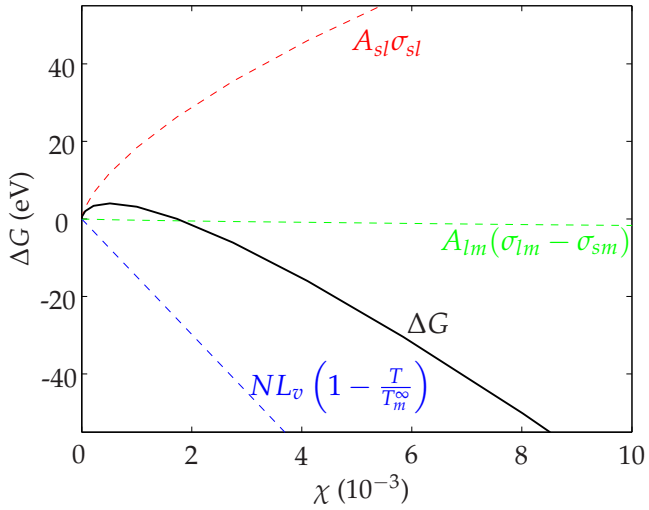

Figure 12.16: Difference in Gibbs free energy as a function of the volume fraction of liquid χ at the bulk melting point.

This equation is illustrated in Fig. 12.16 as a function of the volume fraction of the premelt at the bulk melting temperature, in order to appreciate the importance of all terms. The first thing to notice is that there is an energy barrier to melting. The barrier arises from the creation of the solid-liquid interface sl. In order for melting to occur, the energy related to the creation of the interface sl must be as low as possible. This introduces an energically favourable pathway for the melting of nanocrystals as illustrated in Fig. 12.17 and introduced in [127]. The pathway corresponding to the lowest energy barrier will be the one for which A_{sl} is

minimum for a given volume. The computation of this pathway is a variational problem. In this work, the problem was treated by assuming that the smallest area for a given volume will have a spherical curvature, and was treated using Lagrange multipliers [128]. The optimised pathway obtained was used to simulate the results presented in [127] for Ge nanocrystals and a similar energy barrier was found[8].

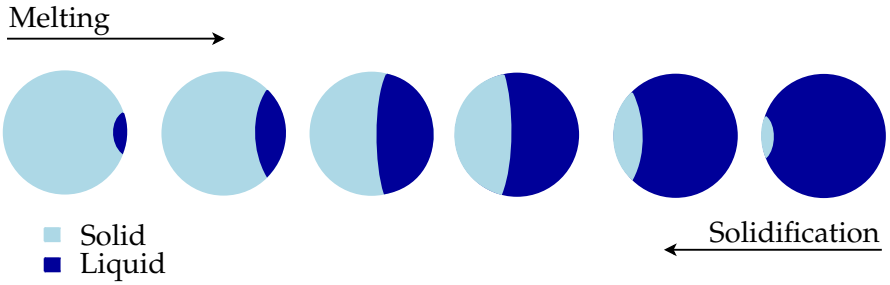

Figure 12.17: Pathway for the melting and solidification of nanocrystals in SiO_2 obtained from the minimisation of A_{sl}.

In order to take into account the compressive stress on the nanocrystals present in the system of InSb nanocrystals in SiO_2, a modification to Eq. 12.8 was done. The melting temperature of the bulk is set to be a function of the pressure. This dependency is known for bulk InSb [129]. Assuming only the bulk melting temperature being a function of pressure, Eq. 12.8 becomes:

$$\Delta G = N\chi L_v \left(1 - \frac{T}{T_m^{\infty}(P)}\right) + A_{sl}(\chi)\sigma_{sl} + A_{lm}(\chi)(\sigma_{lm} - \sigma_{sm}) \qquad (12.9)$$

A similar expression can be found for solidification, where the pathway for solidification is the same as for melting due to the symmetry of the problem.

By using the method of activated complex theory [130], commonly used to simulate kinetics of chemical reactions, the melting and solidification behaviour of InSb nanocrystals in SiO_2 was calculated and the interface energies of this system were obtained. According to this theory, the rate at which the melting will occur, that is the rate at which the

[8] In the present work 3.35 eV at 1125°C was found, while in [127] they found 3.91 eV at the same temperature.

transition from configuration G_s to configuration G_{s+l} will occur, is given by:

$$\nu = \kappa K \tag{12.10}$$

where κ is the transmission coefficient, normally assumed to be 1, and

$$K = \frac{k_B T}{h} \exp\left(\frac{-\Delta G_{max}}{k_B T}\right) \tag{12.11}$$

where k_B is Boltzmann's constant, h is Planck's constant, and ΔG_{max} is the energy barrier. Assuming that the number of InSb molecules in the solid phase in the sample is directly proportional to the diffracted intensity, the rate ν can also be expressed in terms of the diffracted intensity I as:

$$\frac{\mathrm{d}I}{\mathrm{d}t} = -\nu I(t) \tag{12.12}$$

where t is time. In this way, an expression for the diffracted intensity as a function of the temperature can be obtained:

$$\ln I = -\delta t \frac{k_B T}{h} e^{-\Delta G_{max}/k_B T} \tag{12.13}$$

where δt is the delay time allowing for the transition to occur.

This model was applied to the nanocrystals of InSb in SiO_2 assuming a pressure of 19 kbar, thus reducing the bulk melting by 150°C. δt is set to 8 min[9], which is the time interval between the change in temperature and the actual measurement. The values for the interface energies found in [131] were used as a starting point in the model. The latent heat of fusion is set to $L_v = 4.23 \times 10^{-20}$ J/molecule [132]. The calculation results for a nanocrystal having a radius of 11 nm are shown in Fig. 12.18 together with the experimental data for comparison. The interface energies were adjusted so that simulated melting and solidification occur at the same temperature as the those measured. They were found to be $\sigma_{sl} = 0.18$ N/m, and $\sigma_{sm} - \sigma_{lm} = 0.02$ N/m. The energy barrier to melting is 2.47 eV at $T = 567$°C, while it is 2.40 eV at $T = 478$°C for solidification. In the case of the calculation, the temperature of melting and solidification are well defined compared to the experimental results. However, the shape of the curves is different due to the fact that the size distribution of the nanocrystals was not taken into account in the calculation. Furthermore, the Debye-Waller factor [96] introducing a decrease

[9] 8 min is an upper limit estimate for the time delay.

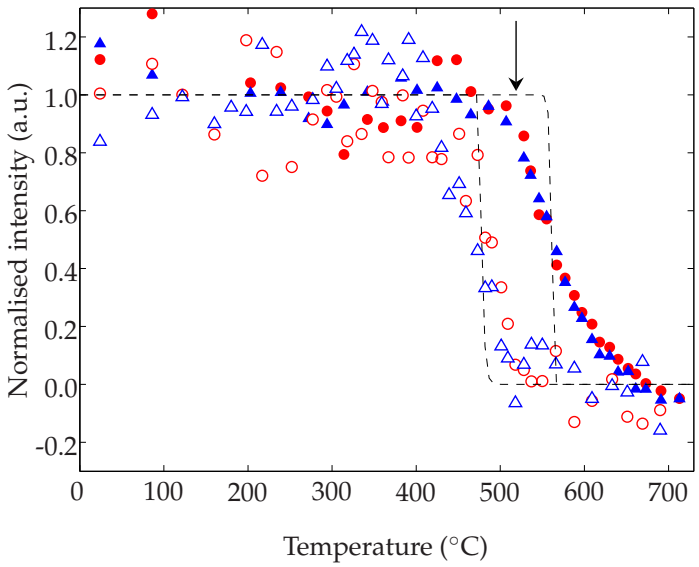

Figure 12.18: Calculation (dashed black curves) of the melting and solidification curves for InSb nanocrystals embedded in SiO_2. The experimental results are also shown for comparison (see Fig. 12.13 for more details). The arrow indicates the bulk melting temperature $T = 527°C$.

in the diffracted intensity due to the thermal motion of the atoms with the temperature was also ignored. These two factors would contribute to a broadening of the melting and solidification curves.

The energy barrier to melting at $T = 567°C$ was calculated as a function of the radius r of a InSb nanocrystal with the interface energies mentioned above. The results are presented in Fig. 12.19. Apart from the variations in the energy barrier for large radius values due to the resolution in the volume fraction becoming cruder as the size increases, the energy barrier seems to be constant for a radius higher than 8 nm. The barrier would still be present in a bulk crystal. This inconsistency can be explained by the lack of an entropy term in the model related to the different configurations the premelt can take at the $InSb/SiO_2$ interface, as illustrated schematically in Fig. 12.20. If, in a first approximation, the number of configurations possible correspond to the total area of the nanocrystal divided by the area at the interface A_{lm}, the difference in

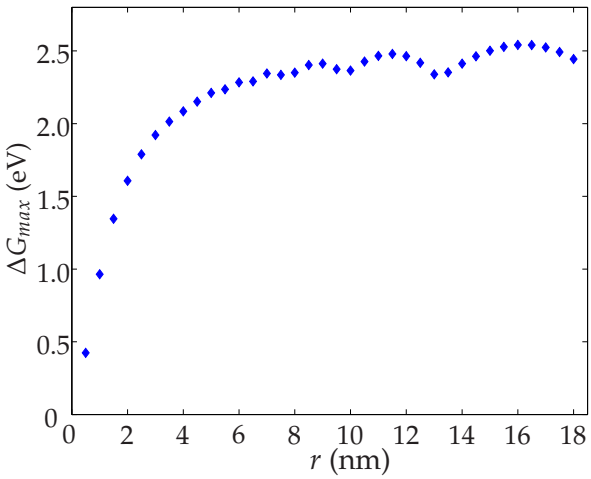

Figure 12.19: Energy barrier as a function of the nanocrystal radius at $T = 567°C$.

Figure 12.20: Illustration of the different configurations of the premelt, which correspond to an increase in entropy.

Gibbs free energy becomes:

$$\Delta G^* = \Delta G - T\Delta S^* \tag{12.14}$$

where

$$\Delta S^* = k_B \ln \frac{4\pi r^2}{A_{lm}}. \tag{12.15}$$

This extra entropy term increases with the radius of the nanocrystal. Applied to a nanocrystal of 11 nm in radius, ΔS^* would reduce the energy barrier by 0.4 eV at $T = 567°C$. For a macroscopic crystal of 1 cm in radius, the reduction of the energy barrier becomes $\sim$2.4 eV at the same temperature. This first approximation is most likely to underestimate

the number of configurations possible. A more accurate approach is to consider that every atomic site at the interface corresponds to a configuration, since by moving the center of the A_{lm} interface by one atom, different atoms of the interface will be contained in the premelt. The entropy would be in this case:

$$\Delta S^{**} = k_B \ln(4\pi r^2 n). \tag{12.16}$$

where n is the surface atomic density. As an example, if $n = 6.74 \times 10^{18}$ atoms/m^2 for InSb (110) [133] and $r = 11$ nm, $T\Delta S^{**} = 0.67$ eV and for $r = 1$ cm, $T\Delta S^{**} = 2.65$ eV. By introducing this entropy term in Eq. 12.13, an solid-liquid interface energy of $\sigma_{sl} = 0.197$ N/m is found, while the difference between σ_{lm} and σ_{sm} remains constant. Thus, the determination of the interface energies can be achieved more accurately by including the extra entropy term in the model and the barrier disappears for macroscopic systems.

In summary, the superheating and undercooling of InSb nanocrystals embedded in SiO_2 observed experimentally can be understood by introducing a kinetic pathway for melting and solidification. The processes can be modelled by determining the energy barrier to melting and solidification and by applying the formalism of activated complex theory. In this way, the interface energies of the system could be found and the analytical model could reproduced the experimental results.

12.3 InSb nanocrystals in a multilayer configuration

In order to study the physical properties of nanocrystals, which are strongly influenced by their size, a more defined size distribution of nanocrystals is desired. The deposition in a multilayer configuration, introduced by Tong *et al.* [134], is the technique chosen for this project since it is easily achieved by RF magnetron sputtering. It consists of depositing alternating layers of the material meant for nanocrystals and SiO_2. In this configuration, the size of the nanocrystals is related to the thickness of the layer of semiconductor material, which can be changed easily. The preliminary results obtained for the formation of InSb nanocrystals in a multilayer configuration will be presented in this section.

The multilayer films were deposited by alternating the sputtering of a SiO_2 and InSb target. In order to have an idea of the thickness of the deposited layers as a function of time, the deposition rate for both targets

was calibrated. Several multilayer samples, where the InSb layer thickness was varied from 2 nm up to 8 nm, were deposited on Si substrates. A SiO_2 layer of 15 nm was found to be an appropriate choice to limit inter-layer interactions. The Ar pressure and the RF power were kept constant for these investigations[10], and the temperature of the substrate was varied from room temperature up to 450°C. The samples were heat treated after deposition at various temperatures in a furnace for times ranging from 30 min to 120 min. RTA heat treatment was also tried with the parameters described in section 12.1, but in all these cases the formation of InSb nanocrystals could not be detected with XRD even though their expected size was large enough for the diffraction to be recorded.

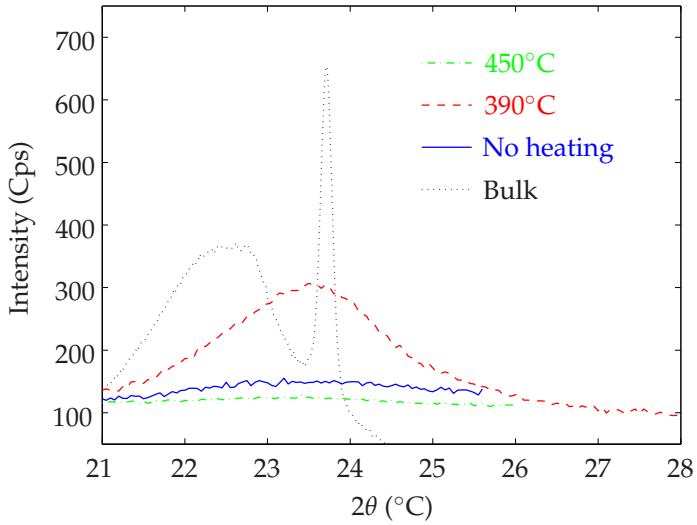

Figure 12.21: XRD spectra of multilayer samples before heat treatment. The diffraction from the (111) plane of InSb is present in the case where the substrate was heated to 390°C during the deposition (red dashed curve). No diffraction is recorded when the deposition is done at a higher temperature, 450°C (dot-dashed green curve), or at room temperature (plain blue curve).

The first conclusion drawn from multilayer film deposition is that the substrate temperature during deposition is an important parameter. Figure 12.21 shows a XRD spectrum of a film deposited without heating the

[10] See section 10.1.2 for the deposition parameters.

substrate (plain blue curve), one for which the substrate was heated at 390°C (red dashed curve) and one at 450°C (dot-dashed green curve). In all cases, the thickness of the InSb layers was 8 nm. Polycrystalline layers are formed when the substrate is heated at 390°C, but not at higher temperature (450°C) nor at room temperature. A film heated during deposition at 450°C has the typical colour of a SiO_2 film of the same thickness, indicating that InSb is not present in the film. The range of temperatures for which polycrystalline layers are formed is most likely to be restricted to 350-420°C, which corresponds to the crystallisation temperature of InSb seen in Fig. 12.14(a). The formation of the polycrystalline layers is important for the formation of nanocrystals. Without it, only diffusion of the species to the surface occurs when the films are heat treated after deposition. It is interesting to note that the polycrystalline layers do not exhibit the compressive stress discussed in section 12.1. In contrast, they are slightly relaxed with respect to the bulk (dotted black curve).

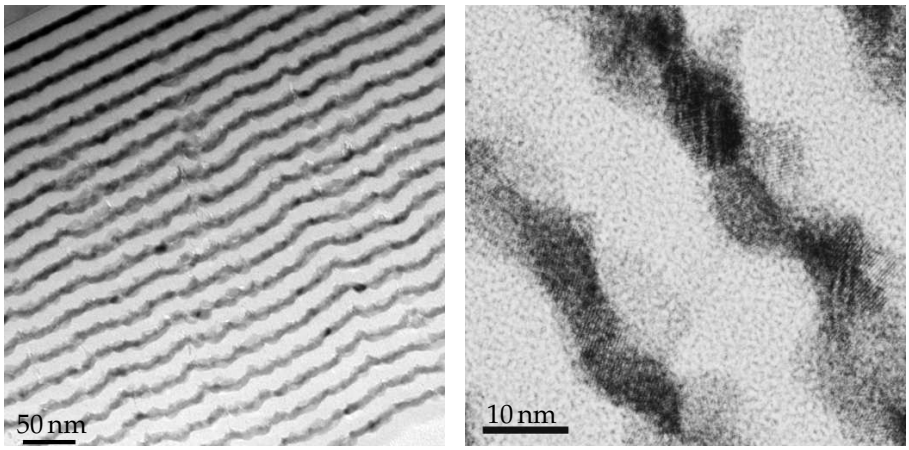

(a) (b)

Figure 12.22: (a) TEM image of a multilayer sample as deposited for which the Si substrate (top left corner) was heated to 390°C during the deposition. (b) HRTEM image showing the polycrystalline layer formed by heating the substrate during deposition.

The roughness of the layers increases with the number of layers deposited as seen in Fig. 12.22(a). This effect is due to atom shadowing occuring during sputtering deposition [135,136]. In this case, 21 layers of InSb 8 nm thick were deposited on a Si substrate heated at 390°C. Only

the first five layers from the substrate (top left corner) are planar. The crystallinity of the layers is seen in a HRTEM image (Fig. 12.22(b)), confirming the results obtained by XRD.

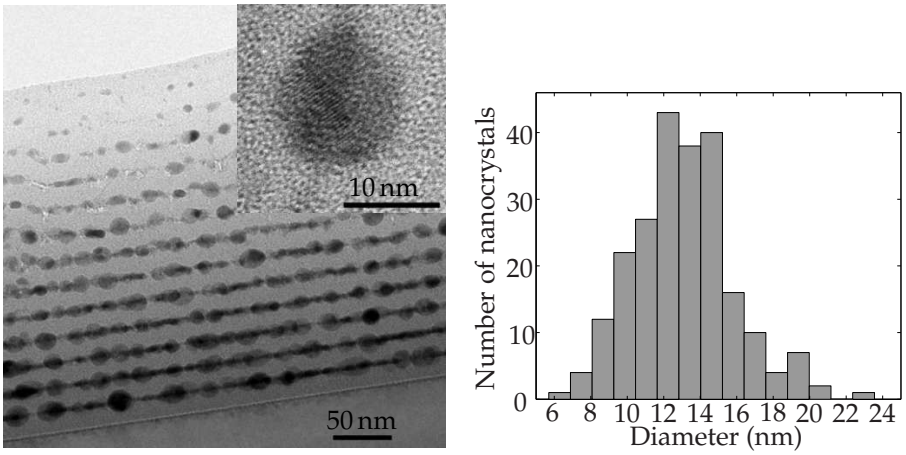

(a) (b)

Figure 12.23: (a) TEM image of a multilayer sample for which the Si substrate (bottom) was heated to 390°C during the deposition. Post deposition heat treatment was done in a furnace annealing at 500°C for two hours in a constant flow of N_2. The inset shows a HRTEM image of a 14 nm nanocrystal. (b) Size distribution obtained from the first nine layers from the substrate in (a).

Finally, there is a threshold in the InSb layer thickness for the formation of the nanocrystals to occur. When the layers of InSb are larger than 3 nm, partial formation of nanocrystals and diffusion of the species to the surface occur. The formation of nanocrystals arises when lowering the thickness as shown in Fig. 12.23. For this sample, 21 layers of InSb 3 nm thick were deposited on a Si substrate heated at 390°C. The film was heat treated in a furnace annealing at 500°C for two hours in a constant flow of N_2 after deposition. The inset of Fig. 12.23(a) shows a HRTEM image of a 14 nm nanocrystal. The size distribution of the nanocrystals in this sample was obtained from the first nine layers from the substrate and is shown in Fig. 12.23(b). The average diameter of the nanocrystals is 13.1 ± 0.2 nm. From Fig. 12.23(a), one can see that there is a limit on the number of layers to be deposited while heating the substrate during deposition. The top layers show a reduction of material, indicating an

enhancement of the diffusion to the surface, resulting in the formation of smaller nanocrystals in the top layers. Apart from the top layers, the size distribution is more defined than in the case of randomly distributed nanocrystals as expected for this configuration. These preliminary results indicate that the formation of nanocrystals of InSb of 13 nm or less in a multilayer configuration is possible, which is very interesting in order to study further the optical properties of InSb nanocrystals, and also their melting and solidification behaviour.

12.4 Summary

This chapter presented the experimental results concerning InSb nanocrystals in SiO_2. The synthesis of InSb nanocrystals was successfully achieved by deposition of SiO_2 films containing between 6 at% and 10 at% of InSb, and post deposition heat treatment by RTA at the temperature range 800-1000°C in a N_2 atmosphere or in vacuum. The melting and solidification of the nanocrystals was studied *in situ* in the TEM. Superheating and undercooling of the nanocrystals was observed and calculated using a kinetic approach combined with activated complex theory. Good agreement between the experimental data and the calculations was shown. Finally, preliminary results for the synthesis of InSb nanocrystals in SiO_2 in a multilayer configuration were presented. These results are promising. A more well defined size distribution would open the way to the study of the melting and solidification behaviour as a function of the size of the nanocrystals and also of their stress state, which could be compared to the model described in this chapter. Further study of the optical properties of InSb nanocrystals could also be made as a function of their size, but also as a function of temperature since the absorption and photoluminescence of bulk InSb are strongly dependent on temperature.

CHAPTER 13

Conclusion

Semiconductor nanocrystals present many interesting properties different from the bulk crystal. InSb nanocrystals are no exception. In order to learn more about these nanostructures and their properties, the quantum confinement effect, giving rise to the blue shift of the absorption and emission, has been introduced. A short review on InSb nanostructures was also included in order to put this work in perspective. A description of the preparation of InSb nanocrystals in SiO_2 was made, including RF magnetron sputtering and post deposition heat treatment in a furnace or by RTA. The formation of InSb nanocrystals was successfully achieved by post deposition RTA heat treatment in the temperature range 800-1000°C, in a N_2 atmosphere or in vacuum, of SiO_2 containing 6-10 at% of InSb. X-ray diffraction spectroscopy, transmission electron microscopy, and Rutherford back scattering spectrometry measurements were used in order to characterise the nanocrystals. More specifically, the melting and solidification behaviour of the nanocrystals were studied *in situ* in the TEM by recording the diffraction pattern as a function of temperature. A model based on a kinetic approach to melting and solidification combined with the formalism of activate complex theory was developped. Superheating and undercooling of InSb nanocrystals embedded in SiO_2 were both observed experimentally and calculated, which provided a measure of the interface energies of this system. Fi-

nally, preliminary results of the formation of InSb nanocrystals in SiO_2 in a multilayer configuration were presented. This configuration enables the formation of nanocrystals showing a narrower size distribution, thus nanocrystals having more defined size dependent properties. By obtaining a narrower size distribution, more well defined optical properties and the melting and solidification behaviour of InSb nanocrystals could be obtained and studied further as a function of their size.

CHAPTER 14

General conclusion and outlook

In the last few years there has been a shift towards "siliconising" photonics, since there is hope for the resolution of the problem of interconnection on a chip by using optics instead of electronics. The work presented in this thesis concerns two different subjects within the field of silicon photonics. The first part was related to the work made on 2D photonic crystals components, while the second part described the formation and characterisation of InSb nanocrystals.

The modeling of 2D photonic crystal components, using both plane wave expansion and finite-difference time-domain methods, was applied to various structures in order to understand the propagation and dispersion properties of photonic crystal waveguides. This study introduced one of the most interesting features, namely the phenomenon of slow light. The mapping of the field in this regime was utilised to optimise components for slow light, including in-coupling and 60° bends. The optimisation was made by using topology optimisation. Applied to photonic crystal structures, it consists of a free redistribution of material in a design domain in a way which maximises the transmission through the device for a given polarisation of light. The performance of in-coupling to slow-light was improved, giving a very short structure with a reduction of losses by up to 5 dB. The optimisation method was also applied to 60° bends and resulted in an improvement of the transmission of light

through the devices, both in the linear regime and the slow-light regime. As a final remark, these studies showed that photonic crystal waveguides are not the preferred solution for point-to-point transmission of light, which indicates that these structures are more likely to be used for their unique dispersion properties.

In the second part of this thesis, the focus was on InSb nanocrystals embedded in SiO_2. The quantum confinement effect is predicted to occur in InSb nanocrystals in the size range 2-22 nm in diameter, and should change the optical properties of InSb. The details of the experimental road followed to actually obtain nanocrystals of InSb, of 17-25 nm in diameter, in SiO_2 were presented. Optical absorption measurements for InSb nanocrystals were shown, but the spectra could not be correlated with the presence of the nanocrystals. However, the absorption and photoluminescence of bulk InSb are strongly temperature dependent, therefore, low temperature experiments may be a way to measure optical properties of these nanocrystals. The formation of InSb in a multilayer configuration was also discussed, and the preliminary results for multilayer samples showed a more well defined size distribution, paving the way for further study of the optical properties of InSb nanocrystal as a function of their size.

During this project, the nanocrystals formed were used to study the melting and solidification behaviour on the nanometer scale in a transmission electron microscope. As oppposed to previous theory in this field, both superheating and undercooling of InSb nanocrystals could be observed experimentally. The compressive stress measured on the nanocrystals was inserted into an analytical model, based on a kinetic approach to melting, and good agreement between the experimental observations and the calculations was found. In order to validate the model and for future work, it would be interesting to investigate the influence of the stress and size on melting and solidification of InSb nanocrystals embedded in SiO_2, and also other types of nanocrystals.

Bibliography

1. Cullis, A. G. and Canham, L. T. Visible light emission due to quantum size effects in highly porous crystalline silicon. *Nature* **353**(6342), 335–338 (1991).

2. Wilson, W. L., Szajowski, P. F., and Brus, L. E. Quantum comfinement in size-selected, surface-oxidized silicon nanocrystals. *Science* **262**, 1242–1244, November (1993).

3. Rong, N., Jones, R., Ansheng, L., Cohen, O., Hak, D., Fang, A., and Paniccia, M. A continuous-wave raman silicon laser. *Nature* **433**(7027), 725–728 (2004).

4. Xu, Q., Schmidt, B., Pradhan, S., and Lipson, M. All-optical slow-light on a photonic chip. *Nature* **435**(7040), 325–327 (2005).

5. Vlasov, Y. A. and McNab, S. J. Losses in single-mode silicon-on-insulator strip waveguides and bends. *Opt. Express* **12**(8), 1622–1631 (2004).

6. Bogaerts, W., Taillaert, D., Luyssaert, B., Dumon, P., Van Campenhout, J., Bienstman, P., Van Thourhout, D., Baets, R., Wiaux, V., and Beckx, S. Basic structures for photonic integrated circuits in silicon-on-insulator. *Opt. Express* **12**(8), 1583–1591 (2004).

7. Vlasov, Y. A., O'Boyle, M., Hamann, H. F., and McNab, S. J. Active control of slow light on a chip with photonic crystal waveguides. *Nature* **438**(8), 65–69 (2005).

8. Jacobsen, R. S., Andersen, K. N., Borel, P., Fage-Pedersen, J., Frandsen, L. H., Hansen, O., Kristensen, M., Lavrinenko, A., Moulin, G.,

Ou, H., Peucheret, C., Zsigri, B., and Bjarklev, A. Strained silicon as a new electro-optic material. *Nature* **441**, 199–202, May (2006).

9. Lu, Z. H., Lockwood, D. J., and Baribeau, J.-M. Quantum confinement and light emission in SiO_2/Si superlattices. *Nature* **378**, 258–260, November (1995).

10. Lodahl, P., van Driel, A. F., Nikolaev, I. S., Irman, A., Overgaag, K., Vanmaekelbergh, D., and Vos, W. L. Controlling the dynamics of spontaneous emission from quantum dots by photonic crystals. *Nature* **430**, 654–657 (2004).

11. Yablonovitch, E. Inhibited spontaneous emission in solid-state physics and electronics. *Phys. Rev. Lett.* **58**(20), 2059–2062, May (1987).

12. John, S. Strong localization of photons in certain disordered dielectric superlattices. *Phys. Rev. Lett.* **58**(23), 2486–2489, June (1987).

13. Johnson, S. G. Morpho deidamia photo taken at the butterfly garden in april 2004 in hunawihr, alsace, france. *Wikipedia GNU Free Documentation License* , http://en.wikipedia.org/wiki/Image:Hunawihr–morpho–butterfly.jpg (2004).

14. Korte, F., Koch, J., Serbin, J., Ovsianikov, A., and Chichkov, B. N. Three-dimensional nanostructuring with femtosecond laser pulses. *IEEE Trans. Nanotech.* **3**(4), 468–472 (2004).

15. Borel, P., Harpøth, A., Frandsen, L. H., Kristensen, M., Shi, P., Jensen, J. S., and Sigmund, O. Topology optimization and fabrication of photonic crystal structures. *Opt. Express* **12**(9), 1996–2001 (2004).

16. Têtu, A., Kristensen, M., Frandsen, L. H., Harpøth, A., Borel, P., Jensen, J. S., and Sigmund, O. Broadband topology-optimized photonic crystal components for both TE and TM polarizations. *Opt. Express* **13**(21), 8606–8611, October (2005).

17. Jacobsen, R. S., Lavrinenko, A., Frandsen, L. H., Peucheret, C., Zsigri, B., Moulin, G., Fage-Pedersen, J., and Borel, P. Direct experimental and numerical determination of extremely high group indices in photonic crystal waveguides. *Opt. Express* **13**(20), 7861–7870 (2005).

18. Joannopoulos, J. D., Meade, R. D., and Winn, J. N. *Photonic Crystals. Molding the Flow of Light*. Princeton University Press, (1975).

19. Johnson, S. G. and Joannopoulos, J. D. Mit photonic-bands, (2002). http://ab-initio.mit.edu/mpb/.

20. Frandsen, L. H. *Fabrication and Characterization of Photonic Bandgap Components*. Ph.D. thesis, Department for Communications, Optics & Materials, COM, Technical University of Denmark, (2006).

21. Taflove, A. *Advances in Computational Electrodynamics, The Finite Difference Time Domain Method*. Artech House Publischers, (1998).

22. Photon design. http://www.photond.com.

23. Ward, A. and Pendry, J. A program for calculating photonic band structures and green's functions using a non-orthogonal FDTD method. *Comp. Phys. Comm.* **112**(1), 23–41 (1998).

24. Ward, A. and Pendry, J. A program for calculating photonic band structures, Green's functions and transmission/reflection coefficients using a non-orthogonal FDTD method. *Comp. Phys. Comm.* **128**(3), 590–621 (2000).

25. Lavrinenko, A., Borel, P., Frandsen, L. H., Thorhauge, M., Harpøth, A., Kristensen, M., and Niemi, T. Comprehensive FDTD modelling of photonic crystal waveguide components. *Opt. Express* **12**(2), 234–248 (2004).

26. Cluzel, B., Gérard, D., Picard, E., Charvolin, T., Calvo, V., Hadjii, E., and de Fornel, F. Experimental demonstration of bloch mode parity change in photonic crystal waveguide. *Appl. Phys. Lett.* **85**(14), 2682–2684 (2004).

27. Borel, P. I., Frandsen, L. H., Harpøth, A., LEan, J. B., Liu, H., Kristensen, M., Bogaerts, W., Dumon, P., Baets, R., Wiaux, V., Wouters, J., and Beckx, S. Bandwidth engineering of photonic crystal waveguide bends. *Electron. Lett.* **40**(20), 1263–1264 (2004).

28. Yanik, M. F., Suh, W., Wang, Z., and Fan, S. Stopping light in a waveguide with an all-optical analog electromagnetically induced transparancy. *Phys. Rev. Lett.* **93**, 233903 (2004).

29. Altug, H. and Vuckovic, J. Two-dimensional coupled photonic crystal resonator arrays. *Appl. Phys. Lett.* **84**(2), 161–163 (2004).

30. Olivier, S., Benisty, H., Weisbuch, C., Smith, C. J. M., Krauss, T. F., Houdré, R., and Oesterle, U. Improved 60 bend transmission of submicron-width waveguides defined in two-dimensional photonic crystals. *J. Lightwave Technol.* **20**(7), 1198–1203 (2002).

31. Xing, P., Borel, P., Frandsen, L. H., Harpøth, A., and Kristensen, M. Optimization of bandwidth in 60° photonic crystal waveguide bends. *Opt. Communic.* **248**(1-3), 179–184 (2005).

32. Cox, S. and Dobson, D. Band structure optimization of two-dimensional photonic crystals in H-polarization. *J. Comput. Phys.* **158**(2), 214–224 (2000).

33. Dobson, D. and Santosa, F. Optimal localization of eigenfunctions in an inhomogeneous medium. *SIAM J. Appl. Math.* **64**(5), 762–774 (2003).

34. Burger, M., Osher, S., and Yablonovitch, E. Inverse problem techniques for the design of photonic crystals. *IEICE Trans. Electron.* **E87-C**(3), 258–265 (2004).

35. Kao, C., Osher, S., and Yablonovitch, E. Maximizing band gaps in two-dimensional photonic crystals by using level set methods. *Appl. Phys. B* **81**(2-3), 235–244 (2005).

36. Bendsøe, M. P. and Sigmund, O. *Topology Optimization - Theory, Methods and Applications*. Springer, Berlin, (2003).

37. Jensen, J. S. and Sigmund, O. Systematic design of photonic crystal structures using topology optimization: Low-loss waveguide bends. *Appl. Phys. Lett.* **84**(12), 2022–2024 (2004).

38. Jensen, J. S. and Sigmund, O. Topology optimization of photonic crystal structures: A high bandwidth low loss T-junction waveguide. *J. Opt. Soc. Am. B* **22**(6), 1191–1198, June (2005).

39. Svanberg, K. The method of moving asymptotes - a new method for structural optimization. *Int. Numer. Methods Eng.* **24**, 359–373 (1987).

40. Frandsen, L. H., Harpøth, A., Borel, P., Kristensen, M., Jensen, J. S., and Sigmund, O. Broadband photonic crystal waveguide 60° bend obtained utilizing topology optimization. *Opt. Express* **12**(24), 5916–5921 (2004).

41. Jensen, J. S., Sigmund, O., Frandsen, L. H., Borel, P., Harpøth, A., and Kristensen, M. Topology design and fabrication of a new double 90-degree photonic crystal waveguide bend. *IEEE Photonics Technol. Lett.* **17**(6), 1202–1204 (2005).

42. Borel, P., Frandsen, L. H., Harpøth, A., Kristensen, M., Jensen, J. S., and Sigmund, O. Topology optimised broadband photonic crystal Y-splitter. *Electron. Lett.* **41**(2), 69–71 (2005).

43. Sigmund, O. and Jensen, J. S. Topopt. http://www.topopt.dtu.dk/.

44. Bogaerts, W., Wiaux, V., Taillert, D., Beckx, S., Luyssaert, B., Bienstman, P., and Baets, R. Fabrication of photonic crystals in silicon-on-insulator using 248-nm deep UV lithography. *IEEE J. Select. Top. Quantum Electron.* **8**(4), 928–934 (2002).

45. Bogaerts, W., Wiaux, V., Dumon, P., Taillert, D., Wouters, J., Beckx, S., Van Campenhout, J., Luyssaert, B., and Baets, R. Large-scale production techniques for photonic nanostructures. *Proc. SPIE* **5225**, 101–112 (2003).

46. Bogaerts, W. *Nanophotonic Waveguides and Photonic Crystals in Silicon-on-Insulator*. Ph.D. thesis, Vakgroep Informatietechnologie (In-TEC), Faculteit Toegepaste Wetenschappen, Ghent University, (2004).

47. Thorhauge, M., Frandsen, L., Borel, P., Harpøth, A., Zhuang, Y., Kristensen, M., Bogaerts, W., Dumon, P., Baets, R., Wiaux, V., Wouters, J., and Beckx, S. Novel low-loss 60° bends in photonic crystal waveguides. *Conference on Lasers and Electro-Optics (CLEO)* **1**, 2 pp. (2004).

48. Frandsen, L., Borel, P., Zhuang, Y., Harpøth, A., Thorhauge, M., Kristensen, M., Bogaerts, W., Dumon, P., Baets, R., Wiaux, V., Wouters, J., and Beckx, S. Ultralow-loss 3-dB photonic crystal waveguide splitter. *Opt. Lett.* **29**(14), 1623–1625 (2004).

49. Auberton-Herve, A., Bruel, M., Aspar, B., Maleville, C., and Moriceau, H. Smart-Cut(R): the basic fabrication process for unibond(R) SOI wafers. *IEICE Trans. Electron.* **E80-C**(3), 358–363 (1997).

50. Chang, T. Proximity effect in electron-beam lithography. *J. Vac. Sci. Technol.* **12**(6), 1271–1275 (2004).

51. Owen, G. and Rissman, P. Proximity effect correction for electron beam lithography by equalization of background dose. *J. Appl. Phys.* **54**(6), 3573–3582 (1983).

52. JEOL. Jbx 9300fs. http://www.nanolithography.gatech.edu/JEOL_JBX-9300FS_Training.pdf.

53. Rosenfield, M. G., Thomson, M. G. R., Coane, P. J., Kwietniak, K. T., Keller, J., Klaus, D. P., Volant, R. P., Blair, C. R., Tremaine, K. S., Newman, T. H., and Hoh, F. J. Electron-beam lithography for advanced device prototyping: Process tool metrology. *J. Vac. Sci. Technol.* **B11**(6), 2615–2620 (1993).

54. McCord, M. A. and Rooks, M. J. Spie handbook of microlithography, micromachining and microfabrication, (2000). http://www.cnf.cornell.edu/cnf_spietoc.html.

55. Legtenberg, R., Jansen, H., de Boer, M., and Elwenspoek, M. Anisotropic reactive ion etching of silicon using $SF_6/O_2/CHF_3$ gas mixtures. *J. Electrochem. Soc.* **142**(6), 2020–2028 (1995).

56. Jensen, S. *Inductively Coupled Plasma Etching for Microsystems*. Ph.D. thesis, Department of Micro and Nanotechnology, MIC, Technical University of Denmark, (2004).

57. Sze, S. *Semiconductor Devices: Physics and Technology*. John Wiley & Sons, (1985).

58. Bienstmann, P., Bogaerts, W., and Baets, R. Scattering at sidewall roughness in photonic crystal slabs. *Opt. Lett.* **28**(9), 689–691 (2003).

59. Hughes, S., Ramunno, L., Young, J., and Sipe, J. Extrinsic optical scattering loss in photonic crystal waveguides: Role of fabrication disorder and photon gorup velocity. *Phys. Rev. Lett.* **94**(3), 1–4 (2005).

60. Goldstein, J., Newbury, D., Joy, D., Lyman, C., Echlin, P., Lifshin, E., Sawyer, L., and Michael, J. *Preparation of thin films*. Kluwer Academic/Plenum Publishers, New York, (2003).

61. Borel, P., Frandsen, L. H., Thorhauge, M., Harpøth, A., Zhuang, Y. Z., and Kristensen, M. Efficient propagation of TM polarized light in photonic crystal components exhibiting band gaps for TE polarized light. *Opt. Express* **11**(15), 1757–1762 (2003).

62. Finlayson, C. E., Cattaneo, F., Perney, N. M. B., Baumberg, J. J., Netti, M. C., Zoorob, M. E., Charlton, M. D. B., and Parker, G. J. Slow light and chromatic temporal dispersion in photonic crystal waveguides using femtosecond time of flight. *Phys. Rev. E* **73**, 016619:1–10 (2006).

63. Roussey, M., Baida, F. I., and Bernal, M.-P. Experimental and theorical observations of the slow-light effect on a tunable photonic crystal. *J. Opt. Soc. Am. B* **24**(6), 1416–1422 (2007).

64. Gu, L., Jiang, W., Chen, X., Wang, L., and Chen, R. T. High speed silicon photonic crystal waveguide modulator for low voltage operation. *Appl. Phys. Lett.* **90**, 071105:1–3 (2007).

65. Okawachi, Y., Foster, M. A., Sharping, J. E., Gaeta, A. L., Xu, Q., and Lipson, M. All-optical slow-light on a photonic chip. *Opt. Express* **14**(6), 2317–2322 (2006).

66. Miyai, E. and Noda, S. Structural dependence of coupling between a two-dimensional photonic crystal waveguide and a wire waveguide. *J. Opt. Soc. Am. B* **21**(1), 67–72, January (2004).

67. Ushida, J., Tokushima, M., Shirane, M., Gomyo, A., and Yamada, H. Immittance matching for multidimensional open-system photonic crystals. *Phys. Rev. B* **68**, 155115 (2003).

68. Sanchis, P., Bienstman, P., Luyssaert, B., Baets, R., and Marti, J. Analysis of butt coupling in photonic crystals. *IEEE J. Quantum Electron.* **40**(5), 541–550 (2004).

69. Vlasov, Y. A., Moll, N., and McNab, S. J. Observation of surface states in a truncated photonic crystal slab. *Opt. Lett.* **29**(18), 2175–2177 (2004).

70. Kramper, P., Agio, M., Soukoulis, C. M., Birner, A., Müller, F., Wehrspohn, R. B., Gösele, U., and Sandoghdar, V. Highly directional emission from photonic crystal waveguides of subwavelength width. *Phys. Rev. Lett.* **92**(11), 113903 (2004).

71. Moreno, E., García-Vidal, F. J., and Martín-Moreno, L. Enhanced transmission and beaming of light via photonic crystal surface modes. *Phys. Rev. B* **69**, 121402(R) (2004).

72. Velha, P., Hugonin, J. P., and Lalanne, P. Compact and efficient injection of light into band-edge slow-modes. *Opt. Express* **15**(10), 6102–6112 (2007).

73. Hugonin, J. P., Lalanne, P., White, T. P., and Krauss, T. F. Coupling into slow-mode photonic crystal waveguides. *Opt. Lett.* **32**(18), 2638–2640 (2007).

74. Vlasov, Y. A. and McNab, S. J. Coupling into the slow light mode in slab-type photonic crystal waveguides. *Opt. Lett.* **31**(1), 50–52 (2006).

75. Pottier, P., Gnan, M., and De La Rue, R. M. Efficient coupling into slow-light photonic crystal channel guides using photonic crystal tapers. *Opt. Express* **15**(11), 6569–6575 (2007).

76. Ozaki, N., Kitagawa, Y., Takata, Y., Ikeda, N., Watanabe, Y., Mizutani, A., Sugimoto, Y., and Asakawa, K. High transmission recovery of slow light in a photonic crystal waveguide using a hetero groupvelocity waveguide. *Opt. Express* **15**(13), 7974–7983 (2007).

77. Talneau, A., Le Gouezigou, L., Bouadma, N., Kafesaki, M., Soukoulis, C. M., and Agio, M. Photonic-crystal ultrashort bends with improved transmission and low reflection at 1.55 μ m. *Appl. Phys. Lett.* **80**(4), 547–549 (2002).

78. Dinu, M., Willett, R. L., Baldwin, K., Pfeiffer, L. N., and West, K. W. Waveguide tapers and waveguide bends in AlGaAs-based two-dimensional photonic crystals. *Appl. Phys. Lett.* **83**(22), 4471–4473 (2003).

79. Talneau, A., Mulot, M., Anand, S., Olivier, S., Agio, M., Kafesaki, M., and Soukoulis, C. M. Modal behavior of single-line photonic crystal guiding structures on inp substrate. *Photon. Nanostr.-Fundament. Applicat.* **2**(1), 1–10 (2004).

80. Ntakis, I., Pottier, P., and De La Rue, R. M. Optimization of transmission properties of two-dimensional photonic crystal channel waveguide bends through local lattice deformation. *J. Appl. Phys.* **96**(1), 12–18 (2004).

81. Smajic, J., Hafner, C., and Erni, D. On the design of photonic crystal multiplexers. *Opt. Express* **11**(6), 566–571 (2004).

82. Miao, B., Chen, C., Shi, S., Murakowski, J., and Prather, D. W. High-efficiency broad-band transmission through a double-60° bend in a planar photonic crystal single-line defect waveguide. *IEEE Photon. Technol. Lett.* **16**(11), 2469–2471 (2004).

83. Moll, N. and Bona, G.-L. Bend design for the low-group-velocity mode in photonic crystal waveguide bends. *Appl. Phys. Lett.* **85**(19), 4322–4324 (2004).

84. Inoue, K., Sgimoto, Y., Ikeda, N., Tanaka, Y., Asakawa, K., Maruyama, T., Miyashita, K., Ishida, K., and Watanabe, Y. Ultrasmall GaAs-photonic-crystal-slab-waveguide-based near-infrared components: fabrication, guided-mode identification, and estimation of low-loss and broad-band-width in straight-waveguides, 60°-bends and y-splitter. *Japan. J. Appl. Phys.* **43**(9A), 6112–6124 (2004).

85. Ikeda, N., Sugimoto, Y., Tanaka, Y., Inoue, K., and Asakawa, K. Low propagation losses in single-line-defect photonic crystal waveguides on GaAs membranes. *IEEE J. on Select. Areas Communic.* **23**(7), 1315–1319, July (2005).

86. Xiaoa, S. and Qiu, M. Study of transmission properties for waveguide bends by use of a circular photonic crystal. *Phys. Lett. A* **340**(5-6), 474–479 (2005).

87. Zhang, Y. and Li, B. Ultracompact waveguide bends with simple topology in two-dimensional photonic crystal slabs for optical communication wavelengths. *Opt. Lett.* **32**(7), 787–789 (2007).

88. Assefa, S., McNab, S., and Vlasov, Y. A. Transmission of slow light through photonic crystal waveguide bends. *Opt. Lett.* **31**(6), 745–747 (2006).

89. Frandsen, L., Lavrinenko, A., Fage-Pedersen, J., and Borel, P. I. Photonic crystal waveguides with semi-slow light and tailored dispersion properties. *Opt. Express* **14**(20), 9444–9450 (2006).

90. Pavesi, L., Dal Negro, L., Mazzoleni, C., Franzò, G., and Priolo, F. Optical gain in silicon nanocrystals. *Nature* **408**, 440–444, November (2000).

91. Fujii, M., Yoshida, M., Kanzawa, Y., Hayashi, S., and Yamamoto, K. 1.54 μm photoluminescence of Er^{3+} doped into SiO_2 films containing Si nanocrystals: Evidence for energy transfer from Si nanocrystals to Er^{3+}. *Appl. Phys. Lett.* **71**(9), 1198–1200, September (1997).

92. Kjeldsen, M. Nanocrystals images., (2007). madsmk@phys.au.dk.

93. Tasco, V., Deguffroy, N., Baranov, A. N., Tournié, E., Satpati, B., Trampert, A., Dunaevski, M., and Titkov, A. High-density InSb-based quantum dots emitting in the mid-infrared. *J. Crys. Growth* **301-302**, 713–717 (2007).

94. Zhu, K., Shi, J., and Zhang, L. Preparation and optical absorption of InSb microcrystallites embedded in SiO_2 thin films. *Solid State Commun.* **107**, 79–84 (1998).

95. Capoen, B., Lam, V. Q., Turrell, S., Vilcot, J. P., Beclin, F., Jestin, Y., and Bouazaoui, M. Study of structural and optical properties of InSb-doped SiO_2 thin films. *J. Non-Cryst. Solids* **351**, 1819–1824 (2005).

96. Kittel, C. *Introduction to solid state physics*. John Wiley & Sons, (1996).

97. Bimberg, D., Grundmann, M., and Ledentsov, N. N. *Quantum dot heterostructures*. John Wiley & Sons, (1999).

98. Tasco, V., Deguffroy, N., Baranov, A. N., Tournié, E., Satpati, B., and Trampert, A. Structural and optical properties of InSb quantum dots for mid-IR applications. *Phys. Stat. Sol. B.* **243**(15), 3959–3962 (2006).

99. Brus, L. E. A simple model for the ionization potential, electron affinity, and aqueous redox potentials of small semiconductor crystallites. *J. Chem. Phys.* **79**(11), 5566–5571 (1983).

100. Allan, G., Niquet, Y. M., and Delerue, C. Quantum confinement energies in zinc-blende III-V and group IV semiconductors. *Appl. Phys. Lett.* **77**(5), 639–641 (2000).

101. Alphandéry, E., Nicholas, R. J., Mason, N. J., Lyapin, S. G., and Klipstein, P. C. Photoluminescence of self-assembled InSb quantum dots grown on GaSb as a function of excitation power, temperature, and magnetic field. *Phys. Rev. B* **65**, 115322 (2002).

102. Niquet, Y. M., Allan, G., Delerue, C., and Lannoo, M. Quantum confinement in germanium nanocrystals. *Appl. Phys. Lett.* **77**(8), 1182–1184 (2000).

103. Jensen, J. S. *Silicon based materials for optical applications*. PhD. thesis, Interdisciplinary Nanoscience Center (iNANO), and Department of Physics and Astronomy, University of Aarhus, (2007).

104. George, J. *Preparation of thin films*. Marcel Dekker, Inc., (1992).

105. Efros, A. L., Lockwood, D. J., and Tsybeskov, L. *Semiconductor Nanocrystals. From Basic Principles to Applications*. Kluwer Academic/Plenum Publishers, (2003).

106. Porter, D. A. and Easterling, K. E. *Phase Transformations in Metals and Alloys, Second Edition*. CRC Press, Taylor & Francis Group, (1992).

107. Ratke, L. and Voorhees, P. W. *Growth and coarsening*. Springer, (2002).

108. Als-Nielsen, J. and McMorrow, D. *Elements of Modern X-ray Physics*. John Wiley & Sons, (2001).

109. Klug, H. P. and Alexander, L. E. *X-ray diffraction procedures*. John Wiley & Sons, (1974).

110. Williams, D. B. and Carter, C. B. *Transmission electron microscopy, Vol. I-IV*. Plenum Press, New York and London, (1996).

111. Mayer, J. W. and Rimini, E. *Ion beam handbook for material analysis*. Academic Press, (1977).

112. Feldman, L. C. and Mayer, J. W. *Fundamentals of surface and thin film analysis*. Elsevier Science Publishing Co., Inc., (1986).

113. Thompson, M. Rutherford backscattering spectroscopy analysis package, (2002). http://www.genplot.com/.

114. Govil, I. M. Proton induced X-ray emission - a tool for non-destructive trace element analysis. *Curr. Sci.* **80**(12), 1542–1549 (2001).

115. JCPDS. *Metals & Alloys Data Book*. JCPDS International Centre for Diffraction Data, (1978).

116. Ashcroft, N. W. and Mermin, N. D. *Solid State Physics*. Thomson Learning, Inc., (1976).

117. Yu, P. Y. and Cardona, M. *Fundamentals of semiconductors*. Springer, (2005).

118. Elliman, R. G., Lederer, M. J., and Luther-Davies, B. Optical absorption measurements of silica containing Si nanocrystals produced by ion implantation and thermal annealing. *Appl. Phys. Lett.* **80**(8), 1325–1327 (2002).

119. Uhrenfeldt, C. PF Matlab implementated code for multiple interferences simulation in absorbance spectra., (2007). chru@phys.au.dk.

120. Pawlow, P. Dependence of melting-point upon surface energy of solid bodies. *Zeitschr. Phys. Chem.* **65**(1), 1–35 (1909).

121. Takagi, M. Electron-diffraction study of liquid-solid transition of thin metal films. *J. Phys. Soc. Jpn.* **9**, 959 (1954).

122. Couchman, P. R. and Jesser, W. A. Thermodynamic theory of size dependence of melting temperature in metals. *Nature* **469**, 481–483 (1977).

123. Buffat, P. and Borel, J.-P. Size effect on the melting temperature of gold particles. *Phys. Rev. A* **13**(6), 2287–2298 (1976).

124. Baletto, F. and Ferrando, R. Structural properties of nanoclusters. *Rev. Mod. Phys.* **77**(1), 371 (2005).

125. Goldstein, A. N., Echer, C. M., and Alivisatos, A. P. Melting in semiconductor nanocrystals. *Science* **256**, 1425 (1992).

126. Černý, R., Cháb, V., Ivlev, G., Gatskevich, E., and Přikryl, P. Modeling the phase-change processes in pulsed laser-irradiated InSb. *Phys. Rev. B* **59**(16), 10685–10690 (2001).

127. Xu, Q., Sharp, I. D., Yuan, C. W., Yi, D. O., Liao, C. Y., Glaeser, A. M., Minor, A. M., Beeman, J. W., Ridgway, M. C., Kluth, P., Ager III, J. W., Chrzan, D. C., and Haller, E. E. Large melting-point hysteresis of Ge nanocrystals embedded in SiO_2. *Phys. Rev. Lett.* **97**, 155701 (2006).

128. Reif, F. *Fundamentals of Statistical and Thermal Physics*. McGraw-Hill Book Company, (1965).

129. Banus, M. D., Hanneman, R. E., Mariano, A. N., Warekois, E. P., Gatos, H. C., and Kafalas, J. A. High-pressure tetragonal phase of InSb. *Appl. Phys. Lett.* **2**(2), 35–36 (1963).

130. Atkins, P. W. and de Paula, J. *Atkins' Physical chemistry*. Oxford University Press, (2002).

131. Kota, A. K., Anand, G., Ramakrishnan, S., Regel, L. L., and Wilcox, W. R. Influence of oxygen, hydrogen, helium, argon and vacuum on the surface behavior of molten InSb, other semiconductors, and metals on silica. *J. Cryst. Growth* **290**, 319–333 (2006).

132. Lide, D. R. *Handbook of Chemistry and Physics*. CRC Press LLC, (2003).

133. Masutomi, R., Hio, M., Mochizuki, T., and Okamoto, T. Quantum Hall effect at cleaved InSb surfaces and low-temperature annealing effect. *Appl. Phys. Lett.* **90**(20), 202104–1–3 (2007).

134. Tong, S., Liu, X., and Bao, X. Study of photoluminescence in nanocrystalline silicon/amorphous silicon multilayers. *Appl. Phys. Lett.* **66**, 469–471 (1995).

135. Kariotis, R. Non-equilibrium roughening transitions. *J. Phys. A: Math. Gen.* **22**(14), 2781–2794 (1989).

136. Windischmann, H. Intrinsic stress in sputter-deposited thin films. *Crit. Rev. Solid State Mater. Sci.* **17**(6), 547–596 (1992).